Available on CMS information server

CMS AN -2016/459

The Compact Muon Solenoid Experiment

Analysis Note

The content of this note is intended for CMS internal use and distribution only

09 December 2016 (v8, 21 August 2018)

Search for Heavy Resonances decaying to Top Quark Pairs in the All-Hadronic Channel with pp Collisions at 13 TeV at the CMS experiment

Christine A. McLean, Justin Pilot, Robin Erbacher, John Conway, Sal Rappoccio, Ashley Parker, Sheila Amaral,
James Dolen, Neeti Parashar

Abstract

Search for heavy resonances decaying to top quark pairs in the all-hadronic channel with pp collisions at 13 TeV at the CMS experiment with data taken in 2016.

DRAFT
CMS Physics Analysis Summary

2018/08/21
Head Id: 456579
Archive Id: 471893:472417
Archive Date: 2018/04/20
Archive Tag: trunk

Search for Heavy Resonances decaying to Top Quark Pairs in the All-Hadronic Channel with pp Collisions at 13 TeV at the CMS experiment

The CMS Collaboration

Abstract

We present a search for new massive particles which decay to a pair of top quarks using the full dataset collected by the CMS experiment in 2016 at $\sqrt{s} = 13$ TeV. We consider the decay topology in which each top quark decays hadronically and the individual top quark's decay products are reconstructed within a single jet. We utilize jet substructure, subjet b-tagging, and novel pileup mitigation tools to improve our sensitivity to these objects.

This box is only visible in draft mode. Please make sure the values below make sense.

PDFAuthor: Christine A. McLean, Justin Pilot, Robin Erbacher, John Conway, Sal Rappoccio, James Dolen, Ashley Parker
PDFTitle: Search for Heavy Resonances decaying to Top Quark Pairs in the All-Hadronic Channel with pp Collisions at 13 TeV at the CMS experiment
PDFSubject: CMS
PDFKeywords: CMS, physics, software, computing

Please also verify that the abstract does not use any user defined symbols

Contents

1 Change Log

1.1 AN v8 summary

- Dataset: JetHT 03Feb2017 ReminiAOD
- JSON: Final 23Sep2016ReReco
- MC: RunIISummer16MiniAODv2-PUMoriond17
- JEC: Summer16 23Sep2016 V4
- JER: Spring16 25nsV10
- Subjet b-tag: subjet_CSVv2_Moriond17_B_H.csv
- Top p_{T} reweighting

1.2 AN v8 changes with respect to v7

- Added 6, 6.5, and 7 TeV Z′ (1%, 10%, and 30% width) mass points.

1.3 AN v7 changes with respect to v6

- Updated dijet mass distributions and event yields to include closure test uncertainties

1.4 AN v6 changes with respect to v5

- Fully unblinded the analysis.
- Performed QCD closure test.
- Added QCD closure systematic.
- Included NTMJ modmass and closure shape template plots.
- Included narrow Z′ limits separated by b-tag category.
- Added data/MC comparison plot of b-tag discriminant after top-tagging.

1.5 AN v5 changes with respect to v3

- Simplified 1D trigger efficiency plots. Added HT cut to the plot of trigger efficiency vs dijet mass. Added 2D trigger efficiency plots.
- Added 4.5 and 5 TeV mass points for RS KK Gluon
- Add 3 TeV extra-wide Z′ mass point.
- Added correct 2 TeV narrow Z′ mass point.

- Using $\mathrm{t\bar{t}}$ and Z$'$ b-tag efficiencies for respective MC samples.
- Separated b-tag SF systematic uncertainties into b/c-jet and light jet systematics.
- Added partially-blinded limit plots.

1.6 AN v3 changes with respect to v2

- Changed trigger plots to show 1D efficiency. Added a plot of trigger efficiency vs dijet mass.
- Added discovery significance plots.
- Added expected limits for all signal models, now with all systematics included.
- Extra wide Z$'$ limits
- Added 4.5 and 5 TeV Z$'$ mass points and theory cross sections.
- Updated b-tag rate measurement to use PUPPI CSVv2 scores.
- Updated b-tagging scale factor application to consider both subjets, instead of just the subjet with the leading CSVv2 score.
- Added $\mathrm{t\bar{t}}$ and Z$'$ b-tag efficiency plots.

2 Introduction

Many models of new physics predict new particles which have enhanced couplings to the third generation of the Standard Model (SM) [1–9]. Of these, certain models motivate the existence of new heavy resonances that decay to top quark anti-top quark pairs, such as Z$'$ gauge bosons and Randall-Sundrum Kaluza Klein gluons [10–14]. In the analysis described here, we search for heavy resonances in the top anti-top quark pair ($\mathrm{t\bar{t}}$) invariant mass spectrum ($m_{\mathrm{t\bar{t}}}$) to test for the presence of different new physics models. We test for generic leptophobic topcolor models, with the associated resonance labeled as Z$'$, as well as more specific models, such as Randall-Sundrum Kaluza-Klein gluon production.

Past limits have been set for such resonances, with masses below 900 GeV, by the CDF and D0 experiments at the Tevatron [15, 16]. At the LHC, the CMS and ATLAS experiments have continued to set limits for heavy resonances decaying to $\mathrm{t\bar{t}}$. To do so, the experiments have used data from proton-proton collisions at center of mass energies of 7 and 8 TeV to set increasingly strict limits on resonances above 1 TeV [17–24]. The analyses are categorized by the decay modes of the top anti-top pair, with each top decaying into a b quark and W boson, the W subsequently decaying into leptons or a "jet" of hadrons. Most recently, CMS and ATLAS have released $\mathrm{t\bar{t}}$ resonance limits, using data from the first year (2015) of 13 TeV collisions at the LHC [25, 26]. In 2016 the CMS experiment recorded an order of magnitude larger dataset and can now perform a more sensitive search than the 2015 analysis.

In the high mass ranges accessible by the LHC at $\sqrt{s} = 13$ TeV, the event topology of $\mathrm{t\bar{t}}$ production requires special techniques. For example, Z$'$ masses of ≥ 1 TeV decaying to $\mathrm{t\bar{t}}$, the produced top quarks will be highly boosted and the subsequent $\mathrm{t}\rightarrow\mathrm{Wb}$ decays may merge together. We utilize special reconstruction techniques to identify these boosted top quarks.

We consider the topology in which the hadronically decaying top decay products are fully merged into a single jet. For this decay topology, we use a special 'top tagging' algorithm built on identifying substructure within single jets. The tagger used in this analysis is optimized for tops with large boost ($p_{\mathrm{T}} > 400$) and is known as the CMS Top Tagger (V2). This algorithm relies on soft-drop grooming, the N-subjettiness jet shape variable, and subjet b-tagging algorithms to identify top jets. For the first time this analysis now utilizes Pileup Per Particle Identification (PUPPI) before calculating top-tagging variables [27]. PUPPI greatly reduces the effects of pileup on top-tagging performance.

The analysis utilizes the differences in the invariant mass spectrum of the $\mathrm{t\bar{t}}$ pairs ($M_{\mathrm{t\bar{t}}}$) from resonant production and non-resonant SM production in order to search for new resonances. The dominant background from non-top multijet backgrounds (NTMJ) is estimated from data.

We present an update to three existing CMS searches ($\sqrt{s} = 7$ TeV[17], $\sqrt{s} = 8$ TeV[21], $\sqrt{s} = 13$ TeV[28]). The updated search uses the 2016 13 TeV dataset, corresponding to an integrated luminosity of 36 fb^{-1}, with new PUPPI top tagging tools.

3 Analysis Strategy

We use essentially the same analysis strategy used in the previous iteration of this analysis [28], with the addition of PUPPI top-tagging variables used to identify boosted top quark decays. We consider events in the ‘type 1+1’ topology, where a ‘type 1’ top candidate consists of a single jet containing all the decay products from the top quark. Again we use large jets to capture these decay products more efficiently. The CMS Top Tagger V2 (CMSTT V2) uses anti$-kT$ jets with a distance parameter of $R = 0.8$. The CMSTT V2 algorithm utilizes soft drop grooming and $N-$subjettiness, a jet shape variable which determines how consistent a jet is with having N or fewer subjets, in order to identify top jets and reject QCD multijet background. The multijet background is further reduced by utilizing subjet b-tagging. We divide events into categories based on the number of jets containing subjets consistent with a b-quark.

The dominant background for this analysis, where the selection consists of dijet events, is multijet events originating from non-top QCD interactions (non-top multijet, i.e., NTMJ). This background is estimated using a top-tag mistag rate measured using a control region in data. This mistag rate is then applied to data events to estimate the NTMJ background in the signal region. In the most sensitive signal regions, the dominant background is standard model $\mathrm{t\bar{t}}$ production, which is estimated using simulated events. We validate our background model, and proceed to test for the presence of several different signal hypotheses, including both narrow, wide, and extra wide (1%, 10%, and 30% widths, respectively) Z' samples, and Randall-Sundrum Kaluza-Klein gluon models.

4 Samples

4.1 Data Samples

We use data collected in 2016 during Run 2 of the LHC, for which the center-of-mass energy was $\sqrt{s} = 13$ TeV. We use the JetHT primary dataset, as we are interested in events with a large hadronic activity. We use the final ReReco data certification JSON file

`Cert_271036-284044_13TeV_23Sep2016ReReco_Collisions16_JSON`

corresponding to an integrated luminosity of 36 fb^{-1}. The datasets used are summarized in Table 1, and are reconstructed with CMSSW version 8.0.X.

Dataset
`/JetHT/Run2016B-03Feb2017_ver2-v2/MINIAOD`
`/JetHT/Run2016C-03Feb2017-v1/MINIAOD`
`/JetHT/Run2016D-03Feb2017-v1/MINIAOD`
`/JetHT/Run2016E-03Feb2017-v1/MINIAOD`
`/JetHT/Run2016F-03Feb2017-v1/MINIAOD`
`/JetHT/Run2016G-03Feb2017-v1/MINIAOD`
`/JetHT/Run2016H-03Feb2017_ver2-v1/MINIAOD`
`/JetHT/Run2016H-03Feb2017_ver3-v1/MINIAOD`

Table 1: Data samples used in the analysis.

4.2 Simulated Background Samples

We use samples of simulated events to estimate our background from SM continuum $\mathrm{t\bar{t}}$ events. These samples were generated with POWHEG interfaced to PYTHIA 8, and we use a cross section of $\sigma_{\mathrm{t\bar{t}}} = 831.76$ pb for normalization [29] to determine the expected number of events. The $\mathrm{t\bar{t}}$ sample used is inclusive in the top decay products. The $\mathrm{t\bar{t}}$ samples used in this analysis are listed in Table 2.

A data driven method is used to estimate the non-top multijet (NTMJ) background in the analysis, while simulated QCD Monte Carlo events are used to test our analysis methods and to test the closure of the NTMJ background estimate technique. We consider both QCD Monte Carlo simulated with MADGRAPH and showered with PYTHIA 8 (Table 3) and QCD Monte Carlo simulated and showered with PYTHIA 8 (Table 4). While both samples are used for the closure tests and kinematic plots in Appendix A, Figs. 8 – 13 are plotted using the latter QCD sample, as it is found to better model the data.

4.3 Simulated Signal Samples

Table 5 lists Z′ samples with widths set to 1% of the mass of the Z′, Table 6 lists Z′ samples with widths set to 10% of the mass of the Z′, Table 7 lists Z′ samples with widths set to 30% of the mass of the Z′, and Table 8 lists Randal-Sundrum Gluon samples with widths approximately 17% of the mass of the RS Gluon. We use samples generated as part of the "RunIISummer16" campaign, generated using CMSSW version 8.0.X. The samples have a bunch spacing of 25 ns, and use the miniAODv2 data format. We use mass points between 1 and 5 TeV, in increments of 500 GeV.

4.4 Pileup reweighting

The samples used are simulated for the scenario with 25 ns bunch spacing and a pileup scenario which approximates the 2016 data-taking conditions (`mix_2016_25ns_Moriond17MC_PoissonOOTPU`). The simulated signal and background events are reweighed to accurately model the pileup conditions in data, using a minimum bias cross section of 69.2 mb (± 4.6%) (Fig. 1) [30].

Sample	Dataset	Events	σ (pb), NNLO
$t\bar{t}$	`/TT_TuneCUETP8M2T4_13TeV-powheg-pythia8` `/RunIISummer16MiniAODv2-PUMoriond17_80X_mcRun2_asymptotic_2016_TrancheIV_v6-v1/MINIAODSIM`	77229341	831.76
$t\bar{t}$ extension	`/TT_TuneCUETP8M2T4_13TeV-powheg-pythia8` `/RunIISummer16MiniAODv2-PUMoriond17_backup_80X_mcRun2_asymptotic_2016_TrancheIV_v6-v1/MINIAODSIM`	77709140	831.76

Table 2: Standard model background simulated samples

Sample	**Dataset**	**Events**	**σ (pb), LO**
QCD Madgraph + Pythia8 HT $\in$ [200,300]extension	`/QCD_HT200to300_TuneCUETP8M1_13TeV-madgraphMLM-pythia8` `/RunIISummer16MiniAODv2-PUMoriond17_80X_mcRun2_asymptotic_2016_TrancheIV_v6_ext1-v1/MINIAODSIM`	38857977	1712000
QCD Madgraph + Pythia8 HT $\in$ [300,500]	`/QCD_HT300to500_TuneCUETP8M1_13TeV-madgraphMLM-pythia8` `/RunIISummer16MiniAODv2-PUMoriond17_80X_mcRun2_asymptotic_2016_TrancheIV_v6-v1/MINIAODSIM`	16914727	347700
QCD Madgraph + Pythia8 HT $\in$ [300,500]extension	`/QCD_HT300to500_TuneCUETP8M1_13TeV-madgraphMLM-pythia8` `/RunIISummer16MiniAODv2-PUMoriond17_80X_mcRun2_asymptotic_2016_TrancheIV_v6_ext1-v1/MINIAODSIM`	37502012	347700
QCD Madgraph + Pythia8 HT $\in$ [500,700]	`/QCD_HT500to700_TuneCUETP8M1_13TeV-madgraphMLM-pythia8` `/RunIISummer16MiniAODv2-PUMoriond17_80X_mcRun2_asymptotic_2016_TrancheIV_v6-v1/MINIAODSIM`	18929951	32100
QCD Madgraph + Pythia8 HT $\in$ [500,700] extension	`/QCD_HT500to700_TuneCUETP8M1_13TeV-madgraphMLM-pythia8` `/RunIISummer16MiniAODv2-PUMoriond17_80X_mcRun2_asymptotic_2016_TrancheIV_v6_ext1-v1/MINIAODSIM`	43341392	32100
QCD Madgraph + Pythia8 HT $\in$ [700,1000]	`/QCD_HT700to1000_TuneCUETP8M1_13TeV-madgraphMLM-pythia8` `/RunIISummer16MiniAODv2-PUMoriond17_80X_mcRun2_asymptotic_2016_TrancheIV_v6-v1/MINIAODSIM`	15629253	6831
QCD Madgraph + Pythia8 HT $\in$ [700,1000] extension	`/QCD_HT700to1000_TuneCUETP8M1_13TeV-madgraphMLM-pythia8` `/RunIISummer16MiniAODv2-PUMoriond17_80X_mcRun2_asymptotic_2016_TrancheIV_v6_ext1-v1/MINIAODSIM`	29697035	6831
QCD Madgraph + Pythia8 HT $\in$ [1000,1500]	`/QCD_HT1000to1500_TuneCUETP8M1_13TeV-madgraphMLM-pythia8` `/RunIISummer16MiniAODv2-PUMoriond17_80X_mcRun2_asymptotic_2016_TrancheIV_v6-v1/MINIAODSIM`	4767100	1207
QCD Madgraph + Pythia8 HT $\in$ [1000,1500] extension	`/QCD_HT1000to1500_TuneCUETP8M1_13TeV-madgraphMLM-pythia8` `/RunIISummer16MiniAODv2-PUMoriond17_80X_mcRun2_asymptotic_2016_TrancheIV_v6_ext1-v1/MINIAODSIM`	10360193	1207
QCD Madgraph + Pythia8 HT $\in$ [1500,2000]	`/QCD_HT1500to2000_TuneCUETP8M1_13TeV-madgraphMLM-pythia8` `/RunIISummer16MiniAODv2-PUMoriond17_80X_mcRun2_asymptotic_2016_TrancheIV_v6-v1/MINIAODSIM`	3970819	119.9
QCD Madgraph + Pythia8 HT $\in$ [1500,2000] extension	`/QCD_HT1500to2000_TuneCUETP8M1_13TeV-madgraphMLM-pythia8` `/RunIISummer16MiniAODv2-PUMoriond17_80X_mcRun2_asymptotic_2016_TrancheIV_v6_ext1-v1/MINIAODSIM`	7855883	119.9
QCD Madgraph + Pythia8 HT $\in$ [2000,Inf]	`/QCD_HT2000toInf_TuneCUETP8M1_13TeV-madgraphMLM-pythia8` `/RunIISummer16MiniAODv2-PUMoriond17_80X_mcRun2_asymptotic_2016_TrancheIV_v6-v1/MINIAODSIM`	1991645	25.24
QCD Madgraph + Pythia8 HT $\in$ [2000,Inf]extension	`/QCD_HT2000toInf_TuneCUETP8M1_13TeV-madgraphMLM-pythia8` `/RunIISummer16MiniAODv2-PUMoriond17_80X_mcRun2_asymptotic_2016_TrancheIV_v6_ext1-v1/MINIAODSIM`	4047360	25.24

Table 3: Standard model background simulated samples

Sample	Dataset	Events	σ (pb), LO
QCD Pythia8 $\hat{p}_T \in$ [300,470]	`/QCD_Pt_300to470_TuneCUETP8M1_13TeV_pythia8` `/RunIISpring16MiniAODv2-PUSpring16RAWAODSIM_reHLT_80X_mcRun2_asymptotic_v14-v1/MINIAODSIM`	4150588	7823
QCD Pythia8 $\hat{p}_T \in$ [300,470]	`/QCD_Pt_300to470_TuneCUETP8M1_13TeV_pythia8` `/RunIISummer16MiniAODv2-PUMoriond17_80X_mcRun2_asymptotic_2016_TrancheIV_v6_ext1-v1/MINIAODSIM`	15282856	7823
QCD Pythia8 $\hat{p}_T \in$ [470,600]	`/QCD_Pt_470to600_TuneCUETP8M1_13TeV_pythia8` `/RunIISummer16MiniAODv2-PUMoriond17_80X_mcRun2_asymptotic_2016_TrancheIV_v6-v1/MINIAODSIM`	3959986	648.2
QCD Pythia8 $\hat{p}_T \in$ [470,600]	`/QCD_Pt_470to600_TuneCUETP8M1_13TeV_pythia8` `/RunIISummer16MiniAODv2-PUMoriond17_backup_80X_mcRun2_asymptotic_2016_TrancheIV_v6-v1/MINIAODSIM`	15458074	648.2
QCD Pythia8 $\hat{p}_T \in$ [600,800]	`/QCD_Pt_600to800_TuneCUETP8M1_13TeV_pythia8` `/RunIISummer16MiniAODv2-PUMoriond17_80X_mcRun2_asymptotic_2016_TrancheIV_v6-v1/MINIAODSIM`	3896412	186.9
QCD Pythia8 $\hat{p}_T \in$ [600,800]	`/QCD_Pt_600to800_TuneCUETP8M1_13TeV_pythia8` `/RunIISummer16MiniAODv2-PUMoriond17_80X_mcRun2_asymptotic_2016_TrancheIV_v6_ext1-v1/MINIAODSIM`	9622896	186.9
QCD Pythia8 $\hat{p}_T \in$ [800,1000]	`/QCD_Pt_800to1000_TuneCUETP8M1_13TeV_pythia8` `/RunIISummer16MiniAODv2-PUMoriond17_80X_mcRun2_asymptotic_2016_TrancheIV_v6-v1/MINIAODSIM`	3992112	32.293
QCD Pythia8 $\hat{p}_T \in$ [800,1000]	`/QCD_Pt_800to1000_TuneCUETP8M1_13TeV_pythia8` `/RunIISummer16MiniAODv2-PUMoriond17_80X_mcRun2_asymptotic_2016_TrancheIV_v6_ext1-v1/MINIAODSIM`	15194720	32.293
QCD Pythia8 $\hat{p}_T \in$ [1000,1400]	`/QCD_Pt_1000to1400_TuneCUETP8M1_13TeV_pythia8` `/RunIISummer16MiniAODv2-PUMoriond17_80X_mcRun2_asymptotic_2016_TrancheIV_v6-v1/MINIAODSIM`	2999069	9.4183
QCD Pythia8 $\hat{p}_T \in$ [1000,1400]	`/QCD_Pt_1000to1400_TuneCUETP8M1_13TeV_pythia8` `/RunIISummer16MiniAODv2-PUMoriond17_80X_mcRun2_asymptotic_2016_TrancheIV_v6_ext1-v1/MINIAODSIM`	6229840	9.4183
QCD Pythia8 $\hat{p}_T \in$ [1400,1800]	`/QCD_Pt_1400to1800_TuneCUETP8M1_13TeV_pythia8` `/RunIISummer16MiniAODv2-PUMoriond17_80X_mcRun2_asymptotic_2016_TrancheIV_v6-v1/MINIAODSIM`	396409	0.84265
QCD Pythia8 $\hat{p}_T \in$ [1400,1800]	`/QCD_Pt_1400to1800_TuneCUETP8M1_13TeV_pythia8` `/RunIISummer16MiniAODv2-PUMoriond17_80X_mcRun2_asymptotic_2016_TrancheIV_v6_ext1-v1/MINIAODSIM`	2304684	0.84265
QCD Pythia8 $\hat{p}_T \in$ [1800,2400]	`/QCD_Pt_1800to2400_TuneCUETP8M1_13TeV_pythia8` `/RunIISummer16MiniAODv2-PUMoriond17_80X_mcRun2_asymptotic_2016_TrancheIV_v6-v1/MINIAODSIM`	397660	0.12163
QCD Pythia8 $\hat{p}_T \in$ [1800,2400]	`/QCD_Pt_1800to2400_TuneCUETP8M1_13TeV_pythia8` `/RunIISummer16MiniAODv2-PUMoriond17_80X_mcRun2_asymptotic_2016_TrancheIV_v6_ext1-v1/MINIAODSIM`	1552064	0.12163
QCD Pythia8 $\hat{p}_T \in$ [2400,3200]	`/QCD_Pt_2400to3200_TuneCUETP8M1_13TeV_pythia8` `/RunIISummer16MiniAODv2-PUMoriond17_80X_mcRun2_asymptotic_2016_TrancheIV_v6-v1/MINIAODSIM`	399226	0.00682981
QCD Pythia8 $\hat{p}_T \in$ [2400,3200]	`/QCD_Pt_2400to3200_TuneCUETP8M1_13TeV_pythia8` `/RunIISummer16MiniAODv2-PUMoriond17_80X_mcRun2_asymptotic_2016_TrancheIV_v6_ext1-v1/MINIAODSIM`	596904	0.00682981
QCD Pythia8 $\hat{p}_T \in$ [3200,Inf]	`/QCD_Pt_3200toInf_TuneCUETP8M1_13TeV_pythia8` `/RunIISummer16MiniAODv2-PUMoriond17_80X_mcRun2_asymptotic_2016_TrancheIV_v6-v3/MINIAODSIM`	391735	0.000165445

Table 4: Standard model background simulated samples

Sample	Dataset	Events	σ (pb), NLO
Z′ 1 TeV mass, 1% width	/ZprimeToTT_M-1000_W-10_TuneCUETP8M1_13TeV-madgraphMLM-pythia8/RunIISummer16MiniAODv2-PUMoriond17_80X_mcRun2_asymptotic_2016_TrancheIV_v6-v1	103785	4.505
Z′ 1.25 TeV mass, 1% width	/ZprimeToTT_M-1250_W-12p5_TuneCUETP8M1_13TeV-madgraphMLM-pythia8/RunIISummer16MiniAODv2-PUMoriond17_80X_mcRun2_asymptotic_2016_TrancheIV_v6-v1	102833	1.809
Z′ 1.5 TeV mass, 1% width	/ZprimeToTT_M-1500_W-15_TuneCUETP8M1_13TeV-madgraphMLM-pythia8/RunIISummer16MiniAODv2-PUMoriond17_80X_mcRun2_asymptotic_2016_TrancheIV_v6-v1	99690	0.814
Z′ 2 TeV mass, 1% width	/ZprimeToTT_M-2000_W-20_TuneCUETP8M1_13TeV-madgraphMLM-pythia8/RunIISummer16MiniAODv2-PUMoriond17_80X_mcRun2_asymptotic_2016_TrancheIV_v6-v1	91900	0.206
Z′ 2.5 TeV mass, 1% width	/ZprimeToTT_M-2500_W-25_TuneCUETP8M1_13TeV-madgraphMLM-pythia8/RunIISummer16MiniAODv2-PUMoriond17_80X_mcRun2_asymptotic_2016_TrancheIV_v6-v1	100288	0.0617
Z′ 3 TeV mass, 1% width	/ZprimeToTT_M-3000_W-30_TuneCUETP8M1_13TeV-madgraphMLM-pythia8/RunIISummer16MiniAODv2-PUMoriond17_80X_mcRun2_asymptotic_2016_TrancheIV_v6-v1	91004	0.0206
Z′ 3.5 TeV mass, 1% width	/ZprimeToTT_M-3500_W-35_TuneCUETP8M1_13TeV-madgraphMLM-pythia8/RunIISummer16MiniAODv2-PUMoriond17_80X_mcRun2_asymptotic_2016_TrancheIV_v6-v1	91004	0.00735
Z′ 4 TeV mass, 1% width	/ZprimeToTT_M-4000_W-40_TuneCUETP8M1_13TeV-madgraphMLM-pythia8/RunIISummer16MiniAODv2-PUMoriond17_80X_mcRun2_asymptotic_2016_TrancheIV_v6-v1	107914	0.00276
Z′ 4.5 TeV mass, 1% width	/ZprimeToTT_M-4500_W-45_TuneCUETP8M1_13TeV-madgraphMLM-pythia8/RunIISummer16MiniAODv2-PUMoriond17_80X_mcRun2_asymptotic_2016_TrancheIV_v6-v1	100306	0.00109
Z′ 5 TeV mass, 1% width	/ZprimeToTT_M-5000_W-50_TuneCUETP8M1_13TeV-madgraphMLM-pythia8/RunIISummer16MiniAODv2-PUMoriond17_80X_mcRun2_asymptotic_2016_TrancheIV_v6-v1	112042	0.000458
Z′ 6 TeV mass, 1% width	/ZprimeToTT_M-6000_W-60_TuneCUETP8M1_13TeV-madgraphMLM-pythia8/RunIISummer16MiniAODv2-PUMoriond17_80X_mcRun2_asymptotic_2016_TrancheIV_v6-v1	101612	0.000103
Z′ 6.5 TeV mass, 1% width	/ZprimeToTT_M-6500_W-65_TuneCUETP8M1_13TeV-madgraphMLM-pythia8/RunIISummer16MiniAODv2-PUMoriond17_80X_mcRun2_asymptotic_2016_TrancheIV_v6-v1	99576	0.0000572
Z′ 7 TeV mass, 1% width	/ZprimeToTT_M-7000_W-70_TuneCUETP8M1_13TeV-madgraphMLM-pythia8/RunIISummer16MiniAODv2-PUMoriond17_80X_mcRun2_asymptotic_2016_TrancheIV_v6-v1	96206	0.0000349

Table 5: Signal Monte Carlo samples used in the analysis, for the Z′ samples of 1% widths.

Sample	Dataset	Events	σ (pb), NLO
Z′ 1 TeV mass, 10% width	/ZprimeToTT_M-1000_W-100_TuneCUETP8M1_13TeV-madgraphMLM-pythia8/RunIISummer16MiniAODv2-PUMoriond17_80X_mcRun2_asymptotic_2016_TrancheIV_v6-v1	101056	44.853
Z′ 1.25 TeV mass, 10% width	/ZprimeToTT_M-1250_W-125_TuneCUETP8M1_13TeV-madgraphMLM-pythia8/RunIISummer16MiniAODv2-PUMoriond17_80X_mcRun2_asymptotic_2016_TrancheIV_v6-v1	96845	18.374
Z′ 1.5 TeV mass, 10% width	/ZprimeToTT_M-1500_W-150_TuneCUETP8M1_13TeV-madgraphMLM-pythia8/RunIISummer16MiniAODv2-PUMoriond17_80X_mcRun2_asymptotic_2016_TrancheIV_v6-v1	111108	8.476
Z′ 2 TeV mass, 10% width	/ZprimeToTT_M-2000_W-200_TuneCUETP8M1_13TeV-madgraphMLM-pythia8/RunIISummer16MiniAODv2-PUMoriond17_80X_mcRun2_asymptotic_2016_TrancheIV_v6-v1	104119	2.262
Z′ 2.5 TeV mass, 10% width	/ZprimeToTT_M-2500_W-250_TuneCUETP8M1_13TeV-madgraphMLM-pythia8/RunIISummer16MiniAODv2-PUMoriond17_80X_mcRun2_asymptotic_2016_TrancheIV_v6-v1	96077	0.734
Z′ 3 TeV mass, 10% width	/ZprimeToTT_M-3000_W-300_TuneCUETP8M1_13TeV-madgraphMLM-pythia8/RunIISummer16MiniAODv2-PUMoriond17_80X_mcRun2_asymptotic_2016_TrancheIV_v6-v1	189164	0.273
Z′ 3.5 TeV mass, 10% width	/ZprimeToTT_M-3500_W-350_TuneCUETP8M1_13TeV-madgraphMLM-pythia8/RunIISummer16MiniAODv2-PUMoriond17_80X_mcRun2_asymptotic_2016_TrancheIV_v6-v1	101022	0.113
Z′ 4 TeV mass, 10% width	/ZprimeToTT_M-4000_W-400_TuneCUETP8M1_13TeV-madgraphMLM-pythia8/RunIISummer16MiniAODv2-PUMoriond17_80X_mcRun2_asymptotic_2016_TrancheIV_v6-v1	102411	0.0516
Z′ 4.5 TeV mass, 10% width	/ZprimeToTT_M-4500_W-450_TuneCUETP8M1_13TeV-madgraphMLM-pythia8/RunIISummer16MiniAODv2-PUMoriond17_80X_mcRun2_asymptotic_2016_TrancheIV_v6-v1	84504	0.0259
Z′ 5 TeV mass, 10% width	/ZprimeToTT_M-5000_W-500_TuneCUETP8M1_13TeV-madgraphMLM-pythia8/RunIISummer16MiniAODv2-PUMoriond17_80X_mcRun2_asymptotic_2016_TrancheIV_v6-v1	107156	0.0143
Z′ 6 TeV mass, 10% width	/ZprimeToTT_M-6000_W-600_TuneCUETP8M1_13TeV-madgraphMLM-pythia8/RunIISummer16MiniAODv2-PUMoriond17_80X_mcRun2_asymptotic_2016_TrancheIV_v6-v1	96244	0.00550
Z′ 6.5 TeV mass, 10% width	/ZprimeToTT_M-6500_W-650_TuneCUETP8M1_13TeV-madgraphMLM-pythia8/RunIISummer16MiniAODv2-PUMoriond17_80X_mcRun2_asymptotic_2016_TrancheIV_v6-v1	98990	0.00374
Z′ 7 TeV mass, 10% width	/ZprimeToTT_M-7000_W-700_TuneCUETP8M1_13TeV-madgraphMLM-pythia8/RunIISummer16MiniAODv2-PUMoriond17_80X_mcRun2_asymptotic_2016_TrancheIV_v6-v1	98614	0.00266

Table 6: Signal Monte Carlo samples used in the analysis, for the Z′ samples of 10% widths.

Sample	Dataset	Events	σ (pb), NLO
Z′ 1 TeV mass, 30% width	`/ZprimeToTT_M-1000_W-300_TuneCUETP8M1_13TeV-madgraphMLM-pythia8/` `RunIISummer16MiniAODv2-PUMoriond17_80X_mcRun2_asymptotic_2016_TrancheIV_v6-v1`	79477	129.361
Z′ 2 TeV mass, 30% width	`/ZprimeToTT_M-2000_W-600_TuneCUETP8M1_13TeV-madgraphMLM-pythia8/` `RunIISummer16MiniAODv2-PUMoriond17_80X_mcRun2_asymptotic_2016_TrancheIV_v6-v1`	114009	7.742
Z′ 4 TeV mass, 30% width	`/ZprimeToTT_M-4000_W-1200_TuneCUETP8M1_13TeV-madgraphMLM-pythia8/` `RunIISummer16MiniAODv2-PUMoriond17_80X_mcRun2_asymptotic_2016_TrancheIV_v6-v1`	88039	0.289
Z′ 5 TeV mass, 30% width	`/ZprimeToTT_M-5000_W-1500_TuneCUETP8M1_13TeV-madgraphMLM-pythia8/` `RunIISummer16MiniAODv2-PUMoriond17_80X_mcRun2_asymptotic_2016_TrancheIV_v6-v1`	91038	0.0996
Z′ 6 TeV mass, 30% width	`/ZprimeToTT_M-6000_W-1800_TuneCUETP8M1_13TeV-madgraphMLM-pythia8/` `RunIISummer16MiniAODv2-PUMoriond17_80X_mcRun2_asymptotic_2016_TrancheIV_v6-v1`	89335	0.0434
Z′ 6.5 TeV mass, 30% width	`/ZprimeToTT_M-6500_W-1950_TuneCUETP8M1_13TeV-madgraphMLM-pythia8/` `RunIISummer16MiniAODv2-PUMoriond17_80X_mcRun2_asymptotic_2016_TrancheIV_v6-v1`	93070	0.0305
Z′ 7 TeV mass, 30% width	`/ZprimeToTT_M-7000_W-2100_TuneCUETP8M1_13TeV-madgraphMLM-pythia8/` `RunIISummer16MiniAODv2-PUMoriond17_80X_mcRun2_asymptotic_2016_TrancheIV_v6-v1`	96406	0.0221

Table 7: Signal Monte Carlo samples used in the analysis, for the Z′ samples of 30% widths.

Sample	Dataset	Events	σ (pb), LO × 1.3
RSG 1 TeV, ∼17% width	`/RSGluonToTT_M-1000_TuneCUETP8M1_13TeV-pythia8/RunIISummer16MiniAODv2-PUMoriond17_80X_mcRun2_asymptotic_2016_TrancheIV_v6-v1`	98560	20.05 × 1.3
RSG 1.25 TeV, ∼17% width	`/RSGluonToTT_M-1250_TuneCUETP8M1_13TeV-pythia8/RunIISummer16MiniAODv2-PUMoriond17_80X_mcRun2_asymptotic_2016_TrancheIV_v6-v1`	100000	7.92 × 1.3
RSG 1.5 TeV, ∼17% width	`/RSGluonToTT_M-1500_TuneCUETP8M1_13TeV-pythia8/RunIISummer16MiniAODv2-PUMoriond17_80X_mcRun2_asymptotic_2016_TrancheIV_v6-v1`	100000	3.519 × 1.3
RSG 2 TeV, ∼17% width	`/RSGluonToTT_M-2000_TuneCUETP8M1_13TeV-pythia8/RunIISummer16MiniAODv2-PUMoriond17_80X_mcRun2_asymptotic_2016_TrancheIV_v6-v1`	100000	0.9528 × 1.3
RSG 2.5 TeV, ∼17% width	`/RSGluonToTT_M-2500_TuneCUETP8M1_13TeV-pythia8/RunIISummer16MiniAODv2-PUMoriond17_80X_mcRun2_asymptotic_2016_TrancheIV_v6-v1`	100000	0.3136 × 1.3
RSG 3 TeV, ∼17% width	`/RSGluonToTT_M-3000_TuneCUETP8M1_13TeV-pythia8/RunIISummer16MiniAODv2-PUMoriond17_80X_mcRun2_asymptotic_2016_TrancheIV_v6-v1`	99755	0.1289 × 1.3
RSG 3.5 TeV, ∼17% width	`/RSGluonToTT_M-3500_TuneCUETP8M1_13TeV-pythia8/RunIISummer16MiniAODv2-PUMoriond17_80X_mcRun2_asymptotic_2016_TrancheIV_v6-v1`	99508	0.05452 × 1.3
RSG 4 TeV, ∼17% width	`/RSGluonToTT_M-4000_TuneCUETP8M1_13TeV-pythia8/RunIISummer16MiniAODv2-PUMoriond17_80X_mcRun2_asymptotic_2016_TrancheIV_v6-v1`	99136	0.02807 × 1.3

Table 8: Signal Monte Carlo samples used in the analysis, for the Randal-Sundrum Gluon samples of ∼17% widths.

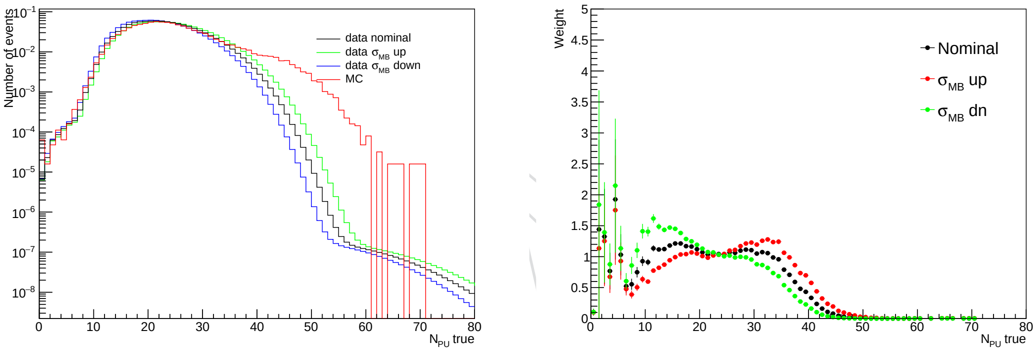

Figure 1: (left) Pileup distribution in data and Monte Carlo. (right) PU weight applied to Monte Carlo.

5 Event Selection

5.1 Trigger Selection

In this analysis we use the OR of the following jet HT, single jet, and groomed jet triggers.

- PFHT800
- PFHT900
- PFHT700TrimMass50
- AK8PFJet450
- PFJet360TrimMass30

In order to determine the best set of triggers for the analysis, we consider trigger efficiency as a function of H_T (Fig. 2), our sensitive variable dijet mass (Fig. 3), and both H_T and PUPPI softdrop mass (4). The H_T of the event is defined as the scalar sum of the p_T of every AK4CHS jet ($p_T^{\mathrm{AK4}} > 30$,$|\eta^{\mathrm{AK4}}| < 3.0$). Dijet mass is defined as the invariant mass of the two p_{T} leading jets. The efficiency is measured as the number of events that pass the numerator selection, trigger of interest OR Mu50 OR IsoMu24, divided by the number of events that pass the denominator selection, Mu50 OR IsoMu24. A preselection requirement, two AK8 jets with $|\Delta\phi > 2.1|$ and p_{T} >400 GeV, is applied to all plots. All three figures include efficiency plots with an additional preselection requirement that at least one jet have its mass in the top tag window ($105\,\mathrm{GeV}/c^2 < m_{SD} < 210\,\mathrm{GeV}/c^2$), as this requirement is made in both the signal region and background estimate sideband.

Comparing the trigger combinations in Fig. 2, we see that the combination of the triggers listed above is the most performant. Looking at the top left plot, we see that a cut of $H_T > 950$ GeV allows the analysis to have $> 99.8\%$ efficiency. In the left plot in Fig. 3, in which this 950 GeV H_T cut has been applied, we see that in the dijet mass region of interest ($M_{jj} > 1000$ GeV), the combination of triggers and preselection cuts allow us to achieve $> 99.9\%$ trigger efficiency. Additionally, considering the right plot in Fig. 4, it is evident that for events with $H_T > 950$ GeV, the analysis trigger selection is highly performant, and the efficiency as a function of H_T does not depend on jet mass.

5.2 Vertex Selection and Pileup Mitigation

Primary vertices are reconstructed using a deterministic annealing filtering algorithm [31]. The leading primary vertex of the event is defined as the primary vertex with the largest squared sum of transverse momenta of clustered physics objects.

Events are required to have a good primary vertex with “not fake”, $|z_{\mathrm{Primary\ Vertex}}| < 24$ cm, $N_{\mathrm{DOF}} > 4$, $|\rho| < 2$ cm.

Charged hadrons associated with subleading primary vertices are removed from further consideration. This is referred to as “charged hadron subtraction” (CHS). To combine these results with the lepton-plus-jets channel, we use CHS jets for the derivation of event kinematics. However, in order to mitigate the effects of pileup on the jet mass and substructure selection (see below), the Pileup Per Particle Identification (PUPPI) is used. This is more resilient to pileup than CHS for these observables.

5.3 Jet Reconstruction

Jets are clustered using the anti-kt R=0.8 algorithm [32] with both CHS and PUPPI inputs. In this analysis, jets are formed out of particle flow (PF) constituents [33]. Jets constructed with

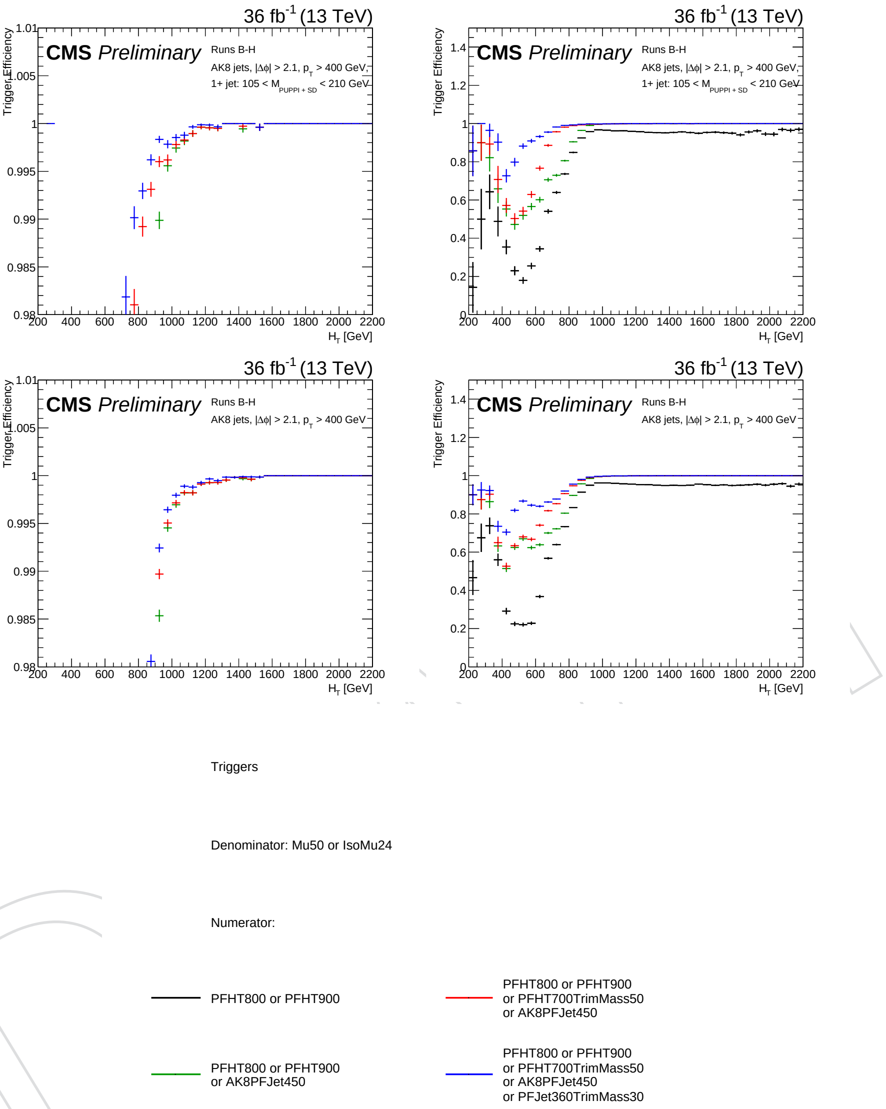

Figure 2: Trigger efficiency as a function of H_T. Plots in the right column use a y-axis range from 0.0 to 1.5, while plots the left column use a y-axis range from 0.98 to 1.01. All events are required to have two AK8 jets with $|\Delta\phi > 2.1|$ and p_T >400 GeV. The plots in row 1 include an additional requirement that each event contains at least one jet with its mass in the top mass window. Below the four efficiency plots, the legend describes the different combinations of jet HT, single jet, and groomed jet triggers compared here. Efficiencies are plotted with an OR of the Mu50 and IsoMu24 triggers in the denominator.

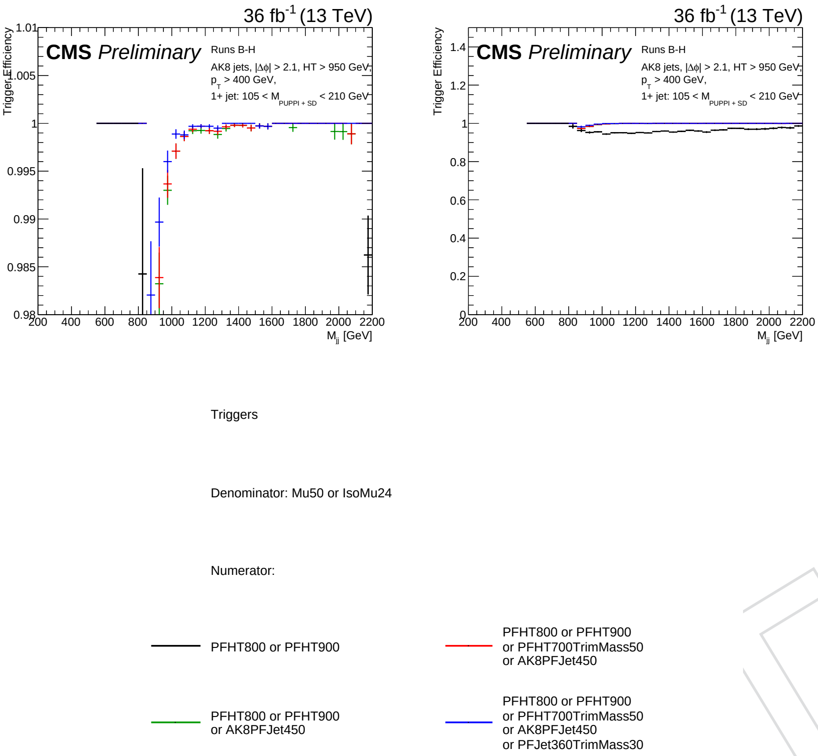

Figure 3: Trigger efficiency as a function of dijet mass, the sensitive variable of this analysis. The right plot has a y-axis range from 0.0 to 1.5, while the left plot has a y-axis range from 0.98 to 1.01. All events are required to have two AK8 jets with $|\Delta\phi > 2.1|$ and p_T >400 GeV, as well as at least one jet with its mass in the top mass window. Below the two efficiency plots, the legend describes the different combinations of jet HT, single jet, and groomed jet triggers compared here. Efficiencies are plotted with an OR of the Mu50 and IsoMu24 triggers in the denominator.

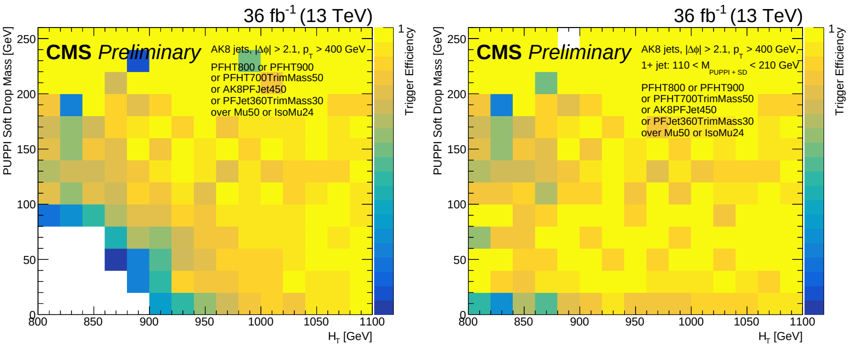

Figure 4: Trigger efficiency as a function of H_T (x-axis) and PUPPI softdrop mass (y-axis). Plots have a z-axis range from 0.98 to 1.0. All events are required to have two AK8 jets with $|\Delta\phi > 2.1|$ and p_T >400 GeV. The plot on the right includes an additional requirement that each event contains at least one jet with its mass in the top mass window. Efficiencies are plotted for the full analysis trigger selection, with an OR of the Mu50 and IsoMu24 triggers in the denominator.

CHS are referred to as “PFCHS”. Jets constructed with PUPPI are referred to as “PFPUPPI”. AK8CHS jets are used for kinematic variables such as p_{T} and dijet mass. AK8PUPPI jets are used only for top-tagging and subjet b-tagging. An AK8PUPPI jet is matched to each AK8CHS jet by finding the closest AK8PUPPI jet which also satisfies $\Delta R(CHS, PUPPI) < 1.0$.

Simulated jets are corrected with Summer16_23Sep2016V4 L1L2L3 corrections, while jets in data are corrected with L1L2L3+L2L3 residual corrections. The corrections derived for AK8CHS jets are applied to the AK8CHS 4-vector. This is done before any kinematic cuts are made. Corrections derived for AK8PUPPI jets are applied to the AK8PUPPI 4-vector.

We investigated three methods of correcting the AK8PUPPI groomed soft drop jet mass:

1. Apply AK8PUPPI corrections also to the groomed jet mass
2. Apply AK4PUPPI corrections to the individual soft drop subjets before calculating the groomed jet mass (the pairwise subjet mass)
3. Apply a specific jet mass correction developed for W-tagging

We find that the W-tagging based correction (correction method 3) induces a shift in the top-tagging mass peak as a function of p_{T} and therefore we choose not to use it. Neither method 1 nor method 2 results in a significant shift in the top mass peak location with increasing p_{T}. We find little difference between correction methods 1 and 2 and therefore we choose to use method 1 for simplicity (Fig. 5).

We account for differing jet energy resolutions between simulated events and data events. We apply the recommended eta-dependent smearing to simulated jets (Spring16 25nsV10) before requiring any kinematic selection on the jets. We employ the hybrid smearing method. We additionally smear the groomed jet mass by the same value used for the jet momentum.

The JME POG recommended Jet ID loose operating point is required. The Jet ID removes jets originating from detector noise with the following selection:

- PFJet Neutral Hadron Fraction < 0.99
- PFJet Neutral EM Fraction < 0.99
- PFJet Number of Constituents > 1
- PFJet Charged Hadron Fraction > 0
- PFJet Charged Multiplicity > 0
- PFJet Charged EM Fraction < 0.99

This jet ID definition is valid in the region $-2.7 < \eta < 2.7$. In our analysis jets are required to satisfy $-2.4 <$Y< 2.4.

5.4 Event Noise Filters

We require the following filters in order to reject noise events

- primary vertex filter
- beam halo filter (”Flag_globalTightHalo2016Filter”)
- HBHE noise filter (”Flag_HBHENoiseFilter”)
- HBHEiso noise filter (”Flag_HBHENoiseIsoFilter”)
- ECAL TP filter (”EcalDeadCellTriggerPrimitiveFilter”)

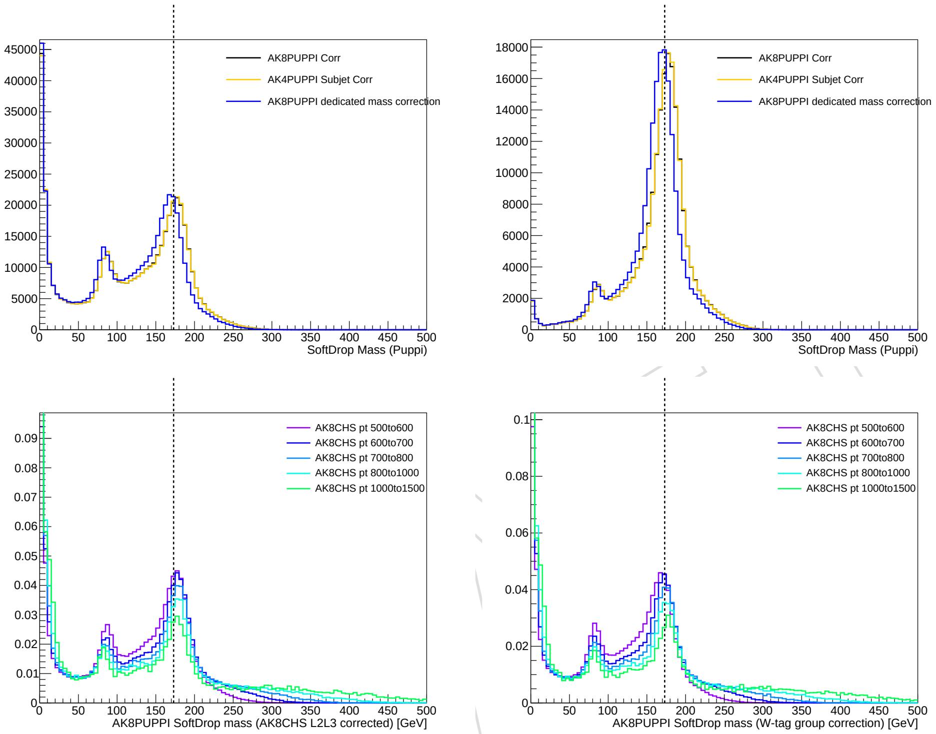

Figure 5: (top left) PUPPI soft drop mass in a $t\bar{t}$ MC sample comparing different mass correction methods. (top right) PUPPI soft drop mass after applying a τ_{32} cut in a $t\bar{t}$ MC sample comparing different mass correction methods. (bottom left) PUPPI soft drop mass corrected with AK8PUPPI JEC in different p_T regions. (bottom right) PUPPI soft drop mass corrected with the dedicated mass correction developed for W-tagging in different p_T regions. These plots show that corrections based on the W mass are inappropriate for the top quark tagger. We do not see much difference in mass when correcting the entire jet or each subjet. For simplicity, we therefore use the first option.

- Bad PF Muon Filter
- Bad Charged Hadron Filter
- ee badSC noise filter (data only)

5.5 Top p_{T} reweighting

As measured by the TOP PAG, the ratio of the top p_{T} in data with respect to the theory prediction exhibits a slope, and therefore a correction factor has been developed [34, 35]. The correction scale factor is given by $SF(p_T^{GEN}) = e^{0.0615-0.0005p_{\mathrm{T}}}$ and therefore the overall event weight becomes $W = \sqrt{SF(t)SF(\bar{t})}$. A comparison of the jet p_{T} distribution with and without top p_{T} reweighting is shown in Figure 6. Comparisons of event and jet kinematic variables is shown in Appendix B. We perform the analysis with top p_{T} reweighting applied to $\mathrm{t\bar{t}}$ MC for the main analysis, and we perform the analysis again, this time without top p_{T} reweighting, in order to measure the systematic uncertainty from this method.

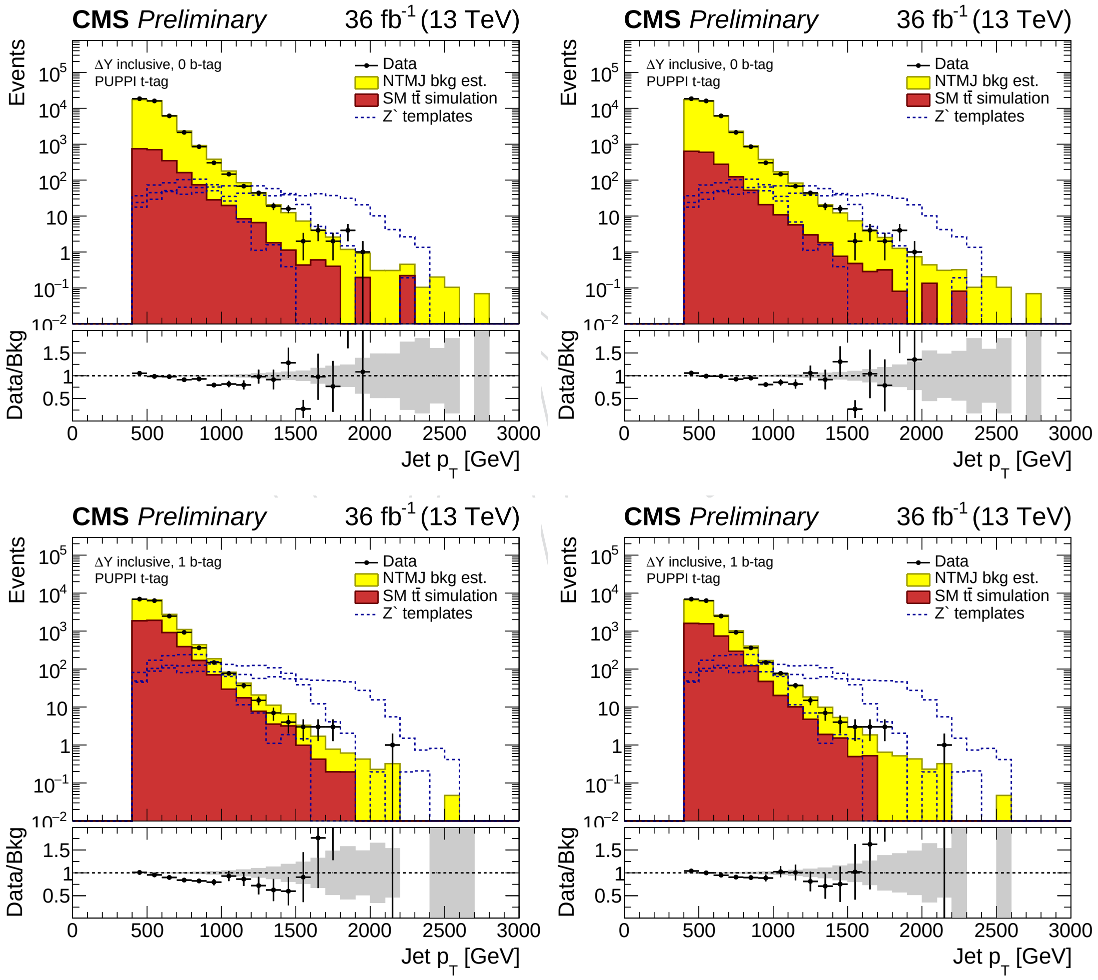

Figure 6: Jet p_{T} distribution in data compared to the data-driven NTMJ (described in section 6) and $\mathrm{t\bar{t}}$ MC backgrounds. (top left) 0 b-tag with no top p_{T} reweighting, (top right) 0 b-tag with top p_{T} reweighting, (bottom left) 1 b-tag with no top p_{T} reweighting, (bottom right) 1 b-tag with top p_{T} reweighting. The plots with top p_{T} reweighting applied show a somewhat better data/MC agreement.

5.6 Event Preselection

The following preselection is applied.

- The event is required to have at least two AK8CHS jets which satisfy:
  - $p_{\mathrm{T}} > 400\,\mathrm{GeV}/c$
  - HT > 950 GeV
  - $|y| < 2.4$
  - Loose jet ID (section 5.3)
- To select the back to back topology, we require the leading two jets to be separated by the azimuthal angle $\Delta\phi > 2.1$.
- Standard event noise cleaning filters (Section 5.4)

5.7 Top Tagging Algorithms

The products of hadronically decaying top quarks can fall within a single jet if the top quark is highly boosted relative to its mass. Special tools, known as top-tagging algorithms, are designed to identify these boosted decay topologies.

5.7.1 CMS Top Tagger Version Two

This algorithm uses a combination of substructure techniques for tagging top jets. For highly boosted tops ($p_{\mathrm{T}} > 400\,\mathrm{GeV}/c$), we use CMS top tagger version two for high p_{T} (CMSTT V2H), which takes anti-k_t R = 0.8 PUPPI jets as inputs (where $R = \sqrt{\Delta\eta^2 + \Delta\phi^2}$) [36]. The input AK8 jets are hereby referred to as the "hard jets." The following variables, defined for each jet passing the algorithm, are used to tag top jets:

- **Softdrop Jet Mass m_{jet}** - The mass of the four-vector sum of the constituents of the hard jet, after the application of the softdrop ($z = 0.1, \beta = 0$) algorithm. Softdrop [37] iteratively declusters a jet j with distance parameter R into two subjets, j_1 and j_2. If the softdrop condition

$$\frac{\min(p_{T1}, p_{T2})}{p_{T1} + p_{T2}} > z_{cut} \cdot (\frac{\Delta R_{12}}{R})^{\beta} \tag{1}$$

  is met, then the procedure stops and j is the final jet. Otherwise, the declustering continues - the higher p_{T} subjet is relabeled as j and the lower p_{T} one is dropped. CMSTT V2 sets the tuneable parameters z_{cut} and β to 0.1 and 0, respectively. In the process, soft and wide-angle particles (relative to the parent in the clustering) are removed. For the case $\beta = 0$, the soft drop groomer is identical to the modified mass drop groomer [38]. A cut of $105\,\mathrm{GeV}/c^2 < m_{SD} < 210\,\mathrm{GeV}/c^2$ is applied as part of the CMS V2H top tagging algorithm as recommended by the CMS JetMET Algorithms and Reconstruction group [39].
- **N-Subjettiness τ_3/τ_2** - N-subjettiness is an algorithm [40] designed to determine the consistency of a jet with N number (or fewer) of subjets. Jet axes are found for an N subjet hypothesis, using the one-pass optimization algorithm. The consistency of the particle flow candidates with the individual axes is then determined, and N-

subjettiness is calculated according to the following formula:

$$\tau_N = \frac{\sum\limits_{i \in \text{particles}} p_T^i \cdot \min(\Delta R_{1,i}, \Delta R_{2,i}, \ldots, \Delta R_{N,i})}{\sum\limits_{i \in \text{particles}} p_T^i \cdot R_{jet}}.$$

Here, the quantities $\Delta R_{j,i}$ represent the angular distances between particle i and subjet axis j, where j ranges between 1 and N to compute N-subjettiness. The normalization factor in the denominator uses R_{jet}, the distance parameter used for jet clustering (0.8 in our case). Jets with low values of τ_N have particle deposits that are more aligned with the hypothesized number and position of the subjet axes, while higher values of τ_N are found for jets inconsistent with a given hypothesis. Additional discrimination between signal and background jets can be obtained by taking ratios of successive τ_N values. We use the ratio of 3-subjettiness to 2-subjettiness to increase identification efficiency and background rejection of top quark candidates. The CMS JetMET Algorithms and Reconstruction group provides several τ_3/τ_2 working points to be used as part of the CMS V2H top tagging algorithm [39]. We apply a cut of $\tau_3/\tau_2 < 0.65$, which was found to be most optimal for this analysis (see Section 5.9). Both the soft drop mass and N-subjettiness are calculated using PUPPI PF inputs.

We separate the subjet b-tagging definition from the t-tagging definition in order to later divide event categories based on the number of identified subjet b-tags.

In this analysis we calculate the t-tagging variables τ_3/τ_2 and m_{SD} from PUPPI inputs. The PUPPI-based t-tagging algorithm demonstrates relatively stable tagging efficiency for all pileup conditions observed in 2016 (Fig. 7).

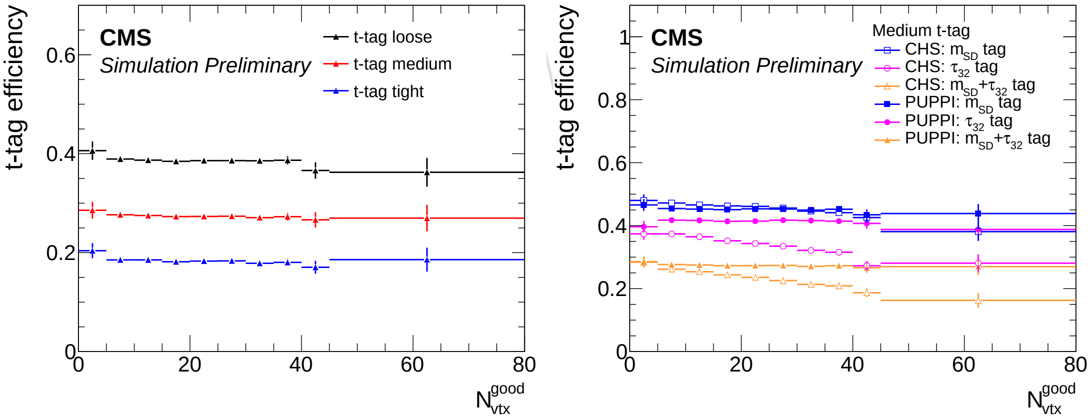

Figure 7: (left) PUPPI t-tag efficiency for 3 different working points (right) t-tag efficiency for CHS and PUPPI based variables. Three tag definitions are consdiered: m_{SD} only, τ_{32} only, $m_{SD} + \tau_{32}$. The pileup dependence of CHS is still significant in the pileup regime of interest, whereas the dependence of PUPPI is flat. We therefore use the PUPPI-based variables for substructure tagging.

Figure 8 shows a comparison of the relevant CMSTT quantities in data, simulated $t\bar{t}$, and simulated QCD events. The discrimination power of each observable can be seen – each variable is shown with the requirements already placed on the other two quantities. In this way, one can ascertain the independent discrimination power offered by each variable. Some disagreement is observed due to the lack of scale factors available for cutting on a single top-tagging variable. In these plots, there is a t-tag SF applied to the opposite t-tagged jet, but no SF is applied to the N-1 tagged jet. The application of soft drop jet mass resolution scale factors, as yet unmeasured for top jets, might also improve the agreement.

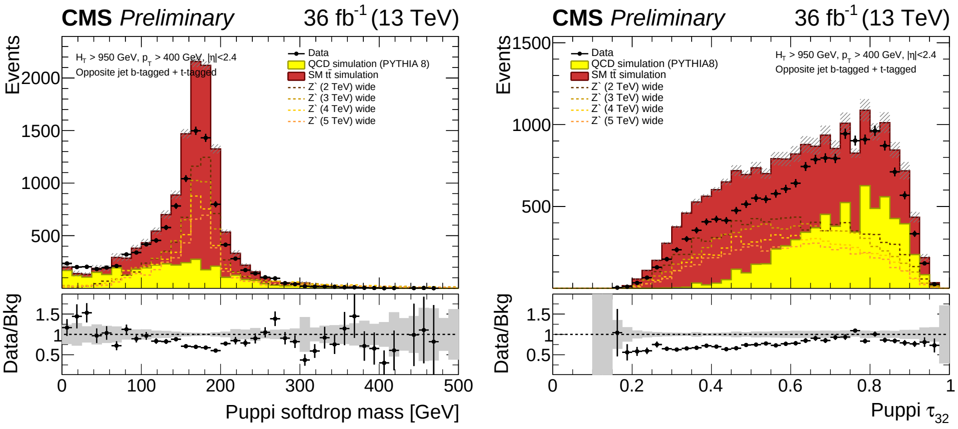

Figure 8: Comparison of data, background simulation, and signal simulation, for each of the quantities used in CMSTT V2H: AK8 PUPPI jet soft-drop mass (left) and AK8 PUPPI jet τ_3/τ_2 value (right). Each plot is made requiring the CMSTT V2H selection with the exception of the variable being plotted.

5.8 Subjet b-tagging

Subjet b-tagging is used to categorize events (see next section). We apply the standard CMS b-quark ID combined secondary vertex (CSVv2) algorithm [41] (pfCombinedInclusiveSecondaryVertexV2BJetTags) to the subjets found using the softdrop algorithm running on AK8PUPPI jets, as described above. We consider a subjet to be b-tagged if the CSV discriminant is greater than 0.8484, corresponding to the medium-efficiency working point (CSVv2M). The loose working point was also considered but was found to be sub-optimal (see Section 5.9). There is no official tight subjet b-tagging working point.

Figure 9 shows the distribution of the maximum subjet b-tag discriminant of the p_T-leading top-jet candidate in data, simulated tt̄, and simulated QCD events. Both the jet plotted and the opposite AK8 jet have been top tagged. The discrimination power of the b-tagging algorithm, even after top-tagging, can be seen – at high CSV discriminant values, the tt̄ peaks while the QCD remains relatively flat. Some disagreement in the normalization of the data and MC is observed, due to the use of QCD MC instead of the data driven background estimate.

The subjet b-tag rate differs in data and in simulation and therefore subjet b-tagging scale factors are applied. We use scale factors provided by the BTV POG with tag:

```
subjet_CSVv2_Moriond17_B_H.csv
```

In order to properly account for the migration of events from one b-tag category to another when applying the scale factors, we employ the “jet-by-jet updating method”([42]), or in our case a “subjet-by-subjet updating method”. This method is defined as follows: each subjets’s b-tagging status is upgraded or downgraded based on the scale factor and a random number.

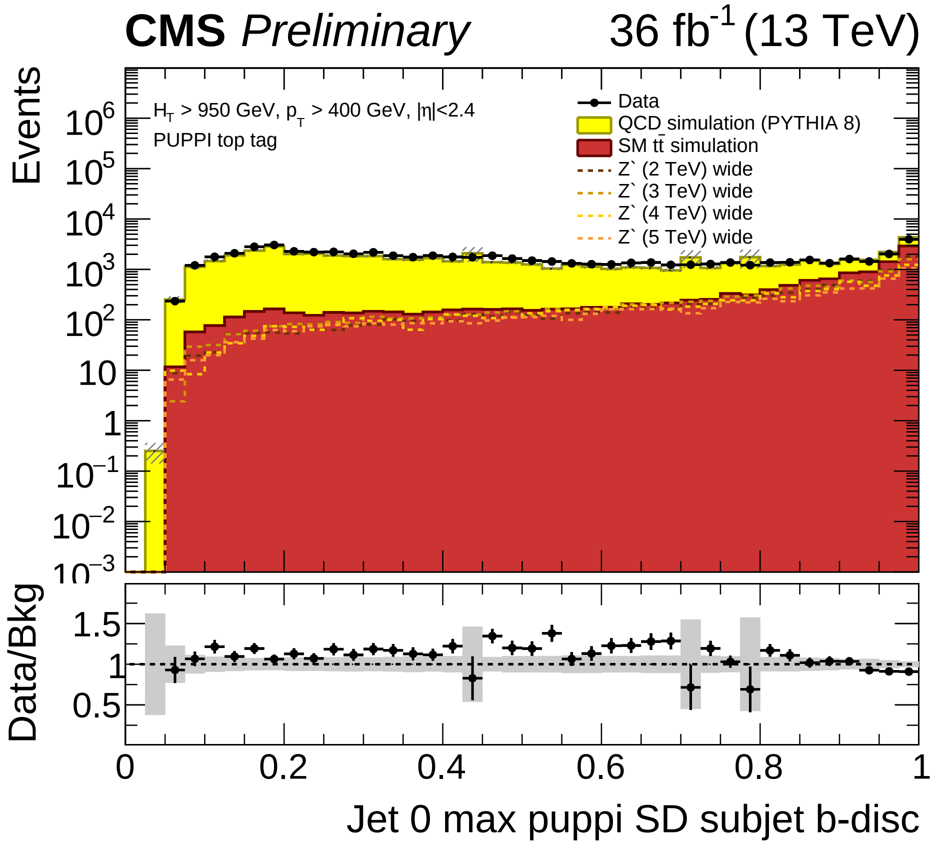

Figure 9: Comparison of data, background simulation, and signal simulation, for the maximum subjet b-tag discriminant of the p_T-leading top-jet candidate. The plot is made requiring the CMSTT V2H selection on both of the leading AK8 jets in the event.

For scale factors less than 1, b-tagged subjets are downgraded based on the fraction $f = 1 - \mathrm{SF}$, while for scale factors greater than 1, untagged subjets are upgraded based on the fraction $f = (1-\mathrm{SF})/(1-1/\epsilon_{MC})$, where ϵ_{MC} is the b-tagging Monte Carlo efficiency. With this procedure the fraction of events in each b-tagging category is modified. The b-tag efficiency for different subjet hadron flavors (ϵ_{MC}) has been measured separtely for each Monte Carlo sample. Subjet b-tag scale factors depend on the flavor of the subjet, and therefore we use the hadron flavor of each subjet when finding the correct scale factor. Figs. 10 – 12 show selected $\mathrm{t\bar{t}}$ and Z′ b-tag efficiencies. Due to limited statistics when measuring the b-tag SF, the BTV POG recommends that the scale factor uncertainty should be doubled for subjets with p_{T} outside of the range 20-1000 GeV/c for udsg flavor subjets and outside of the range 30-450 GeV/c for b and c flavor subjets.

We consider an AK8 jet to contain a subjet b-tag if, after applying the subjet-by-subjet updating procedure, the jet contains at least one b-tagged subjet. We then categorize events based on the number of jets containing at least one subjet b-tag (see Section 5.9).

5.9 Signal region and event categorization

Given the back-to-back high p_{T} dijet events selected by the preselection (Section 5.6), our signal region is defined to be events containing two top-tagged jets.

We observe that for high dijet mass the rapidity difference (ΔY) between the two top-tagged jets can be used to further discriminate signal from background (Figure 13). We therefore categorize signal region events into the regions defined by ΔY<1 and ΔY>1.

Subjet b-tagging can also be used to discriminate signal from background. We therefore further categorize events based on the number of jets containing a subjet b-tag (0,1, or 2).

In order to optimize our selection we consider the 2 subjet b-tagging working points and 3 top-tagging working points provided by the CMS Physics Object Groups.

The b-tag working points are:

- Medium operating point (M): CSV> 0.8484
- Loose operating point (L): CSV> 0.5426

The top-tagging working points are:

- Working point A : $105\,\mathrm{GeV}/c^2 < m_{SD} < 210\,\mathrm{GeV}/c^2$ and $\tau_3/\tau_2 < 0.80$ (loose, $\epsilon_B = 3\%$)
- Working point B : $105\,\mathrm{GeV}/c^2 < m_{SD} < 210\,\mathrm{GeV}/c^2$ and $\tau_3/\tau_2 < 0.65$ (medium $\epsilon_B = 1\%$))
- Working point C : $105\,\mathrm{GeV}/c^2 < m_{SD} < 210\,\mathrm{GeV}/c^2$ and $\tau_3/\tau_2 < 0.54$ (tight $\epsilon_B = 0.3\%$))

Given the 6 event categories, we calculate discovery significance (Figure 14) and expected limits (Figure 15) for each combination of b-tag and top-tag working points. We find that the medium b-tag working point and top-tagging working point B are close to optimal and also match what is used for the semi-leptonic Z′ analysis. Therefore we choose to use this combination of working points.

These categories uses in this analysis are summarized in Table 9.

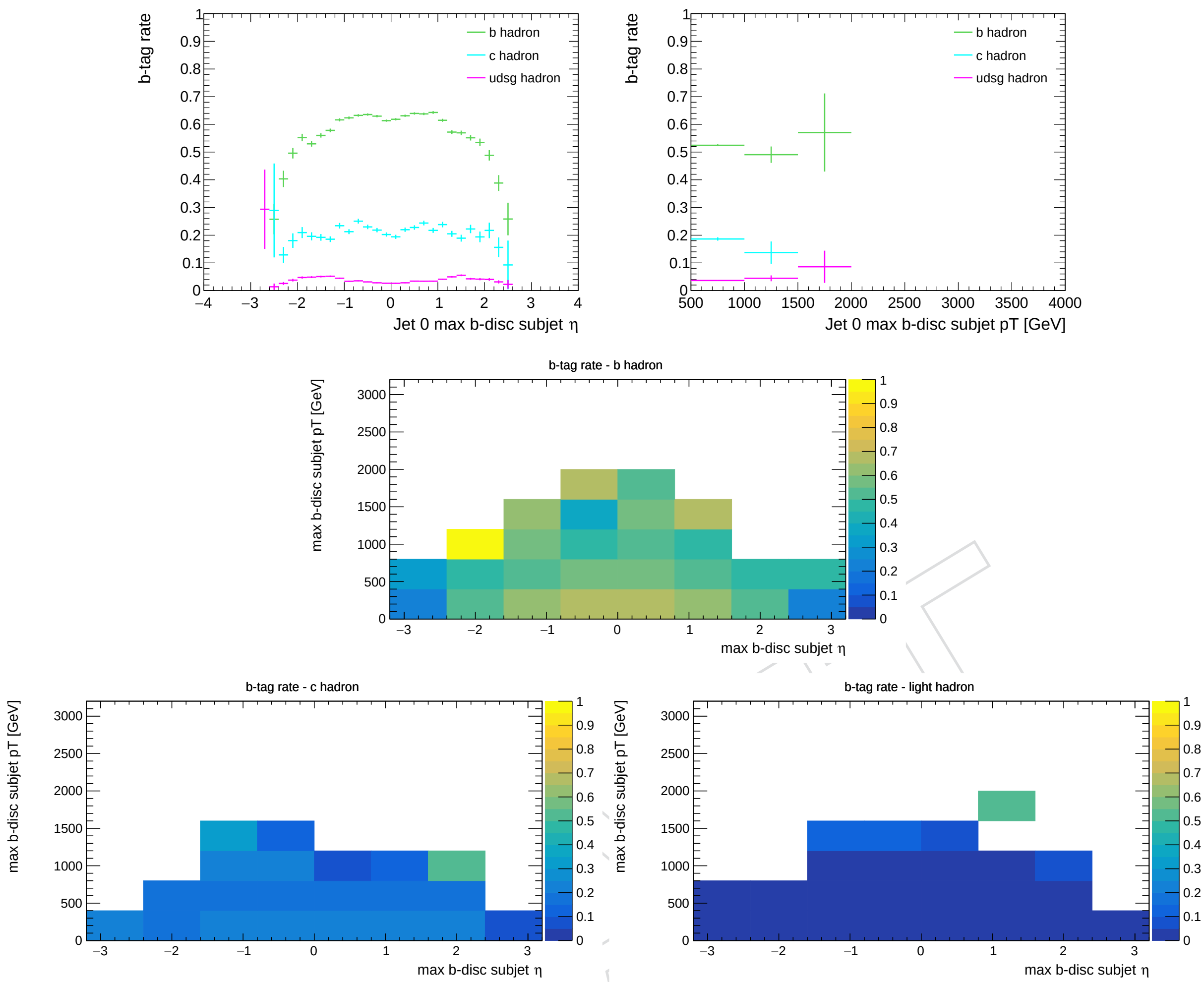

Figure 10: b-tag rate of the subjet with the maximum b-discriminant for the medium operating point as measured in a simulated $t\bar{t}$ sample. (a) b-tag rate as a function of the subjet η for subjets of different hadron flavor (b) b-tag rate as a function of the subjet p_T for subjets of different hadron flavor (c) The b-tag rate for a given subjet p_T and η for subjets originating from b-hadrons (d) The b-tag rate for a given subjet p_T and η for subjets originating from c-hadrons (e) The b-tag rate for a given subjet p_T and η for subjets originating from udsg-hadrons

Event Category	PUPPI Softdrop jet mass window	τ_3/τ_2 Cut	$\lvert\Delta y\rvert$ Cut	Number of jets with a CSVM b-tagged subjet
A	$105-210$	< 0.65	< 1.0	0
B	$105-210$	< 0.65	< 1.0	1
C	$105-210$	< 0.65	< 1.0	≥ 2
D	$105-210$	< 0.65	> 1.0	0
E	$105-210$	< 0.65	> 1.0	1
F	$105-210$	< 0.65	> 1.0	≥ 2

Table 9: Event selections defining the six categories used in the analysis.

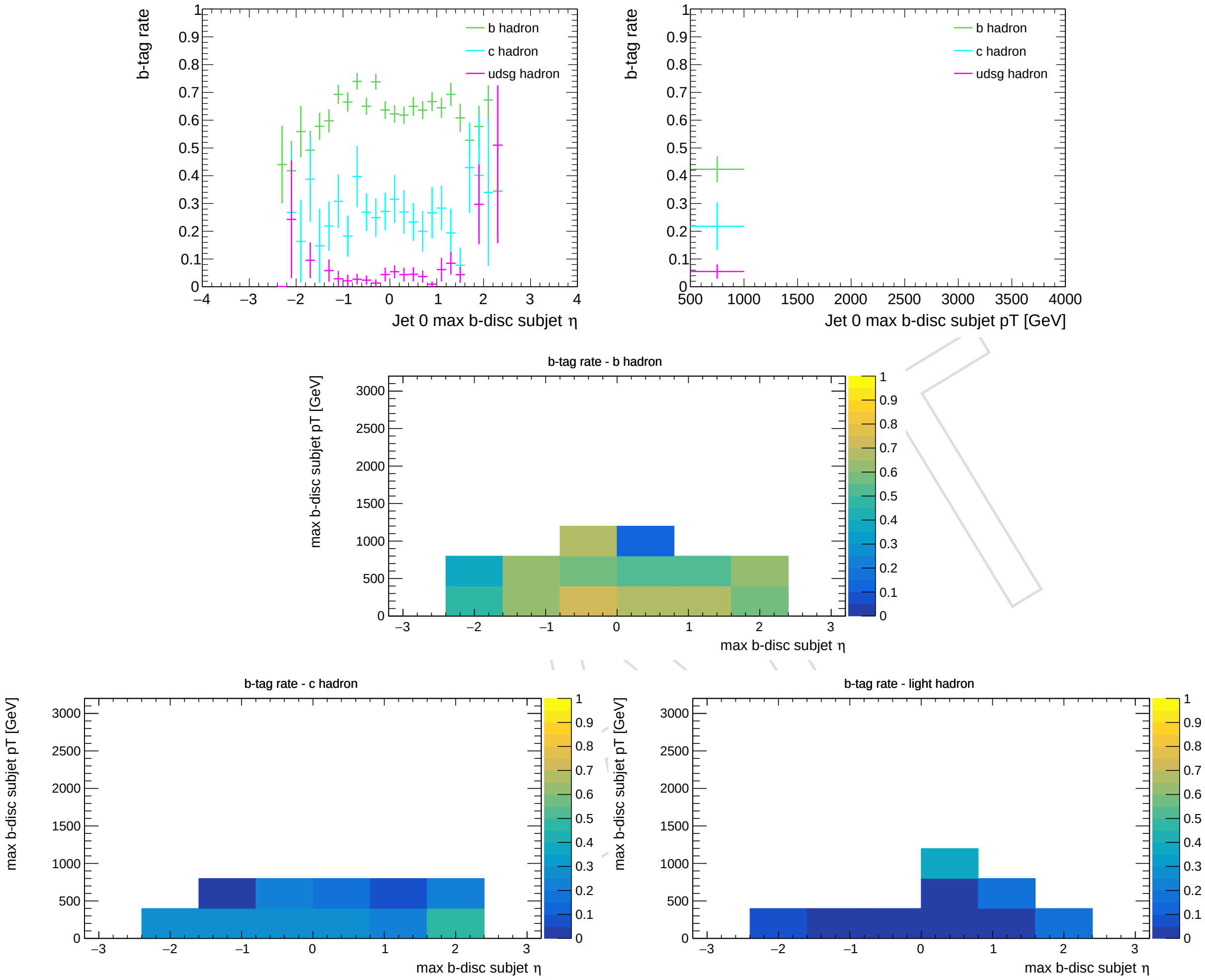

Figure 11: b-tag rate of the subjet with the maximum b-discriminant for the medium operating point as measured in a simulated narrow 1 TeV Z' sample. (a) b-tag rate as a function of the subjet η for subjets of different hadron flavor (b) b-tag rate as a function of the subjet p_T for subjets of different hadron flavor (c) The b-tag rate for a given subjet p_T and η for subjets originating from b-hadrons (d) The b-tag rate for a given subjet p_T and η for subjets originating from c-hadrons (e) The b-tag rate for a given subjet p_T and η for subjets originating from udsg-hadrons

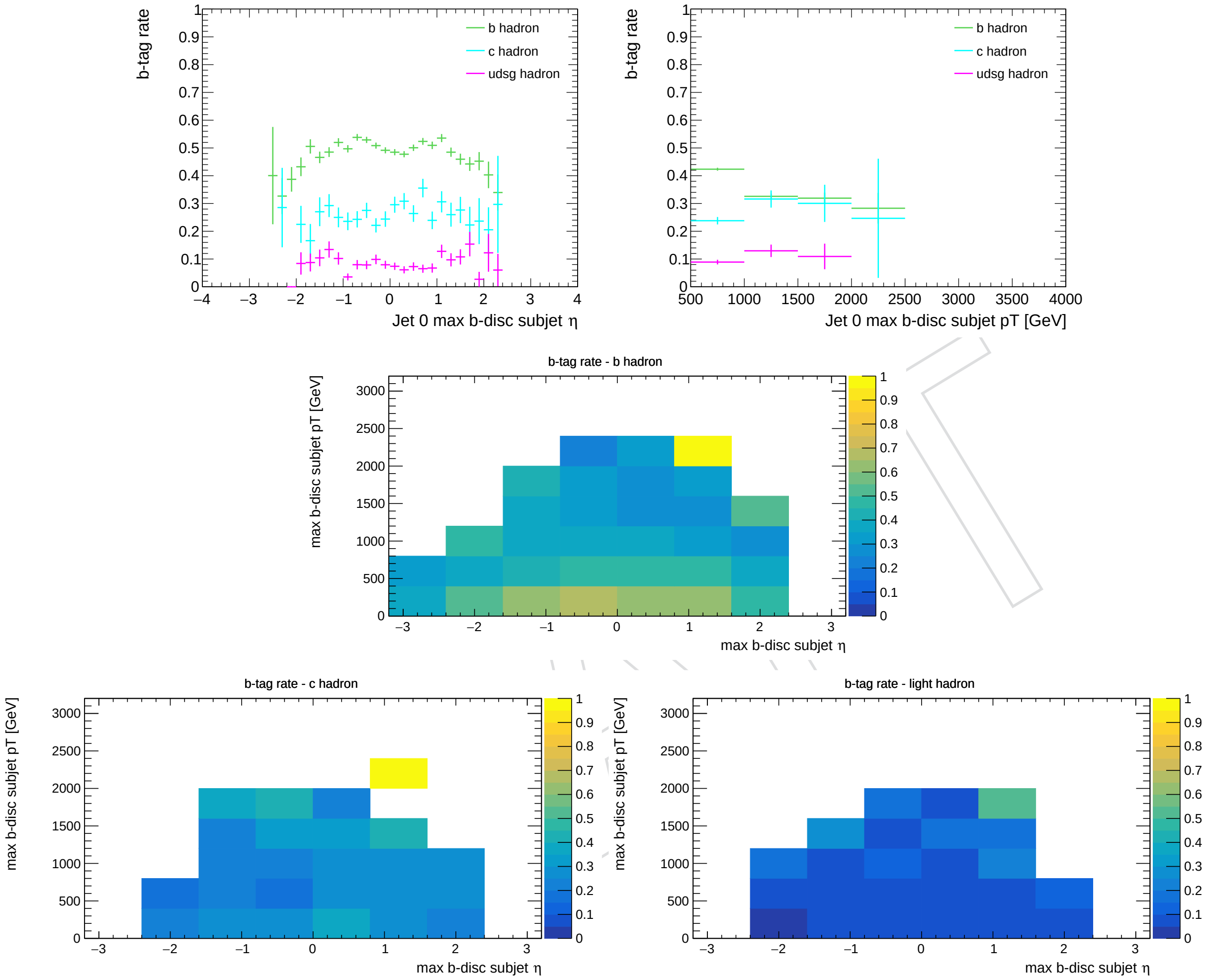

Figure 12: b-tag rate of the subjet with the maximum b-discriminant for the medium operating point as measured in a simulated extra-wide 5 TeV Z' sample. (a) b-tag rate as a function of the subjet η for subjets of different hadron flavor (b) b-tag rate as a function of the subjet p_{T} for subjets of different hadron flavor (c) The b-tag rate for a given subjet p_{T} and η for subjets originating from b-hadrons (d) The b-tag rate for a given subjet p_{T} and η for subjets originating from c-hadrons (e) The b-tag rate for a given subjet p_{T} and η for subjets originating from udsg-hadrons

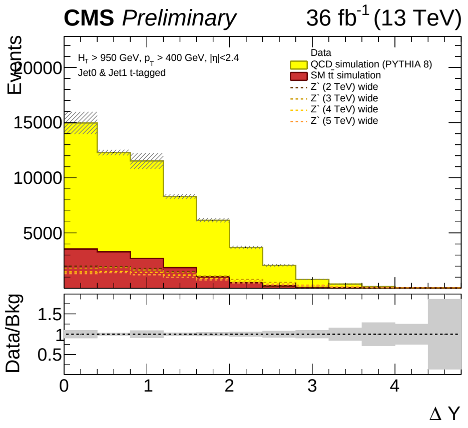

Figure 13: Dijet rapidity difference after requiring two t-tagged jets (a) ΔY (inclusive in m_{tt}) (b) ΔY ($m_{tt} > 2\,\text{TeV}/c^2$)

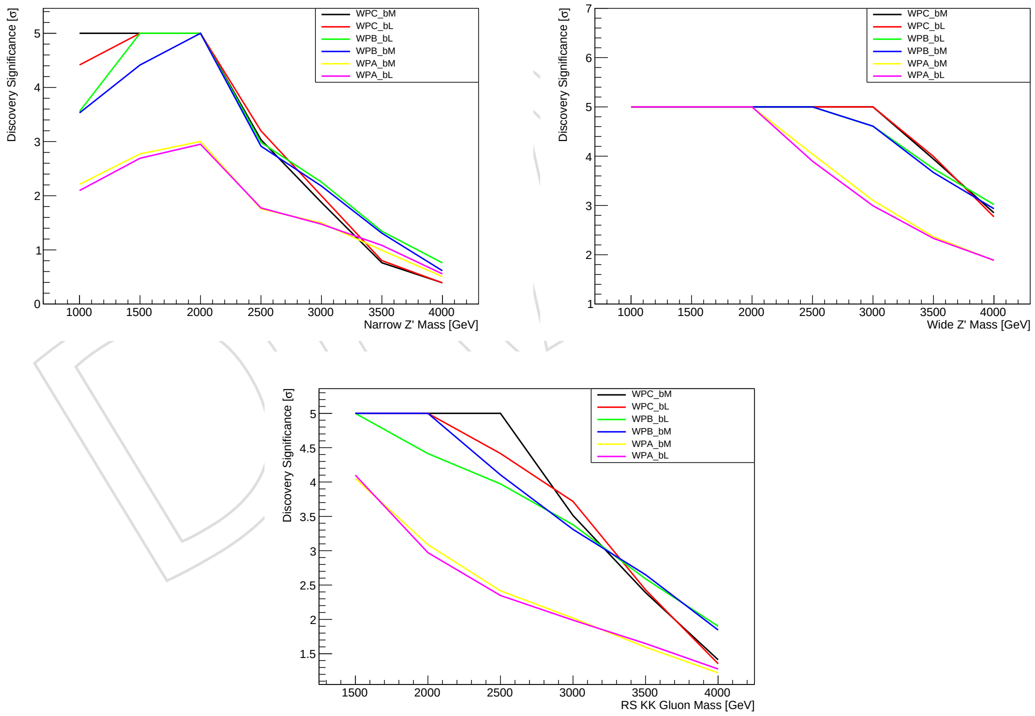

Figure 14: Discovery significance for the full analysis using the 6 event categories for different top tagging working points A,B,C and b-tag working points bL (Loose) or bM (Medium). The three models considered are a Z' boson whose width is 1% of its mass (upper left), a 10% width Z' boson (upper right), and an RS KK gluon (bottom). Working point B is optimal at high masses, which have not yet been excluded by previous searches.

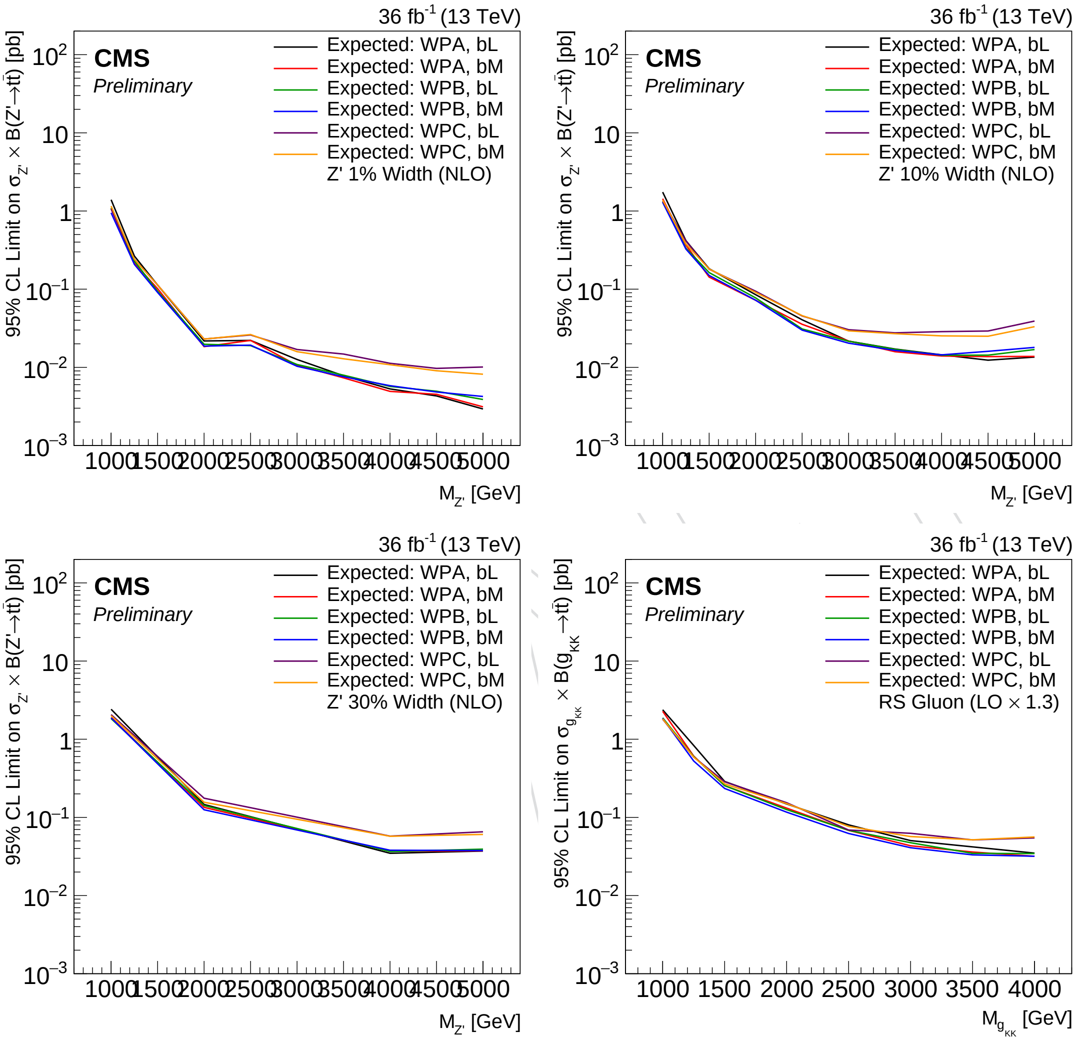

Figure 15: Expected limits for the full analysis using the 6 event categories for different top tagging working points A,B,C and b-tag working points bL (Loose) or bM (Medium). The four models considered are a Z′ boson whose width is 1% of its mass (upper left), a 10% width Z′ boson (upper right), a 30% width Z′ boson (lower left), and an RS KK gluon (lower right).

6 Background Estimation

This analysis has two sources of background: multijet events originating from non-top QCD interactions (non-top multijet, i.e., NTMJ), that will be determined from data, and SM $\mathrm{t\bar{t}}$ events, determined from simulated events. This section describes the methods for estimating the various background contributions.

6.1 Data-derived Backgrounds

For the non-top multijet estimate, we use a data-derived technique. This technique is similar to that described in Ref. [21]. The method involves selecting a sample with low SM $\mathrm{t\bar{t}}$ contribution. This is done by first selecting events with two AK8CHS jets that meet the preselection requirements described in Section 5.6. Next, the top tagging requirements are inverted on one selected jet (anti-tag), and the top tagging rate is determined for the second jet (probe). This 'anti-tag and probe' method yields a per-jet mistag rate that is then applied to each jet in the event to determine the estimated number of NTMJ background events. This mistag rate is parameterized as a function of jet p (not p_{T}, but the full momentum) and is measured separately for events falling into each of the 3 b-tag categories inclusive in delta rapidity.

The mistag rate is determined by the following procedure for the CMS Top Tagger analysis:

1. We select dijet events in the type 1+1 topology, with the leading two AK8 jets required to have p_T greater than 400 GeV. The two jets also have additional kinematic requirements similar to those used in the main selection: hemispheric separation ($|\Delta\phi| > 2.1$) is required, as well as requirements that the event fall into one of the b-tag and rapidity difference bins as described in table 9.

2. One jet is selected at random – this jet is "anti-tagged" to select an enriched sample of NTMJ events. This jet must pass an inverted N-subjettiness selection ($\tau_3/\tau_2 > 0.65$) and the softdrop jet mass must be in the top mass window (105-210 GeV) .

3. Once the anti-tagged jet is selected, the second jet is then used as the probe jet.

4. The top tagging rate of the probe jet is taken as the mistag rate for the algorithm. The mistag rate is measured as a function of jet p and is measured separately for events falling into each of the three b-tag categories. Due to the inversion of the τ_3/τ_2 cut, the data sample is dominated by multijet events in the right kinematic regime, and is therefore an appropriate control region to extract the mistag rate.

The mistag rate is measured both in an NTMJ rich data sample and in $\mathrm{t\bar{t}}$ MC. The $\mathrm{t\bar{t}}$ contamination from the tag and probe distributions is subtracted before calculating the mistag rate. Table 10 shows the the anti-tag and probe event yields for $\mathrm{t\bar{t}}$ MC and data in each of the 6 event categories. Figure 16 shows the mistag rate as measured in data for each b-tag category and Figure 17 compares the mistag rate measured in data to QCD simulation. We see better data/MC agreement for the QCD samples simulated with PYTHIA 8. This is not unexpected, as problems have been observed in some of the other samples simulated with MADGRAPH.

Once the mistag rate is determined from the NTMJ control sample, we can use it to estimate the normalization and shape of NTMJ events passing the final event selection. To do this, we use a "pre-tagged" region which contains events with at least one t-tagged jet. In order to avoid bias, we randomly select one of the two leading jets, which pass the preselection, and ask that

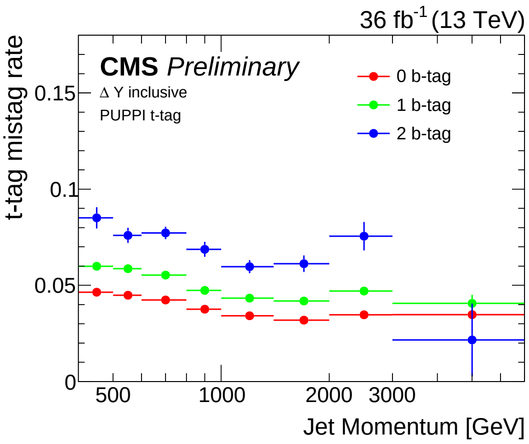

Figure 16: t-tagging mistag rate as measured with an anti-tag and probe procedure separately for each b-tag category

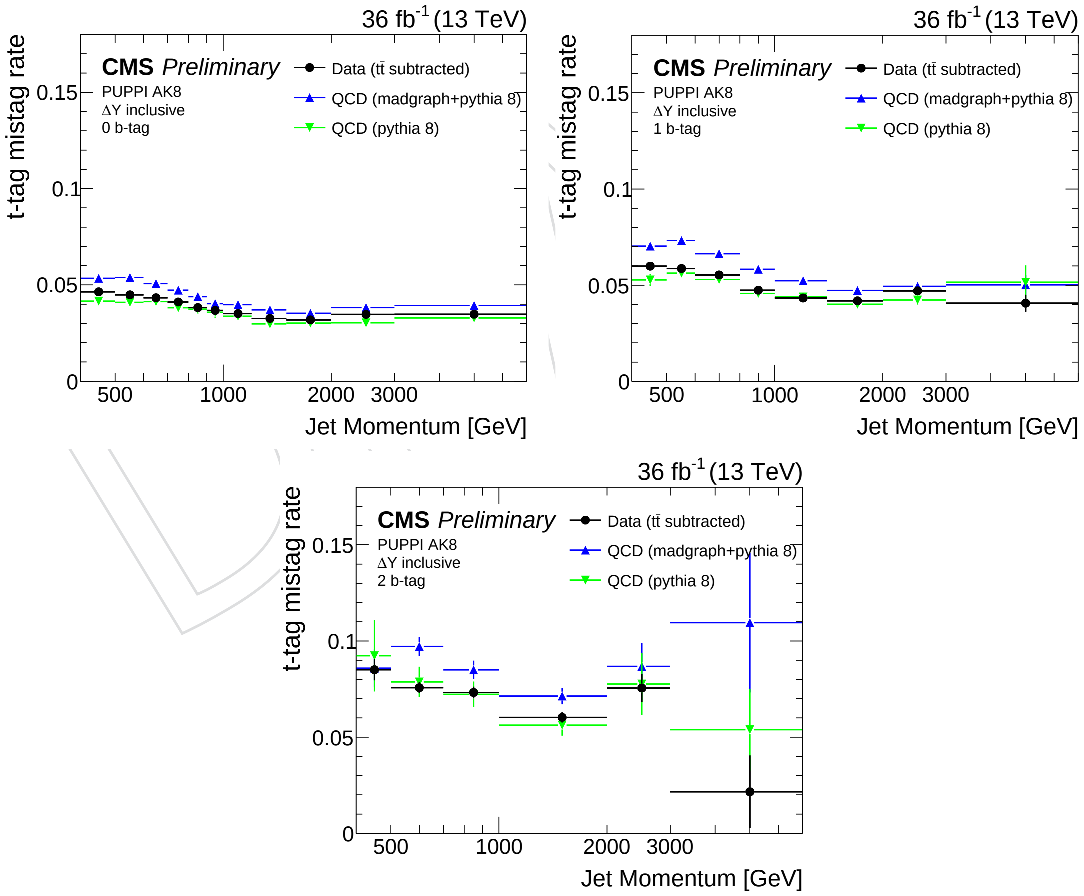

Figure 17: t-tagging mistag rate measured in data and in QCD simulation with the anti-tag and probe procedure: (a) 0 b-tag category (b) 1 b-tag category (c) 2 b-tag category

Sample	Event Category	Probe event yields	Tag event yields
$\mathrm{t\bar{t}}$	$\Delta Y>1$, 0 b-tag	3104	594
$\mathrm{t\bar{t}}$	$\Delta Y>1$, 1 b-tag	4670	1200
$\mathrm{t\bar{t}}$	$\Delta Y>1$, 2 b-tag	1202	513
$\mathrm{t\bar{t}}$	$\Delta Y<1$, 0 b-tag	3976	864
$\mathrm{t\bar{t}}$	$\Delta Y<1$, 1 b-tag	6614	1848
$\mathrm{t\bar{t}}$	$\Delta Y<1$, 2 b-tag	2051	905
Data	$\Delta Y>1$, 0 b-tag	1710380	67049
Data	$\Delta Y>1$, 1 b-tag	370824	19570
Data	$\Delta Y>1$, 2 b-tag	21486	1912
Data	$\Delta Y<1$, 0 b-tag	1685670	68945
Data	$\Delta Y<1$, 1 b-tag	375487	21168
Data	$\Delta Y<1$, 2 b-tag	23202	2477

Table 10: Data and $\mathrm{t\bar{t}}$ yields for the tag and probe histograms

it pass the CMSTT V2H selection described above. If the randomly chosen jet is indeed top-tagged, we use this event and weight the event by the appropriate mistag rate after finding the appropriate bin of the second jet p value. There is no selection applied on this second jet, and if the randomly chosen first jet is not tagged, the event is not used to model the multijet background.

To model the individual signal region categories with differing numbers of b-tagged jets and rapidity separations, we apply the same selections to the events weighted by the mistag rate as those applied to the signal region. For example, in the 1 b-tag category with $|\Delta y| < 1.0$, we require this weighted event to have exactly 1 b-tagged jet (it can be either the already tagged jet or the second jet used to determine the mistag rate), and to also have the two jets separated by a rapidity difference of no more than 1.0 units. Analogous selections are applied for the remaining signal regions.

Using this single-tagged control region without any requirements on the second jet leads to an overlap between the signal region and this region used to estimate the multijet background. To remove the effects of double-counting, the $\mathrm{t\bar{t}}$ contribution should be subtracted from the multijet estimate. This is done by evaluating the mistag weighting procedure described above on the simulated $\mathrm{t\bar{t}}$ events, to find the amount of 'mistagged $\mathrm{t\bar{t}}$'. Generally, this 'mistagged $\mathrm{t\bar{t}}$' makes up about 1–2% of the NTMJ background estimate in the 0 b-tag event regions, and about 6–10% in the other regions.

As a final step to the shape determination of the NTMJ estimate, we use a so-called 'mass-modified' procedure to account for the fact that the second jet, having no tag selection applied, will have different kinematics than the jets in the signal region, which have a jet mass requirement. To mimic the kinematics of the signal region, we set the mass of this second jet 'by hand' to follow a distribution of jet masses from simulated QCD events in the same window used for the signal region selection, $105 < m_{SD} < 210$ GeV. The specific mass is chosen by drawing randomly from this distribution of QCD jet masses. Figure 18 shows the Soft drop mass distributions used in 'mass-modified' procedure for the two leading jets.

6.2 Closure Tests for the CMS Top Tagger V2H Analysis

To validate the method described above to estimate the NTMJ background, we perform the background estimate procedure using a sideband tag definition in data. Here we use the same event categories and N-subjettiness selection but a separate soft drop mass selection (40-105

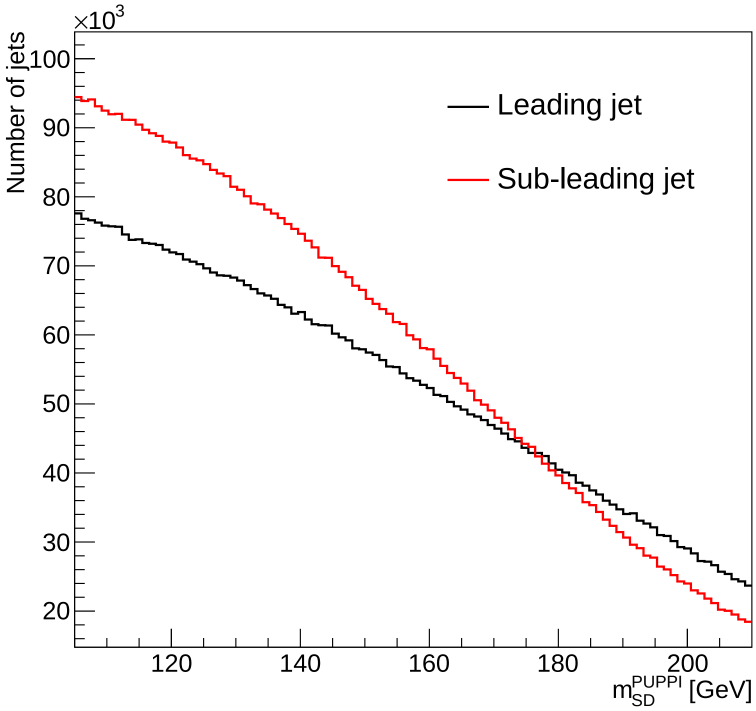

Figure 18: Soft drop mass distributions for the event leading and sub-leading jet as measured in the data pre-selection. These distributions are used for the mass-modified procedure.

GeV/c^2). The mistag rate for this tag definition is shown in Figure (19). Using this tag definition we observe good closure between the background estimate and the double sideband tagged signal region in the individual event categories (Figure 20).

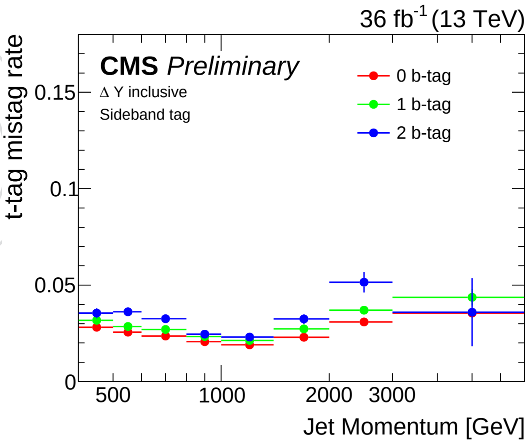

Figure 19: Sideband tag mistag rate as measured with an anti-tag and probe procedure separately for each b-tag category

Additionally, we perform a closure test using QCD events simulated with Pythia8. The samples used for this study are listed in Table 4, along with the number of events in each and the corresponding cross sections used for normalization. The samples are stitched together using the individual cross sections, normalized to the full luminosity.

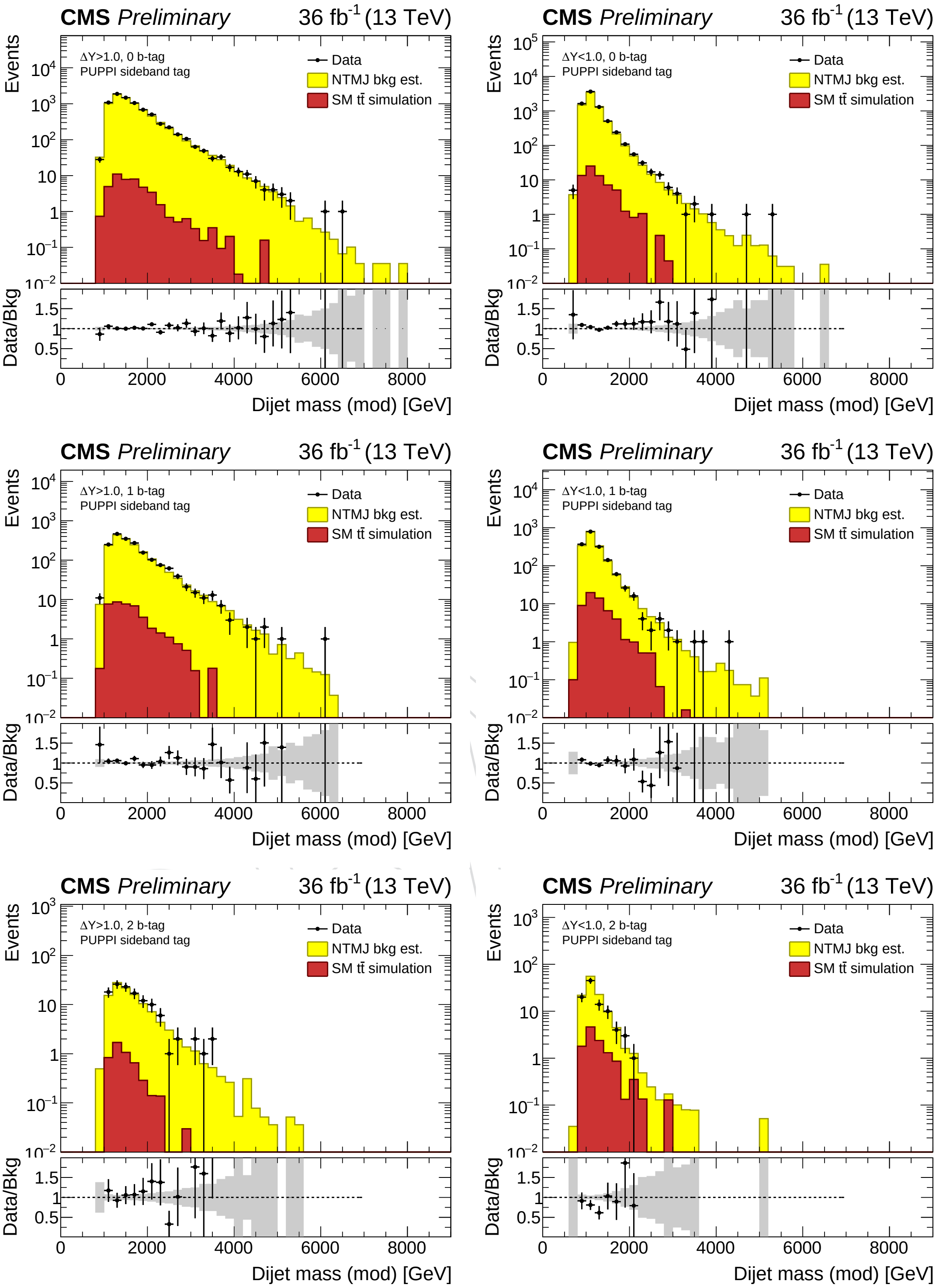

Figure 20: Closure test for the 0+1+2 b-tag categories in the two delta rapidity regions using the data sideband tag definition. The gray band in the ratio plot shows statistical uncertainty only.

To perform the closure tests using these samples, we compare the normalization and shape agreement between the "selected" QCD events, which pass the nominal event selection of two top-tagged jets, and the "predicted" QCD events which are obtained by applying the mistag rate to the same sample, again according to the procedure above. The closure test results are presented in Figure 21 (inclusive in ΔY and number of subjet b-tags) and Figure 22 (separated by signal region). The inclusive plot shows relatively good closure, while the signal regions with greater numbers of subjet b-tags are limited by reduced statistics. Therefore, a corresponding systematic uncertainty is introduced, accounting for the difference between the selected and predicted QCD events.

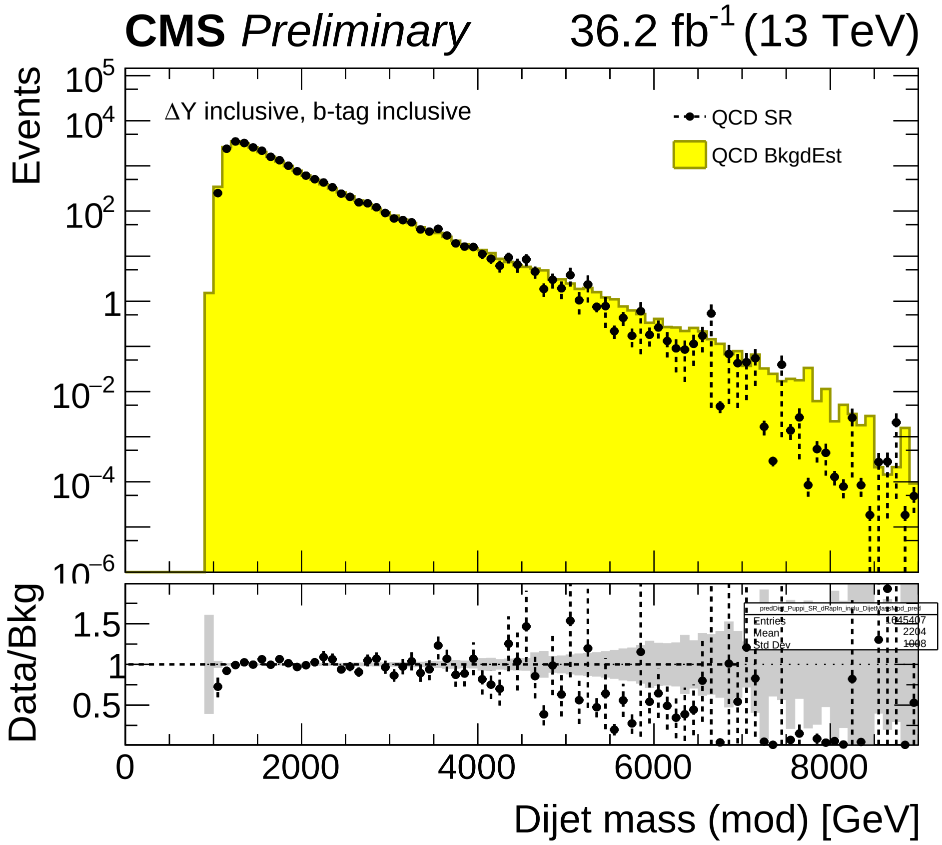

Figure 21: QCD closure test (inclusive ΔY and inclusive b-tag). The gray band in the ratio plot shows statistical uncertainty only.

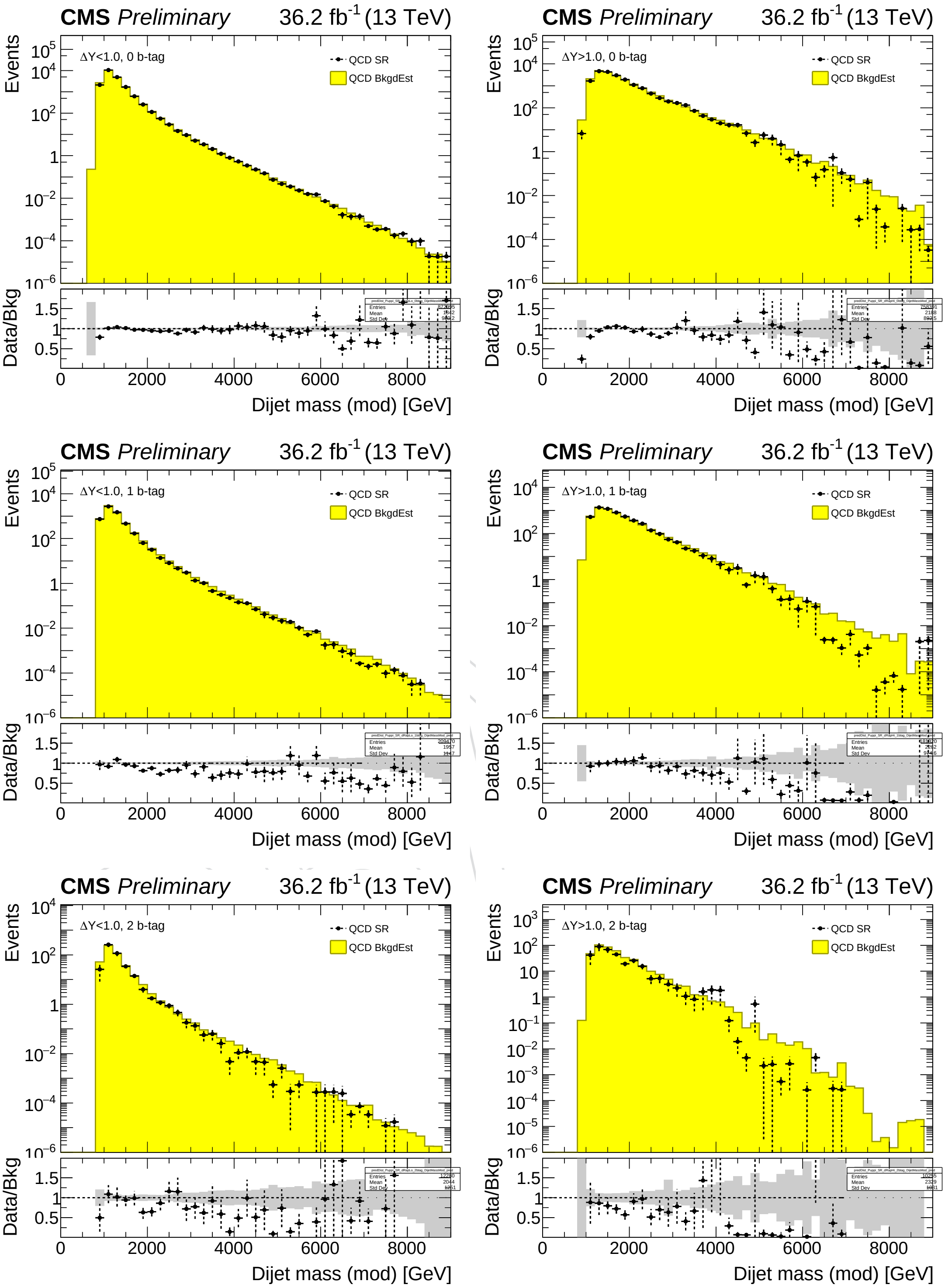

Figure 22: QCD closure test for the 0+1+2 b-tag categories in the two delta rapidity regions. The gray band in the ratio plot shows statistical uncertainty only.

7 Event Kinematics

In this section we examine some event kinematics after the selection has been performed. Figure 23 shows comparisons of data and the data driven background estimate. Comparisons of data to QCD Monte Carlo can be found in appendix A. In the analysis results, we estimate the NTMJ background using a data-driven technique, as described in a previous section. The $t\bar{t}$ Monte Carlo is scaled based on the top and b tagging scale factors when appropriate. An additional scale factor is applied to take into account the measured difference between the high p_T $t\bar{t}$ cross section in data and simulation. This scale factor (0.9) is taken from the normalized parton-level differential cross section measurement made by CMS (TOP-14-002) in the 600 GeV p_T bin. This is consistent with NNLO corrections to the NLO differential cross section in this region [43].

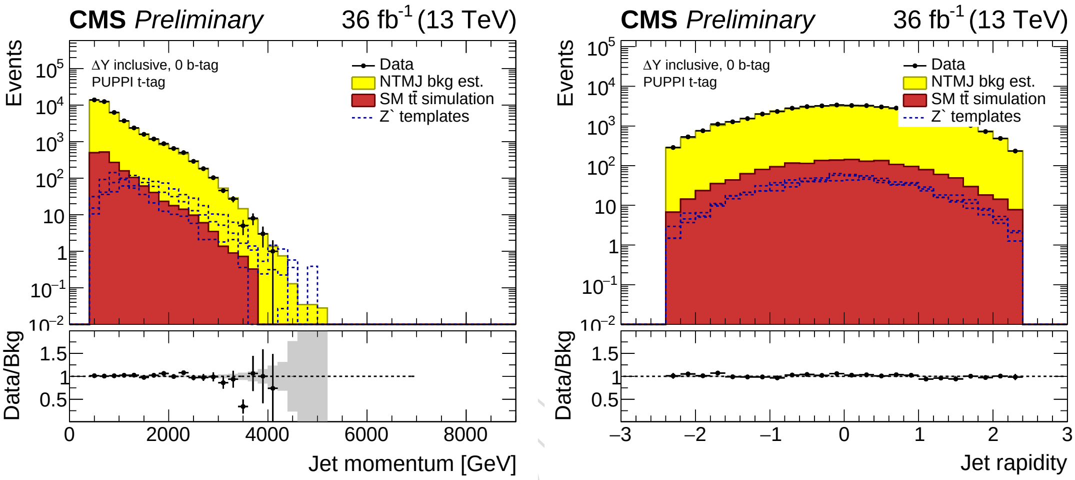

Figure 23: Kinematic comparisons showing $t\bar{t}$ MC and data-driven NTMJ compared to data for the 0 b-tag category (left) jet momentum (right) jet rapidity.

Table 11 shows the expected numbers of events for each of the background processes , along with the observed data counts,for each of the six signal categories used in the analysis. The NTMJ background entry represents the data-driven estimate.

		$\lvert\Delta y\rvert < 1.0$	
Process	**0 b-tags**	**1 b-tag**	**2 b-tags**
NTMJ	21269 ± 797	6536 ± 891	481 ± 71
SM $\mathrm{t\bar{t}}$	1261 ± 169	3347 ± 442	2165 ± 309
Total Background	22530 ± 815	9883 ± 994	2646 ± 317
Observed DATA	22313	9368	2226

		$\lvert\Delta y\rvert > 1.0$	
Process	**0 b-tags**	**1 b-tag**	**2 b-tags**
NTMJ	20576 ± 753	6247 ± 96	469 ± 165
SM $\mathrm{t\bar{t}}$	812 ± 87	1980 ± 208	1205 ± 133
Total Background	21388 ± 758	8227 ± 229	1674 ± 212
Observed DATA	21836	7973	1376

Table 11: Expected background and observed data yields for the six event categorizations used in the final analysis selection. Errors include both the statistical and systematic components.

8 Systematic Uncertainties

Several sources of systematic uncertainty affect both the normalization of event yields in the analysis, as well as the shapes of the $\mathrm{t\bar{t}}$ invariant mass distribution for various processes. We evaluate these systematic uncertainties on both the simulated samples and the data-driven method used to estimate the NTMJ background contribution. This section will detail the individual contributions to the total systematic uncertainty of the analysis. Table 12 shows a list of the systematic uncertainties. Detailed tables of the effects of individual uncertainty contributions on each signal and background process can be seen in the Appendix.

Systematic Uncertainty	Value	Type
b-Tag SF Uncertainty	$\pm 1\sigma$	Rate + Shape
Light jet b-mistag SF Uncertainty	$\pm 1\sigma$	Rate + Shape
CMS Top Tagger SF Uncertainty	+25% -9%	Rate
Jet Energy Corrections	$\pm 1\sigma$	Rate + Shape
Jet Energy Resolution	$\pm 1\sigma$	Rate + Shape
Luminosity	2.5%	Rate
PDF Uncertainty	$\pm 1\sigma$	Rate + Shape
Pileup Uncertainty	$\pm 1\sigma$	Rate + Shape
Top p_{T} Reweighting Uncertainty	$\pm 1\sigma$	Rate + Shape
$\mathrm{t\bar{t}}$ Q^2 Uncertainty	$\pm 1\sigma$	Rate + Shape
$\mathrm{t\bar{t}}$ Cross Section	8%	Rate
Mistag Rate Uncertainty	$\pm 1\sigma$	Rate + Shape
QCD Modified Mass Procedure	$\pm 1\sigma$	Rate + Shape
QCD Closure Test	$\pm 1\sigma$	Rate + Shape

Table 12: Summary of systematic uncertainties applied to the analysis.

8.1 Top Tagging and Subjet b-tagging Scale Factor Uncertainties

All jets in the signal selection are top tagged and therefore the top tagging scale factor, recommended by the CMS JetMET Algorithms and Reconstruction group [39], is applied as an overall normalization scale factor to the final selection (the scale factor is applied twice, once per jet). The associated systematic uncertainty, based on the scale factor uncertainty, is found to be +25% -9% for each event.

The subjet b-tagging scale factor is applied on a subjet-by-subjet basis (see Section 5.8). The subjet b-tagging systematic uncertainty is obtained by applying a $\pm 1\sigma$ variation of the SF value. The full suite of shape templates used for the b-tag scale factor uncertainty can be found in Section C.3. The subjet b-tagging systematic is applied based on the jet flavor. Charm and b-jet SF uncertainties are considered fully correlated, while the light jet b-tag SF uncertainties are treated as a separate systematic uncertainty.

8.2 Jet Energy Scale

We evaluate the effect of the jet energy scale uncertainty on the simulated samples. This is done by varying the jet four-momentum up and down by the jet energy scale uncertainty [44], which is less than 3% in most cases. We include p_T and η dependent corrections to the jet energies, combined with uncertainties due to the difference in the W mass for data and Monte Carlo, along with uncertainties on the response of the pruning algorithm for jets in data and simulation. This combination of uncertainties is described in [45]. This results in a shape difference in the $m_{\mathrm{t\bar{t}}}$ spectrum, which depends on the invariant mass itself. For low masses, the effect is large since the jets are close to the p_T cut of 400 GeV/c. Varying the four-momenta causes jets to fall below the cut, or be promoted above the cut – increasing or decreasing acceptance. For higher invariant masses, the jets generally have higher p_T and this effect is smaller. This systematic uncertainty is applied to both the signal samples and the SM $\mathrm{t\bar{t}}$ sample.

The full suite of shape templates used for the jet energy scale uncertainty can be found in Section C.1.

8.3 Jet Energy Resolution

We account for differing jet energy resolutions between simulated events and data events. We apply the recommended eta-dependent smearing to jets, as listed in Table 13, and then use the errors on this recommendation to form systematic shape uncertainty templates. This systematic uncertainty is applied to all simulated samples, and the systematic shapes can be seen in Section C.2. Additionally, we assume that the jet energy resolution for subjets is the same as that for the hard jets. The variation of the subjet p_T is also included in these shape uncertainties.

$\lvert\eta\rvert$ Range	Smearing Factor
$0.0 < \eta < 0.5$	1.109 ± 0.008
$0.5 < \eta < 0.8$	1.138 ± 0.013
$0.8 < \eta < 1.1$	1.114 ± 0.013
$1.1 < \eta < 1.3$	1.123 ± 0.024
$1.3 < \eta < 1.7$	1.084 ± 0.011
$1.7 < \eta < 1.9$	1.082 ± 0.035
$1.9 < \eta < 2.1$	1.140 ± 0.047
$2.1 < \eta < 2.3$	1.067 ± 0.053
$2.3 < \eta < 2.5$	1.177 ± 0.041
$2.5 < \eta < 2.8$	1.364 ± 0.039
$2.8 < \eta < 3.0$	1.857 ± 0.071
$3.0 < \eta < 3.2$	1.328 ± 0.022
$3.2 < \eta < 5.0$	1.16 ± 0.029

Table 13: Systematic smearing factors applied to individual jets to obtain shape templates used for the jet energy resolution systematic.

8.4 Parton Distribution Function Uncertainties

We evaluate the effect of the parton distribution function (PDF) uncertainty on the simulated samples. We find the RMS of the NNPDF3.0 PDF weights and use this to weight events up and down. This results in a shape difference in the $m_{\mathrm{t\bar{t}}}$ spectrum. This systematic uncertainty is applied to both the signal samples and the SM $\mathrm{t\bar{t}}$ sample. The full suite of shape templates used for the PDF uncertainty can be found in Section C.4.

8.5 Pileup Uncertainties

We evaluate the effect of the pileup uncertainty on the simulated samples. We reweight the Monte Carlo simulation with the data pileup distribution, based on a minimum bias cross section of 69 mb. We use the uncertainty on this cross section, 5%, to vary the pileup distribution up and down. This results in a shape difference in the $m_{\mathrm{t\bar{t}}}$ spectrum. This systematic uncertainty is applied to both the signal samples and the SM $\mathrm{t\bar{t}}$ sample. The full suite of shape templates used for the PDF uncertainty can be found in Section C.5.

8.6 Top p_{T} Reweighting Uncertainties

We evaluate the effect of the top p_{T} reweighting uncertainty on the simulated samples. This systematic uncertainty is computed by taking the difference between the $m_{\mathrm{t\bar{t}}}$ distributions with and without top p_{T} reweighting applied. This results in a shape difference in the $m_{\mathrm{t\bar{t}}}$ spectrum. Figure 39 shows the distributions with and without top p_{T} reweighting.

8.7 SM $\mathrm{t\bar{t}}$ Uncertainties

The uncertainties applied exclusively to SM $\mathrm{t\bar{t}}$ events include two contributions: a rate-only component due to the uncertainty in the $\mathrm{t\bar{t}}$ cross section, which is taken to be 8% [46], and a second shape component for uncertainties in the factorization and normalization scale (Q^2) uncertainties. The Q^2 uncertainties are evaluated by finding the envelope of the Q^2 weights (variations of μ_R and μ_F by factors of 2 or 0.5), which is then used to weight events up and down. This results in a shape difference in the $m_{\mathrm{t\bar{t}}}$ spectrum. Section C.6 shows the shape templates corresponding to the ± 1 standard deviation uncertainties on the Q^2 scale.

8.8 Multijet Background Uncertainties

The mistag rate uncertainty, shown in Figure 16, contains statistical uncertainties which are propagated to the NTMJ background estimation. The systematic uncertainty associated with the 'mass-modified' procedure, which is used to correct kinematic bias in the background estimation, is computed by taking half the difference between the uncorrected background estimate and and the 'mass-modified' background estimate. Section C.7 shows the shape templates corresponding to the ±1 standard deviation uncertainties from the 'mass-modified' procedure.

The mistag rate uncertainty, shown in Figure 16, contains statistical uncertainties which are propagated to the NTMJ background estimation. The systematic uncertainty associated with the 'mass-modified' procedure, which is used to correct kinematic bias in the background estimation, is computed by taking half the difference between the uncorrected background estimate and and the 'mass-modified' background estimate. Additionally, the systematic uncertainty associated with the closure test is computed by calculating the percent difference between the double-tagged QCD Monte Carlo and the 'mass-modified' background estimate applied to QCD Monte Carlo - the curves shown in 22. The systematic used to weight events up and down is calculated by multiplying this percent difference by the NTMJ used for the background estimate. Sections C.7 and C.8 show the shape templates corresponding to the ±1 standard deviation uncertainties from the 'mass-modified' procedure and the closure test, respectively.

9 Statistical Interpretation and Results

We do not observe any excess of events above the expected background from SM $\mathrm{t\bar{t}}$ and non-top multijet background. We therefore proceed to set limits on the production cross sections of the three hypothesized signal models. We perform a template-based shape analysis, using the distributions of the candidate top pair invariant mass. The final distributions are shown in Figure 24. Both statistical and systematic uncertainties are shown, with the dominant systematic uncertainty being the top-tag scale factor uncertainty. Additionally, the effect of the closure test uncertainty can be seen in the turn-on and tails of the distributions (c.f. the distributions in the last version of the note).

We use a Bayesian likelihood-based method, allowing the expected background model to fluctuate within the various systematic and statistical uncertainties to find the best fit to the observed data distribution. The distributions input to the limit setting program (in Section D) have a variable binning, which is chosen to best accommodate the background uncertainties.

We use the Theta software package [47] to produce 95% confidence level (CL) upper limits on the cross sections for the four signal models, as a function of the new heavy particle mass. A Poisson model is used for each bin in the $m_{\mathrm{t\bar{t}}}$ distribution, with the final likelihood composed of the product of these Poisson probabilities for each bin in the $m_{\mathrm{t\bar{t}}}$ distribution. For a single bin, the mean of this distribution is shown in Equation 2.

$$\mu_i = \sum_k \beta_k \cdot T_{k,i} \tag{2}$$

The index k represents each physics process contributing to the bin i. T represents the number of expected events for the process k in bin i. The factor β is the Poisson mean for the individual process k. In other words, β_k is the weight given to each physics process due to the choice of all of the nuisance parameters. With this per-bin formula, the full likelihood can be formed as follows:

$$\mathcal{L}(\beta_k) = \Pi_i \frac{\mu_i \cdot e^{-\mu_i}}{N_i^{\mathrm{data}}!}. \tag{3}$$

For the Poisson parameters, β_k, we use different choices of prior distributions. For the NTMJ estimate and the signal cross section normalization parameters, we use a flat prior distribution. For the other nuisance parameters, a lognormal prior distribution is used. Using these parameters, pseudoexperiments are performed to estimate the 68% and 95% CL (1- and 2-sigma) expected limit bands. In the pseudoexperiments, the systematic and statistical uncertainties are accounted for through nuisance parameters. These nuisance parameters are randomly varied within their uncertainties, and the posterior is re-fitted for each individual pseudoexperiment. Through this method, we can evaluate the effect of the shape and normalization uncertainties on the sensitivity of the analysis. Figure 25 shows the the deviation of the post-fit nuisance parameters from their prior values for the narrow 3 TeV Z′ signal.

Figure 26 shows the expected and observed cross section limits obtained from the analysis, using the combination of the 6 independent signal regions A-F. The dashed line represents the median expected limit, while the green and yellow bands represent the one and two sigma bands, respectively, of the expected limits from the set of pseudoexperiments. The black solid line shows the observed limit results using the observed data distribution. The red solid line shows the theoretical cross sections curves - 1.3 × leading order (LO) from PYTHIA 8 for RS KK gluon and next-to-leading order (NLO) for the Z′ curves [48]. The cross sections are also shown numerically in Tables 15 – 18. Looking only at the expected limits, it is clear that this analysis is more sensitive than the ATLAS or CMS analyses using 2015 data. The improvement is slightly

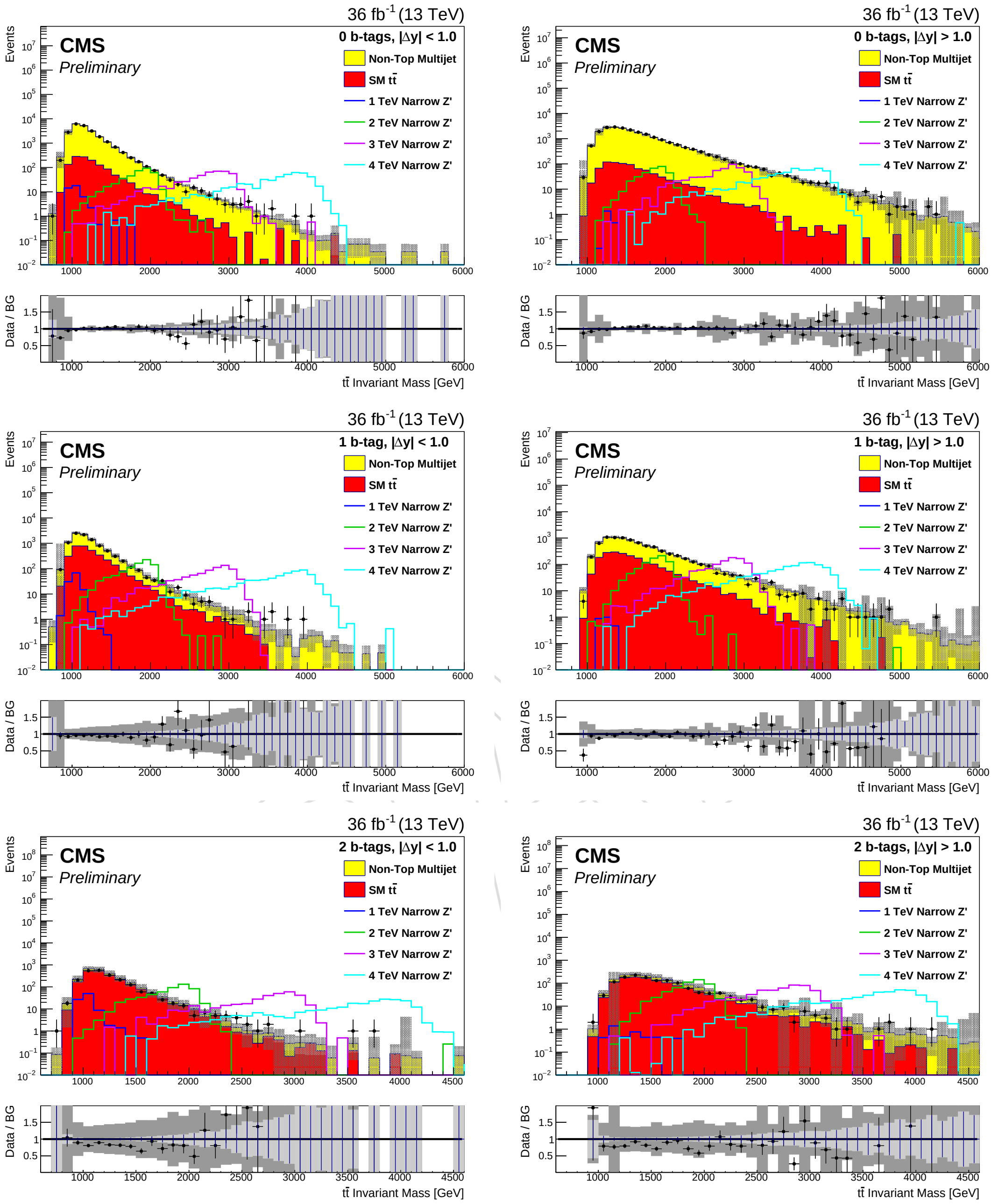

Figure 24: Final log-scale distributions of $m_{t\bar{t}}$ for all six signal regions, with the $|\Delta y| < 1.0$ categories shown in the left column and the $|\Delta y| > 1.0$ categories in the right. The number of b-tags in the plots increase from zero in the first row to two b-tags in the third row. The shaded region corresponds to the combined systematic (dark gray) and statistical (light gray) uncertainties on the background model. Signal models have been normalized to a cross section of 1 pb.

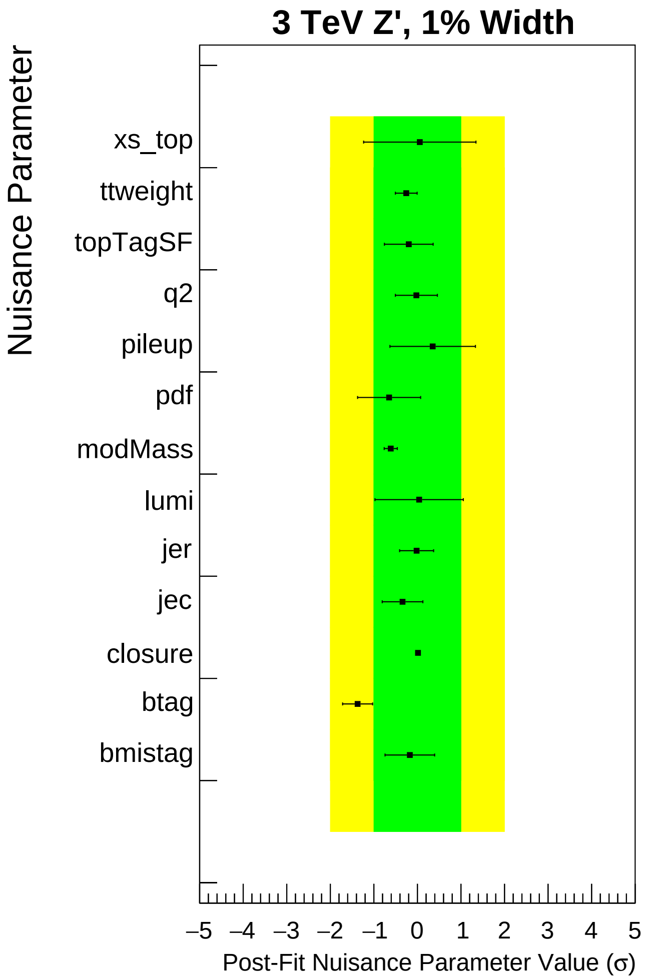

Figure 25: Deviation of post-fit nuisance parameter values from their prior values for the narrow 3 TeV Z′ signal.

more than the expected scaling with luminosity, as the background estimate uncertainty also improves with increased luminosity.

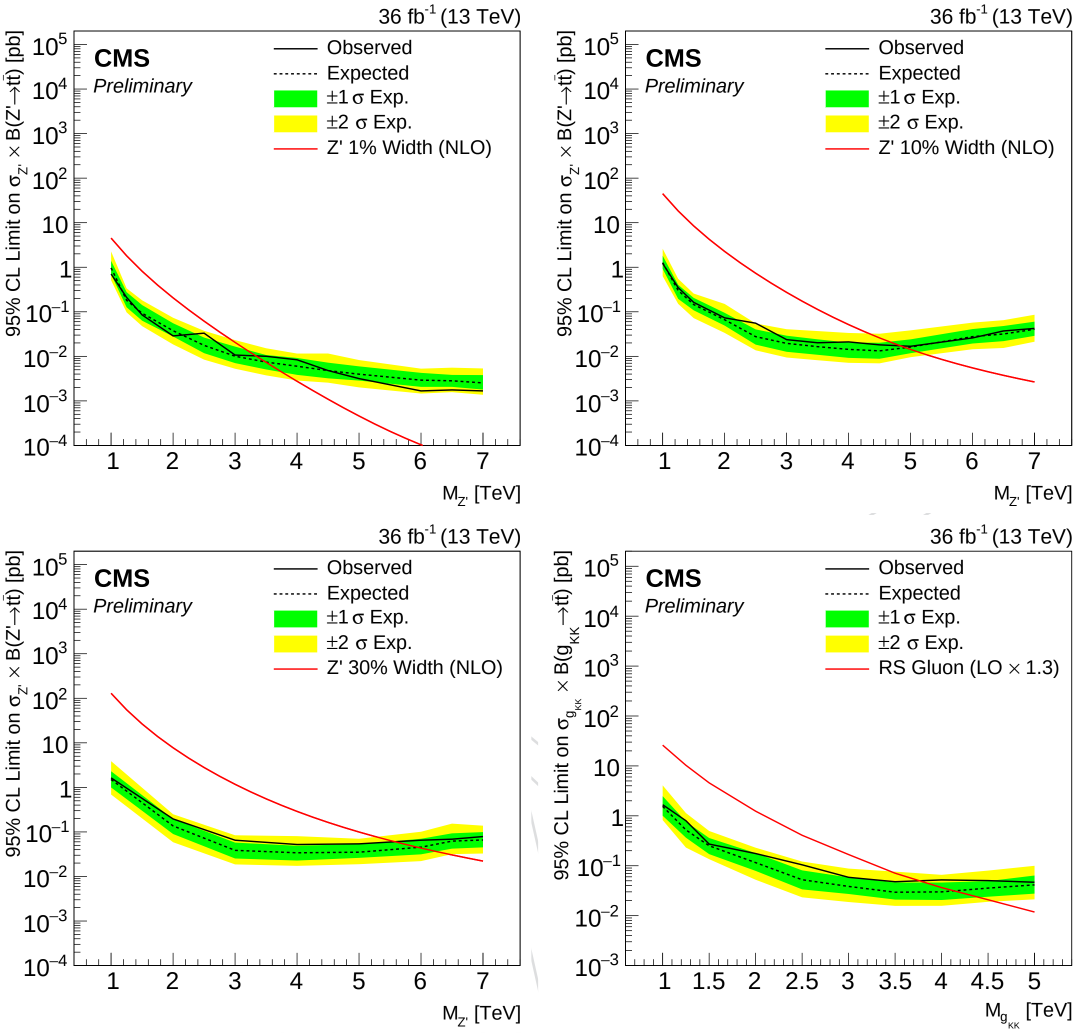

Figure 26: Expected and observed 95% CL upper limits on the cross section times branching ratio for the four signal models, as a function of the new heavy particle mass. The four models considered are a Z′ boson whose width is 1% of its mass (upper left), a 10% width Z′ boson (upper right), a 30% width Z′ boson (lower left), and an RS KK gluon (lower right). The black, solid (dashed) line gives the observed (median expected) limits, while the one (two) sigma expected limit band is shown in green (yellow).

A 2 σ upward fluctuation at 2.5 TeV can be seen for the narrow Z′ hypothesis. This is due to upward fluctuations in the most sensitive channels - 1 and 2 b-tags in the $|\Delta y| < 1.0$ region. This includes an upward fluctuation slightly greater than 2 σ in the latter category. Figure 27 shows the expected and observed limits for the six signal regions of the 1% width Z′ boson. Figure 28 shows the relative contributions of these six channels to the sensitivity of the limits.

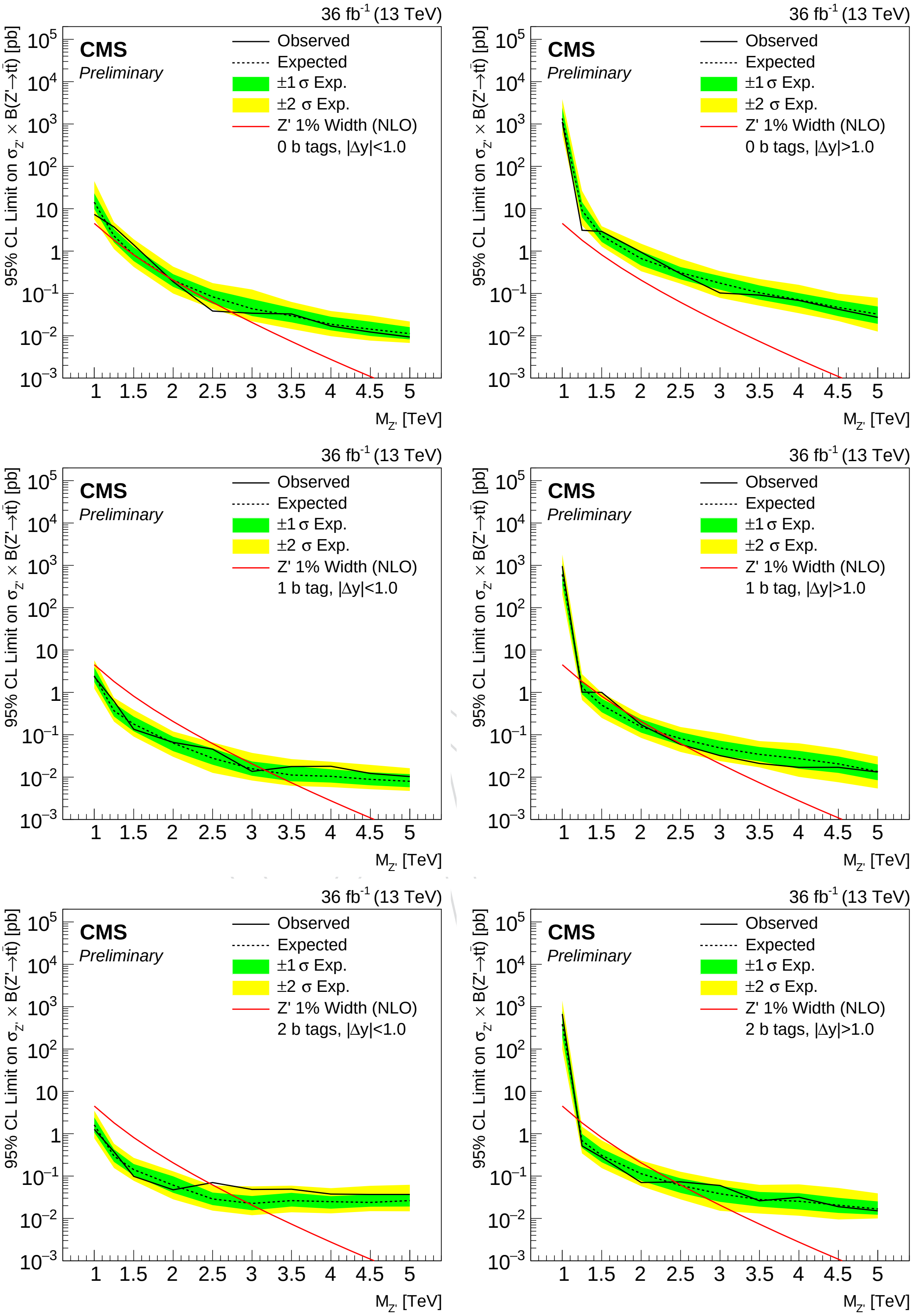

Figure 27: Expected and observed 95% CL upper limits on the cross section times branching ratio for the six signal regions (1% width Z' boson), as a function of the new heavy particle mass. The plots on the left (right) represent the low (high) $|\Delta y|$ region, while the number of subjet b tags increases from the top to bottom rows. The black, solid (dashed) line gives the observed (median expected) limits, while the one (two) sigma expected limit band is shown in green (yellow).

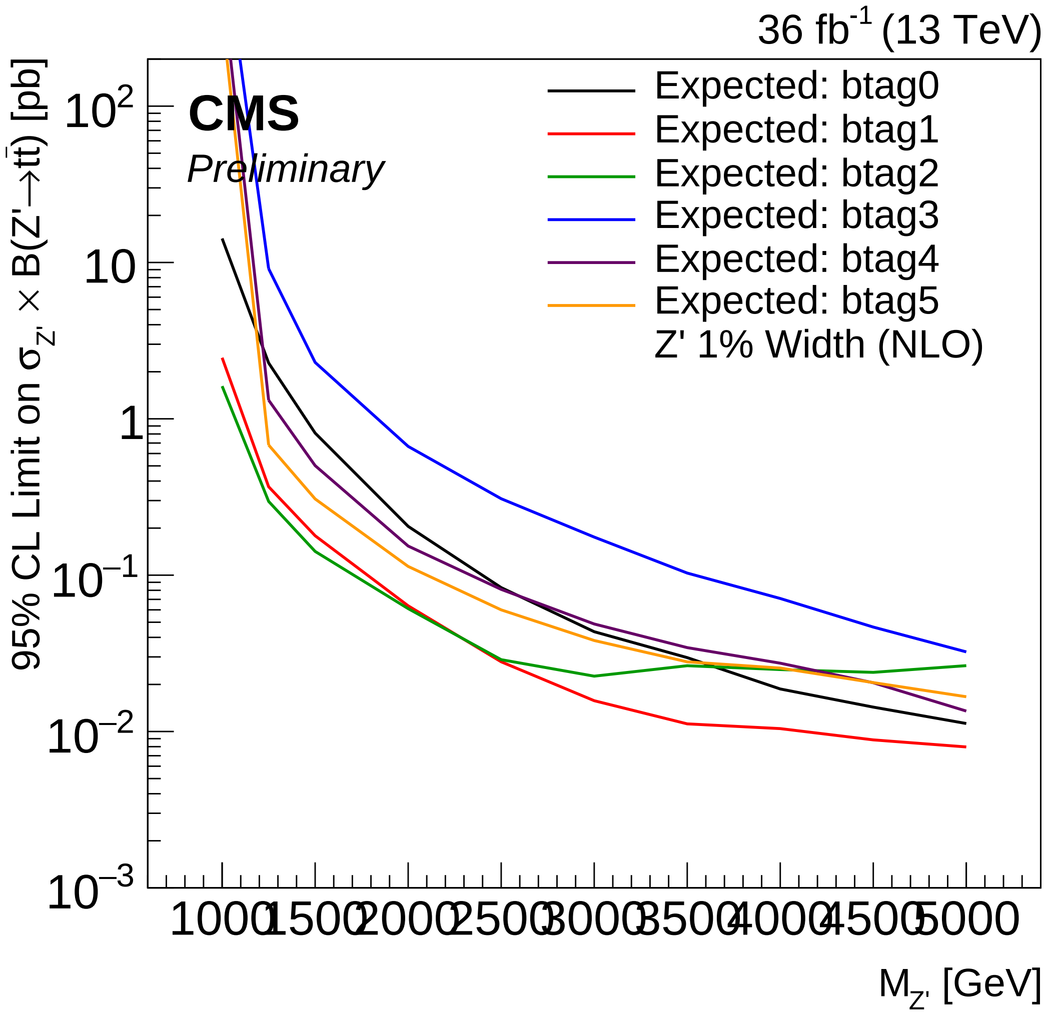

Figure 28: Expected limits for the full analysis, comparing the 6 signal region categories for a 1% width Z′ boson. Following the order in the legend, the first (last) three curves correspond to the low (high) $|\Delta y|$ regions, with number of subjet b-tags increasing from top to bottom.

Mass Exclusion Limits

Signal Model	Exclusion Ranges (TeV)	
	Expected	Observed
Z′ (1% Width)	1.0 – 3.5	1.0 – 3.3
Z′ (10% Width)	1.0 – 4.9	1.0 – 4.8
Z′ (30% Width)	1.0 – 6.0	1.0 – 5.6
RS Gluon	1.0 – 4.1	1.0 – 3.8

Table 14: Observed and expected exclusion ranges for resonance masses in each of the signal models tested in the analysis.

Z′ (1% Width) Signal Hypothesis

Mass (GeV)	Observed 95% CL Limit (pb)	Expected 95% CL Limits (pb)				
		-2σ	-1σ	Median	$+1\sigma$	$+2\sigma$
1	**0.7**	0.51	0.69	**0.97**	1.4	2.3
1.25	**0.21**	0.097	0.13	**0.18**	0.28	0.34
1.5	**0.085**	0.048	0.063	**0.093**	0.14	0.18
2	**0.029**	0.019	0.028	**0.038**	0.055	0.074
2.5	**0.033**	0.0084	0.012	**0.018**	0.026	0.037
3	**0.011**	0.0053	0.0071	**0.01**	0.017	0.023
3.5	**0.01**	0.0037	0.0051	**0.0074**	0.011	0.015
4	**0.0084**	0.0029	0.0038	**0.006**	0.0092	0.012
4.5	**0.0048**	0.0026	0.0032	**0.0048**	0.0072	0.012
5	**0.0032**	0.002	0.0029	**0.004**	0.006	0.0083
6	**0.0017**	0.0015	0.0021	**0.0029**	0.0043	0.0053
6.5	**0.0018**	0.0016	0.0021	**0.0028**	0.0038	0.0056
7	**0.0017**	0.0014	0.0018	**0.0025**	0.0038	0.0054

Table 15: Table of expected and observed 95% CL cross section limits, for the narrow (1% width) Z′ signal hypothesis.

Z′ (10% Width) Signal Hypothesis

Mass (GeV)	Observed 95% CL Limit (pb)	Expected 95% CL Limits (pb)				
		-2σ	-1σ	Median	$+1\sigma$	$+2\sigma$
1	**1.2**	0.63	0.92	**1.3**	1.8	2.6
1.25	**0.35**	0.15	0.2	**0.3**	0.4	0.55
1.5	**0.16**	0.072	0.11	**0.15**	0.21	0.26
2	**0.073**	0.034	0.049	**0.066**	0.095	0.15
2.5	**0.056**	0.014	0.018	**0.028**	0.04	0.055
3	**0.024**	0.0094	0.013	**0.02**	0.029	0.041
3.5	**0.02**	0.0082	0.011	**0.016**	0.024	0.037
4	**0.021**	0.0072	0.0092	**0.014**	0.02	0.033
4.5	**0.018**	0.007	0.0088	**0.013**	0.02	0.032
5	**0.017**	0.0096	0.012	**0.016**	0.024	0.038
6	**0.026**	0.014	0.019	**0.028**	0.041	0.057
6.5	**0.037**	0.015	0.022	**0.032**	0.048	0.065
7	**0.042**	0.021	0.029	**0.04**	0.06	0.086

Table 16: Table of expected and observed 95% CL cross section limits, for the wide (10% width) Z′ signal hypothesis.

Z′ (30% Width) Signal Hypothesis

Mass (GeV)	Observed 95% CL Limit (pb)	Expected 95% CL Limits (pb)				
		-2σ	-1σ	Median	$+1\sigma$	$+2\sigma$
1	**1.6**	0.69	1	**1.5**	2.3	3.9
2	**0.2**	0.059	0.09	**0.14**	0.2	0.25
3	**0.065**	0.019	0.025	**0.039**	0.058	0.084
4	**0.052**	0.017	0.023	**0.034**	0.049	0.08
5	**0.054**	0.019	0.026	**0.035**	0.053	0.07
6	**0.065**	0.022	0.031	**0.045**	0.07	0.1
6.5	**0.069**	0.032	0.042	**0.062**	0.093	0.15
7	**0.079**	0.033	0.045	**0.066**	0.099	0.14

Table 17: Table of expected and observed 95% CL cross section limits, for the extra wide (30% width) Z′ signal hypothesis.

RS Gluon Signal Hypothesis

Mass (GeV)	Observed 95% CL Limit (pb)	Expected 95% CL Limits (pb)				
		-2σ	-1σ	Median	$+1\sigma$	$+2\sigma$
1	**1.7**	0.82	1	**1.5**	2.5	4.1
1.25	**0.8**	0.23	0.36	**0.52**	0.77	1.1
1.5	**0.27**	0.14	0.17	**0.25**	0.36	0.5
2	**0.18**	0.052	0.079	**0.12**	0.18	0.23
2.5	**0.1**	0.023	0.034	**0.052**	0.081	0.12
3	**0.059**	0.019	0.027	**0.039**	0.058	0.088
3.5	**0.048**	0.016	0.021	**0.029**	0.046	0.076
4	**0.052**	0.016	0.021	**0.03**	0.046	0.066
4.5	**0.05**	0.019	0.024	**0.036**	0.049	0.08
5	**0.047**	0.021	0.028	**0.041**	0.064	0.1

Table 18: Table of expected and observed 95% CL cross section limits, for the RS Gluon signal hypothesis.

10 Conclusions

We have performed a search for top pair resonances in the all-hadronic channel using $\sqrt{s} = 13$ TeV data from the LHC Run 2 taken in 2016. The search uses well understood top-tagging algorithm, optimized for Run 2 analyses, using the soft-drop mass and N-subjettiness jet substructure variables. For the first time jet t-tagging variables are calulcated using PUPPI inputs. We estimate the non-top multijet background using a data-driven top-mistag rate measurement. No excess above standard model expectation is observed, and we proceed to set limits on the Z′ production cross section, for signal models with varying Z′ widths. We exclude Z′ masses up to 5.6 TeV (30 % width). The exclusion results are an improvement upon those from the 2015 ATLAS and CMS searches, largely due to the significant increase in luminosity.

References

[1] S. Dimopoulos and H. Georgi, “Softly Broken Supersymmetry and SU(5)”, *Nucl. Phys.* **B193** (1981) 150, `doi:10.1016/0550-3213(81)90522-8`.

[2] S. Weinberg, “Implications of Dynamical Symmetry Breaking”, *Phys. Rev.* **D13** (1976) 974–996, `doi:10.1103/PhysRevD.13.974`.

[3] L. Susskind, “Dynamics of Spontaneous Symmetry Breaking in the Weinberg- Salam Theory”, *Phys. Rev.* **D20** (1979) 2619–2625, `doi:10.1103/PhysRevD.20.2619`.

[4] C. T. Hill and S. J. Parke, “Top production: Sensitivity to new physics”, *Phys. Rev.* **D49** (1994) 4454–4462, `doi:10.1103/PhysRevD.49.4454`, `arXiv:hep-ph/9312324`.

[5] R. S. Chivukula, B. A. Dobrescu, H. Georgi, and C. T. Hill, “Top quark seesaw theory of electroweak symmetry breaking”, *Phys. Rev.* **D59** (1999) 075003, `doi:10.1103/PhysRevD.59.075003`, `arXiv:hep-ph/9809470`.

[6] N. Arkani-Hamed, A. G. Cohen, and H. Georgi, “Electroweak symmetry breaking from dimensional deconstruction”, *Phys. Lett.* **B513** (2001) 232–240, `doi:10.1016/S0370-2693(01)00741-9`, `arXiv:hep-ph/0105239`.

[7] N. Arkani-Hamed, S. Dimopoulos, and G. R. Dvali, “The hierarchy problem and new dimensions at a millimeter”, *Phys. Lett.* **B429** (1998) 263–272, `doi:10.1016/S0370-2693(98)00466-3`, `arXiv:hep-ph/9803315`.

[8] L. Randall and R. Sundrum, “A large mass hierarchy from a small extra dimension”, *Phys. Rev. Lett.* **83** (1999) 3370–3373, `doi:10.1103/PhysRevLett.83.3370`, `arXiv:hep-ph/9905221`.

[9] L. Randall and R. Sundrum, “An alternative to compactification”, *Phys. Rev. Lett.* **83** (1999) 4690–4693, `doi:10.1103/PhysRevLett.83.4690`, `arXiv:hep-th/9906064`.

[10] J. Rosner, “Prominent decay modes of a leptophobic z′”, *Phys. Rev. B* **387** (1996) 113–117, `arXiv:9607207v3`.

[11] CDF Collaboration, “Cross section for topcolor z′ decaying to top-antitop”, Technical Report FERMILAB-FN-0687, Fermilab, 1999. `arXiv:9911288`.

[12] K. Lynch, M. Narain, E. Simmons, and S. Mrenna, “Finding z′ bosons coupled preferentially to the third family at cern lep and the fermilab tevatron”, *Phys. Rev. D* **63** (2001) 035006, `arXiv:0007286`.

[13] K. Agashe et al., “Lhc signals for warped electroweak neutral gauge bosons”, *Phys. Rev. D* **76** (2007) 115015, `arXiv:0810.1497`.

[14] K. Agashe et al., “Lhc signals from warped extra dimensions”, *Phys. Rev. D* **77** (2008) 015003, `arXiv:0612015`.

[15] CDF Collaboration, “Search for resonant production of $t\bar{t}$ pairs in 4.8 fb^{-1} of integrated luminosity of $p\overline{p}$ collisions at $\sqrt{s}\,bf{=}1.96$ TeV”, *Phys. Rev. D* **84** 072004, `doi:10.1103/PhysRevD.84.072004`, `arXiv:1107.5063`.

[16] D0 Collaboration, “Search for $t\bar{t}$ resonances in the lepton+jets final state in $p\overline{p}$ collisions at $\sqrt{s}$ = 1.96 tev”, *Phys. Rev. B* **668** (2008) 98–104, `doi:10.1016/j.physletb.2008.08.027`, `arXiv:0804.3664`.

[17] CMS Collaboration, “Search for anomalous $t\bar{t}$ production in the highly-boosed all-hadronic final state”, *JHEP* **09** (2012) 29, `arXiv:1204.2488`.

[18] CMS Collaboration, “Search for resonant $t\bar{t}$ production in lepton+jets events in pp collisions at $\sqrt{s}$ = 7 tev”, *JHEP* **12** (2012) 15, `arXiv:1209.4397`.

[19] ATLAS Collaboration, “Search for resonances decaying into top-quark pairs using fully hadronic decays in pp collisions with atlas at $\sqrt{s}$ = 7 tev”, *JHEP* **01** (2013) 116, `arXiv:1211.2202`.

[20] ATLAS Collaboration, “A search for $t\bar{t}$ resonances in lepton+jets events with highly-boosed top quarks collected in pp collisions with atlas at $\sqrt{s}$ = 7 tev”, *JHEP* **09** (2012) 41, `arXiv:1207.2409`.

[21] CMS Collaboration Collaboration, “Search for anomalous top quark pair production in the boosted all-hadronic final state using pp collisions at sqrt(s) = 8 tev”, Technical Report CMS-PAS-B2G-12-005, CERN, Geneva, 2013.

[22] CMS Collaboration, “Searches for new physics using the $t\bar{t}$ invariant mass distribution in pp collisions at $\sqrt{s}$ = 8 tev”, *Phys. Rev. Lett.* **111** (2013) 211804, `arXiv:1309.2030`.

[23] CMS Collaboration, “Search for resonant $t\bar{t}$ production in proton-proton collisions at $\sqrt{s}$ = 8 tev”, *Phys. Rev. D* **93** (2016) 012001, `arXiv:1506.03062`.

[24] ATLAS Collaboration, “A search for $t\bar{t}$ resonances using lepton-plus-jets events in proton-proton collisions at $\sqrt{s}$ = 8 tev with the atlas detector”, *JHEP* **08** (2015) 148, `arXiv:1505.07018`.

[25] CMS Collaboration, “Search for $\mathrm{t\bar{t}}$ resonances in highly-boosted lepton+jets and fully hadronic final states in proton-proton collisions at $\sqrt{s} = 13$ TeV”, `arXiv:1704.03366`.

[26] ATLAS Collaboration Collaboration, “Search for heavy particles decaying to pairs of highly-boosted top quarks using lepton-plus-jets events in proton-proton collisions at $\sqrt{s}$ = 13 tev with the atl as detector”, ATLAS Conference Note ATLAS-CONF-2016-014, CERN, 2016.

[27] D. Bertolini, P. Harris, M. Low, and N. Tran, “Pileup Per Particle Identification”, *JHEP* **10** (2014) 059, `doi:10.1007/JHEP10(2014)059`, `arXiv:1407.6013`.

[28] CMS Collaboration Collaboration, “Search for top quark-antiquark resonances in the all-hadronic final state at sqrt(s)=13 TeV”, Technical Report CMS-PAS-B2G-15-003, CERN, Geneva, 2016.

[29] N. Kidonakis, "Differential and total cross sections for top pair and single top production", `arXiv:1205.3453`.

[30] CMS Collaboration, "Utilities for Accessing Pileup Information for Data, https://twiki.cern.ch/twiki/bin/view/CMS/PileupJSONFileforData#Pileup_JSON_Files_For_Run_II",.

[31] CMS Collaboration, "Description and performance of track and primary-vertex reconstruction with the CMS tracker", *JINST* **9** (2014) P10009, `doi:10.1088/1748-0221/9/10/P10009`, `arXiv:1405.6569`.

[32] M. Cacciari, G. P. Salam, and G. Soyez, "The anti-k_t jet clustering algorithm", *JHEP* **04** (2008) 063, `doi:10.1088/1126-6708/2008/04/063`, `arXiv:0802.1189`.

[33] CMS Collaboration, "Particle-flow reconstruction and global event description with the cms detector", *JINST* **12** (2017) P10003, `doi:10.1088/1748-0221/12/10/P10003`, `arXiv:1706.04965`.

[34] CMS Collaboration, "Measurement of differential cross sections for top quark pair production using the lepton+jets final state in proton-proton collisions at 13 TeV", *Phys. Rev.* **D95** (2017), no. 9, 092001, `doi:10.1103/PhysRevD.95.092001`, `arXiv:1610.04191`.

[35] CMS Collaboration Collaboration, "Measurement of the differential cross section for $\mathrm{t\bar{t}}$ production in the dilepton final state at $\sqrt{s} = 13$ TeV", Technical Report CMS-PAS-TOP-16-011, CERN, Geneva, 2016.

[36] CMS Collaboration, "Top tagging with new approaches", CMS Physics Analysis Summary CMS-PAS-JME-15-002, 2016.

[37] A. J. Larkoski, S. Marzani, G. Soyez, and J. Thaler, "Soft Drop", *JHEP* **1405** (2014) 146, `doi:10.1007/JHEP05(2014)146`, `arXiv:1402.2657`.

[38] M. Dasgupta, A. Fregoso, S. Marzani, and G. P. Salam, "Towards an understanding of jet substructure", *JHEP* **09** (2013) 029, `doi:10.1007/JHEP09(2013)029`, `arXiv:1307.0007`.

[39] CMS Collaboration, "Boosted Top Jet Tagging, https://twiki.cern.ch/twiki/bin/view/CMS/JetTopTagging13$_{T}eV_{w}orking_{p}oints_{C}MSSW_{8}{}_{0}^{\prime\prime}$,.

[40] J. Thaler and K. Van Tilburg, "Maximizing Boosted Top Identification by Minimizing N-subjettiness", *JHEP* **1202** (2012) 093, `doi:10.1007/JHEP02(2012)093`, `arXiv:1108.2701`.

[41] CMS Collaboration, "Identification of b-quark jets with the cms experiment",.

[42] CMS Collaboration, "BTAG POG, https://twiki.cern.ch/twiki/bin/viewauth/CMS/BTagSFMethods",.

[43] M. Czakon, P. Fiedler, D. Heymes, and A. Mitov, "NNLO QCD predictions for fully-differential top-quark pair production at the Tevatron", *JHEP* **05** (2016) 034, `doi:10.1007/JHEP05(2016)034`, `arXiv:1601.05375`.

[44] J. Group, "Jet Energy Corrections and Uncertainties. Detector Performance Plots for 2012.",.

[45] CMS Collaboration, “Determination of Jet Energy Calibration and Transverse Momentum Resolution in CMS”, *JINST* **6** (2011) P11002, `doi:10.1088/1748-0221/6/11/P11002`, `arXiv:1107.4277`.

[46] CMS Collaboration, “Measurement of the differential cross section for top quark pair production in pp collisions at sqrt(s) = 8 TeV”, (2015). `arXiv:1505.04480`. Submitted to EPJC.

[47] T. Muller, J. Ott, and J. Wagner-Kuhr, “theta - a framework for template-based modeling and inference”, CMS Internal Note 2010/017, 2010.

[48] R. Bonciani, T. Jezo, M. Klasen, F. Lyonnet, I. Schienbein, “Electroweak top-quark pair production at the LHC with Z′ bosons to the NLO QCD in POWHEG”, *JHEP* **02** (2016) 141, `doi:10.1007/JHEP02(2016)141`, `arXiv:1511.08185`.

A Additional Kinematic Plots

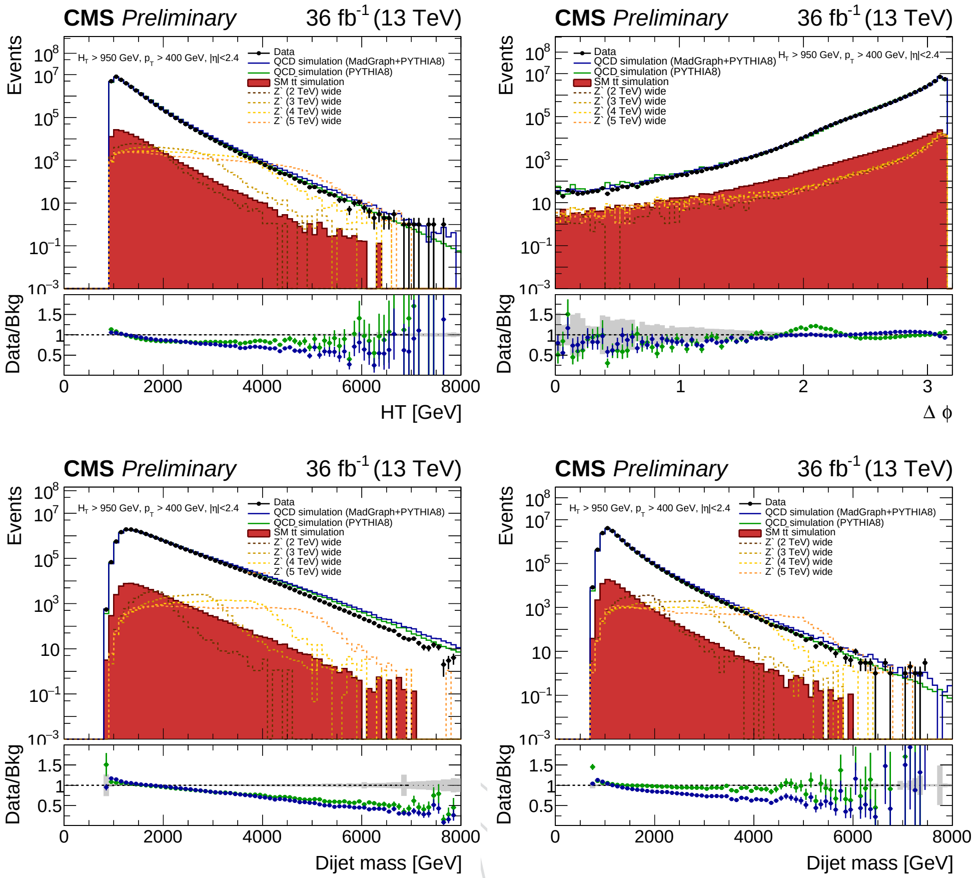

Figure 29: Event kinematic plots after pre-selection (a) HT (b) $\Delta\phi$ (all pre-selection cuts except for the cut on $\Delta\phi$) (c) Dijet mass ($\Delta Y > 1.0$) (d) Dijet mass ($\Delta Y < 1.0$)

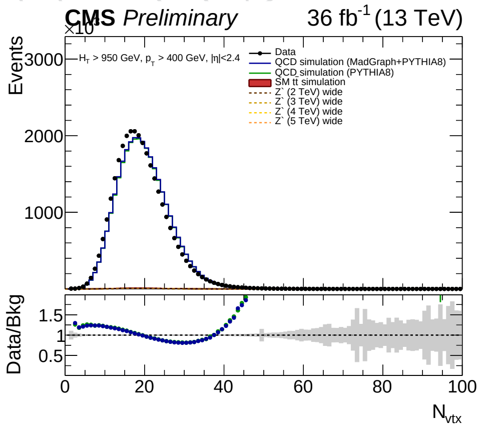

Figure 30: Number of primary vertices

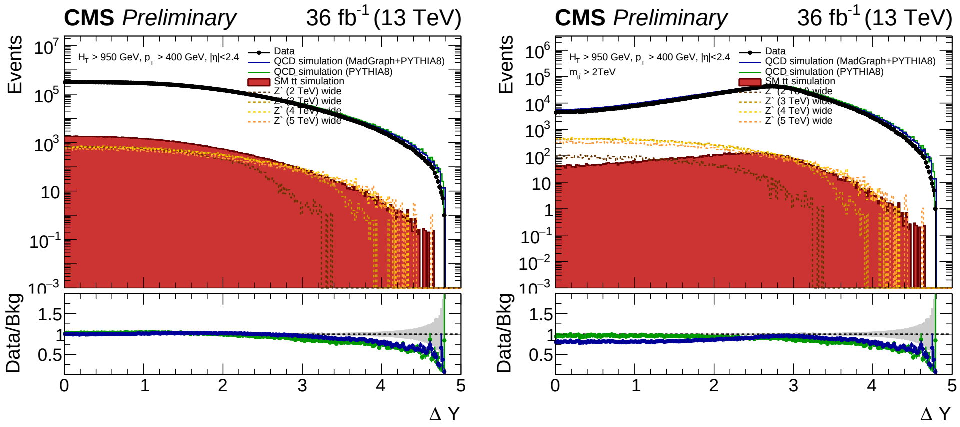

Figure 31: Event kinematic plots after pre-selection (a) ΔY (b) ΔY ($m_{tt} > 2\,\mathrm{TeV}/c^2$)

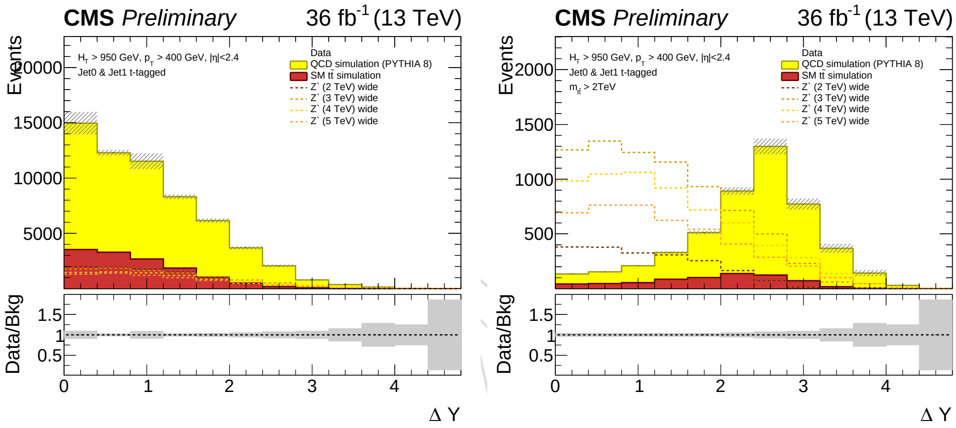

Figure 32: Event kinematic plots after requiring two t-tagged jets (a) ΔY (b) ΔY ($m_{tt} > 2\,\mathrm{TeV}/c^2$)

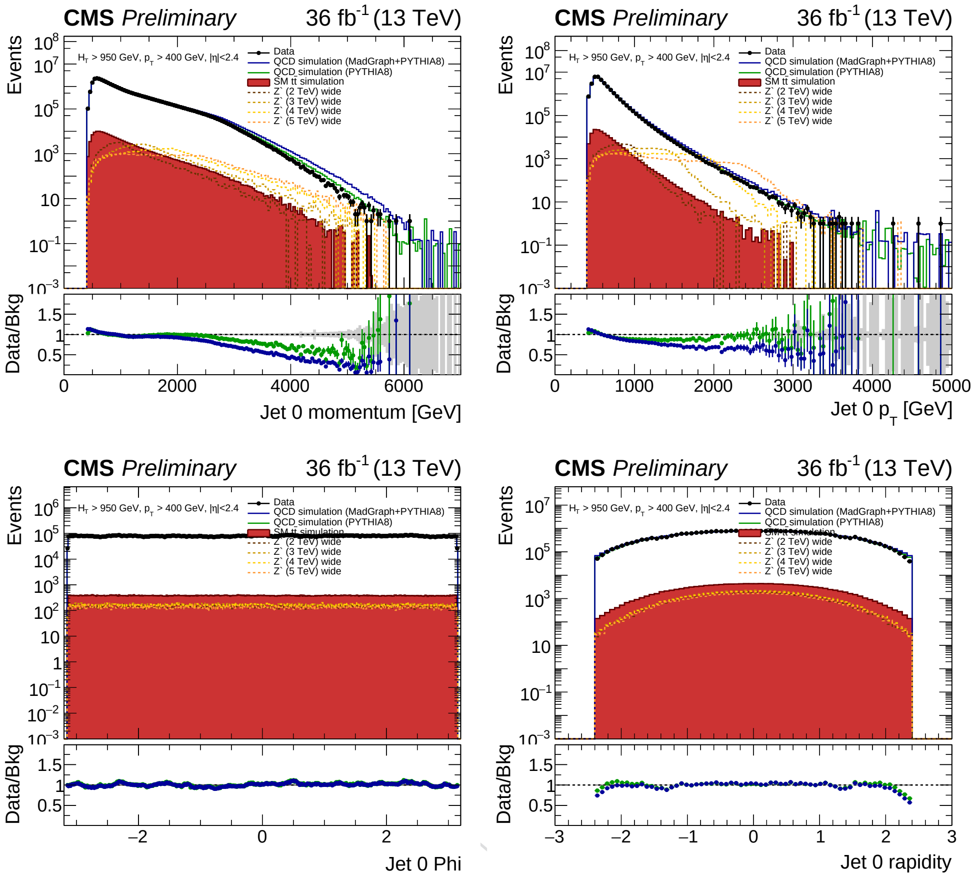

Figure 33: Leading jet kinematic plots after pre-selection (a) Jet 0 momentum (b) Jet 0 p_T (c) Jet 0 ϕ (d) Jet 0 rapidity

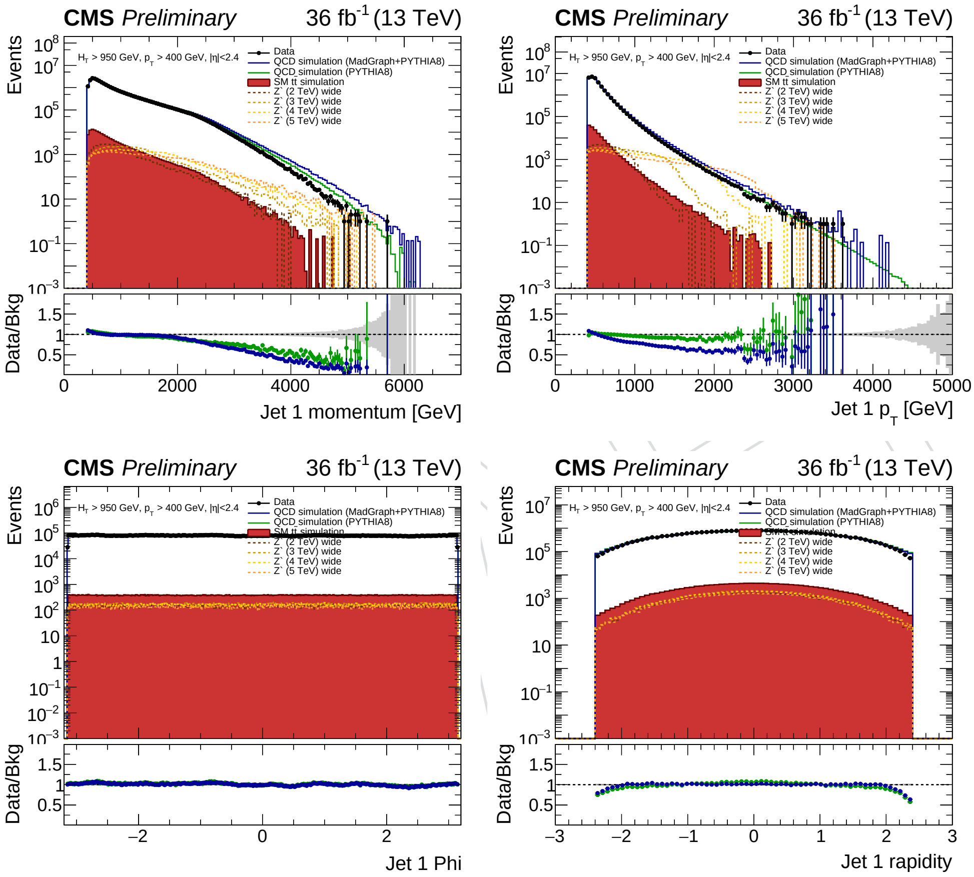

Figure 34: Second leading jet kinematic plots after pre-selection (a) Jet 1 momentum (b) Jet 1 p_T (c) Jet 1 ϕ (d) Jet 1 rapidity

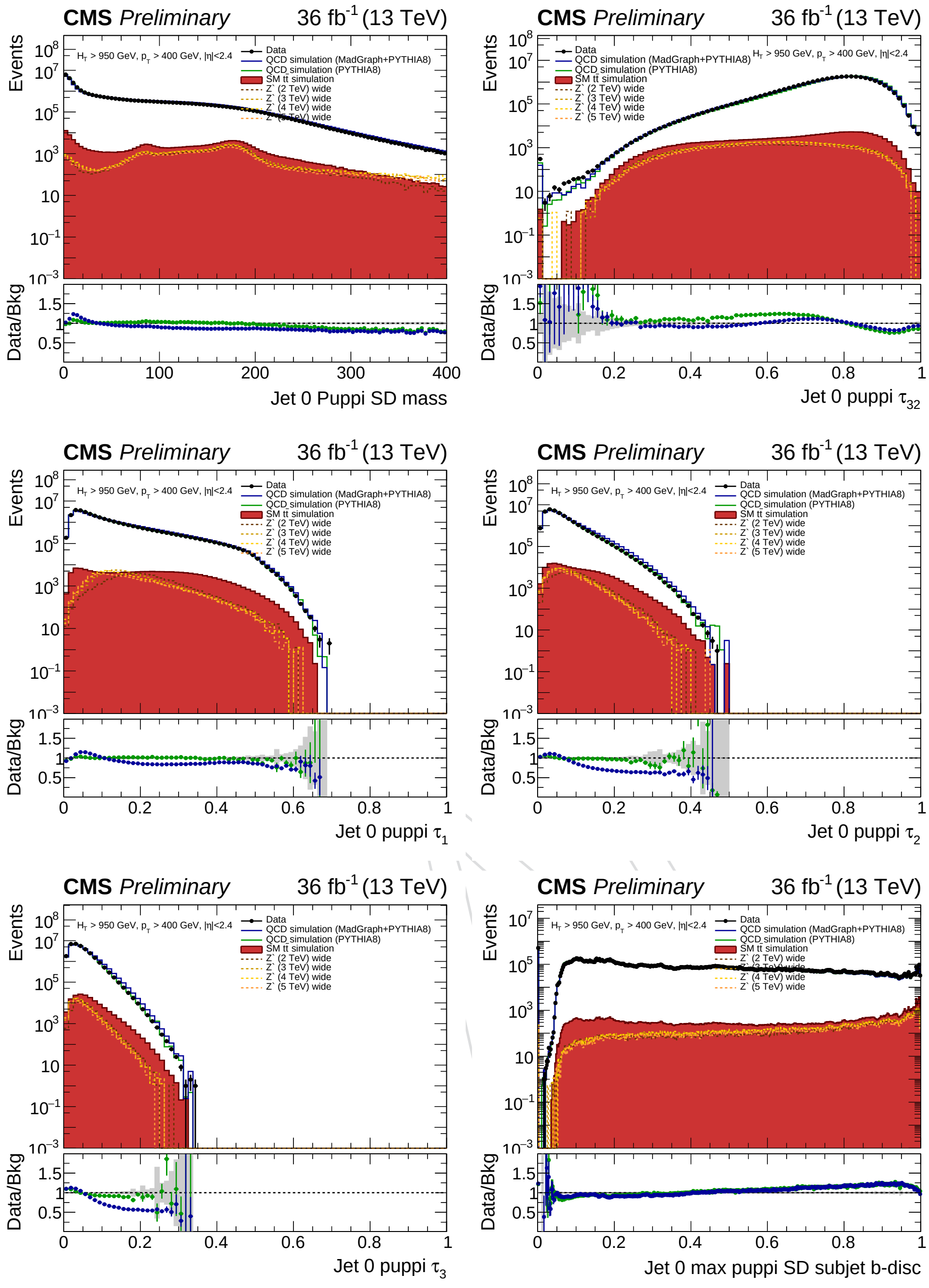

Figure 35: Jet 0 tagging variables after pre-selection

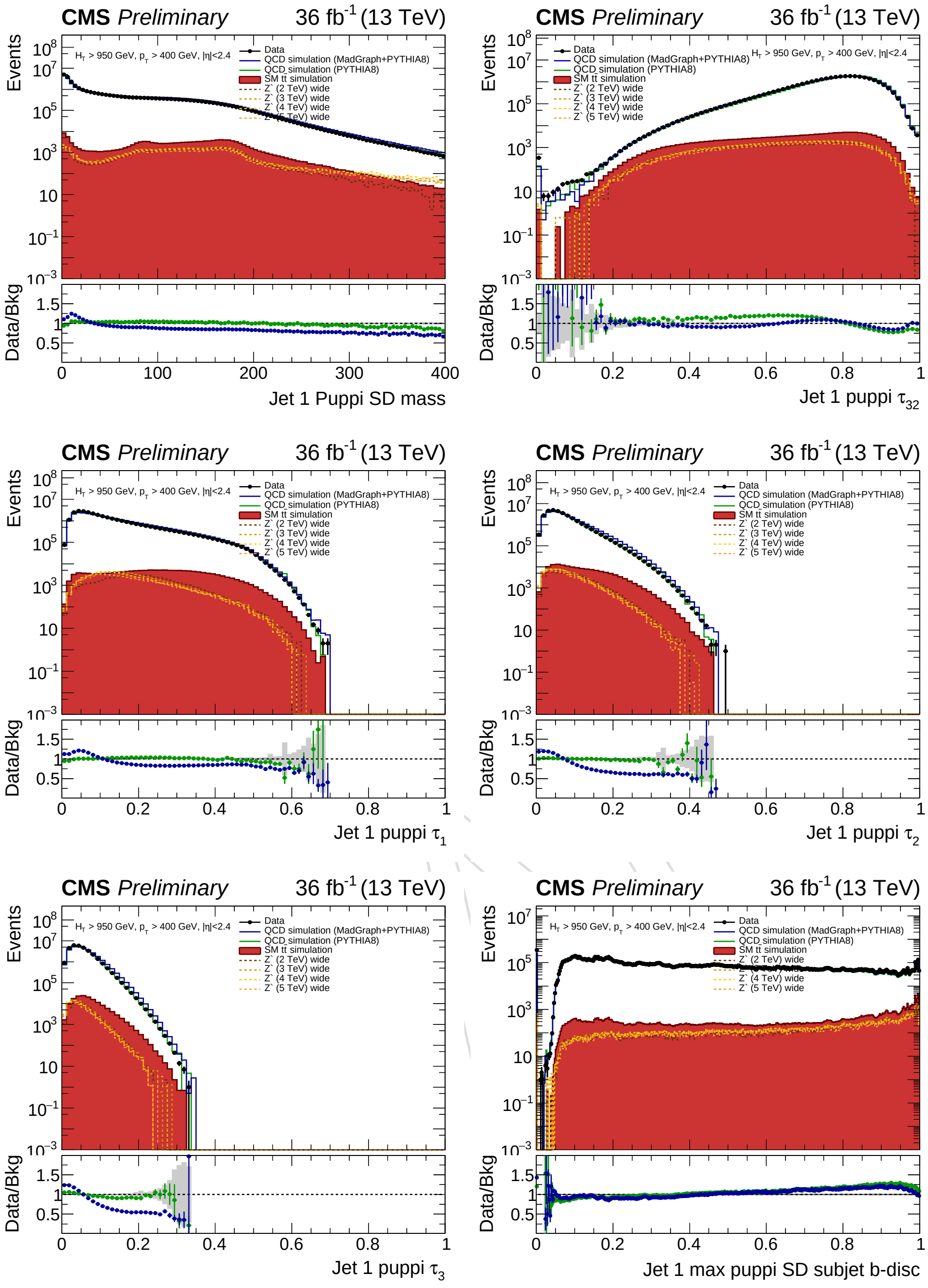

Figure 36: Jet 1 tagging variables after pre-selection

757 B Top p_{T} reweighting

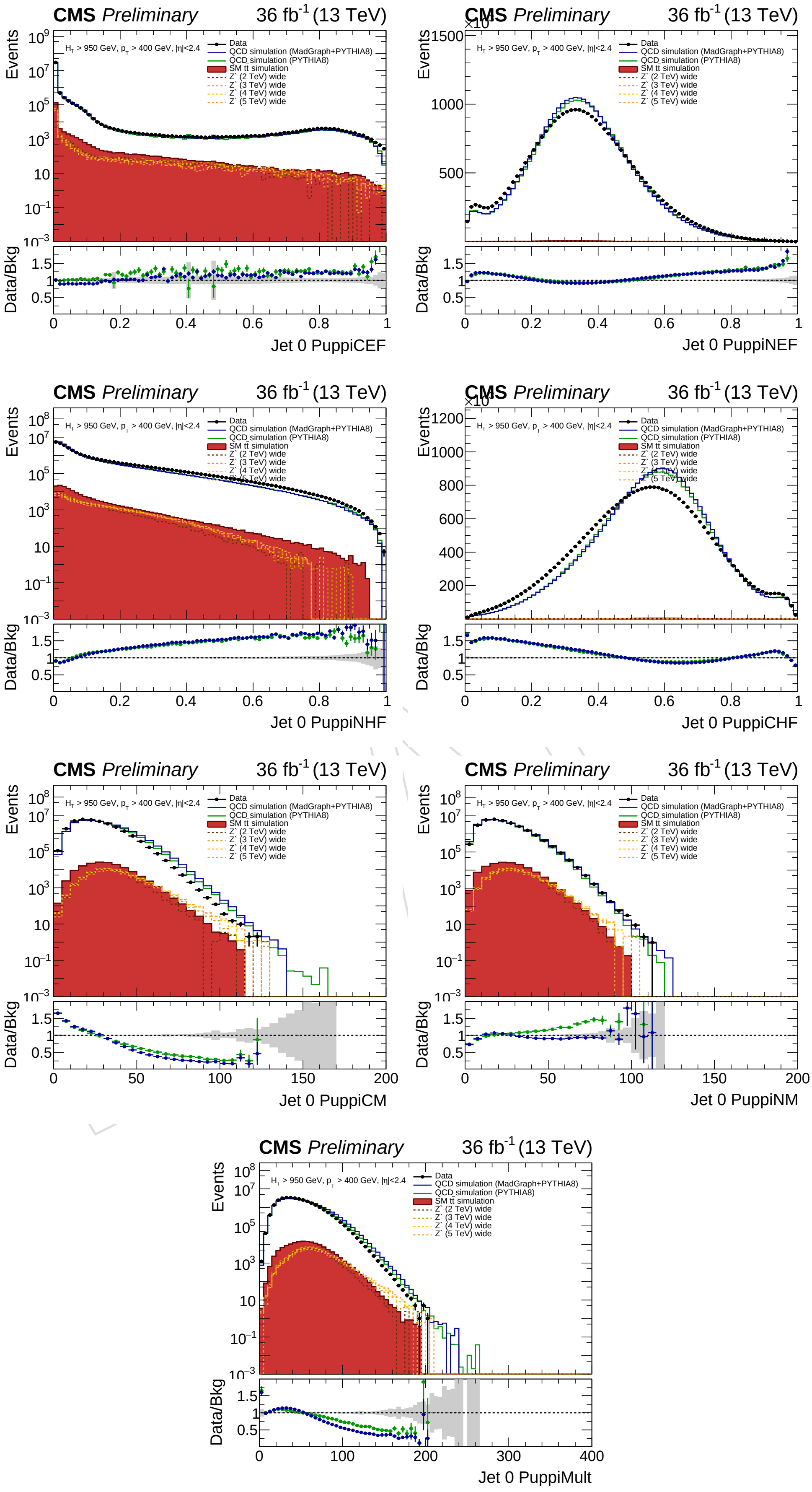

Figure 37: Leading jet PUPPI jet ID variables

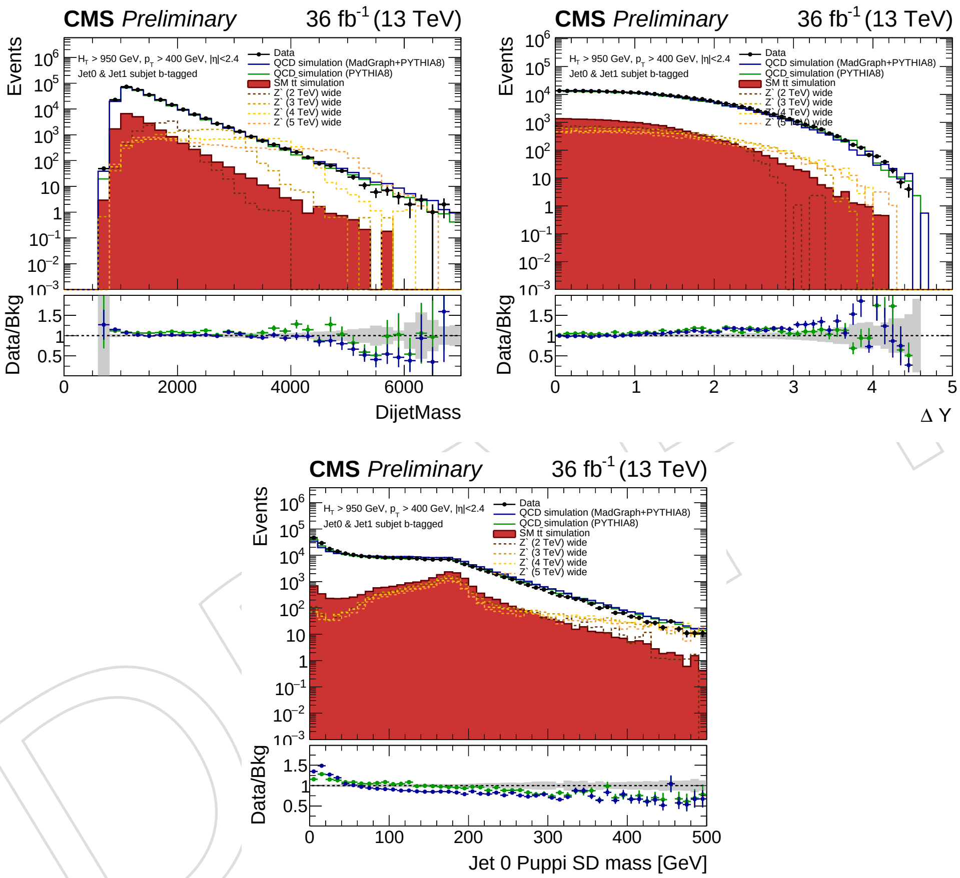

Figure 38: Event kinematic plots after pre-selection and requiring each jet have a subjet b-tag.

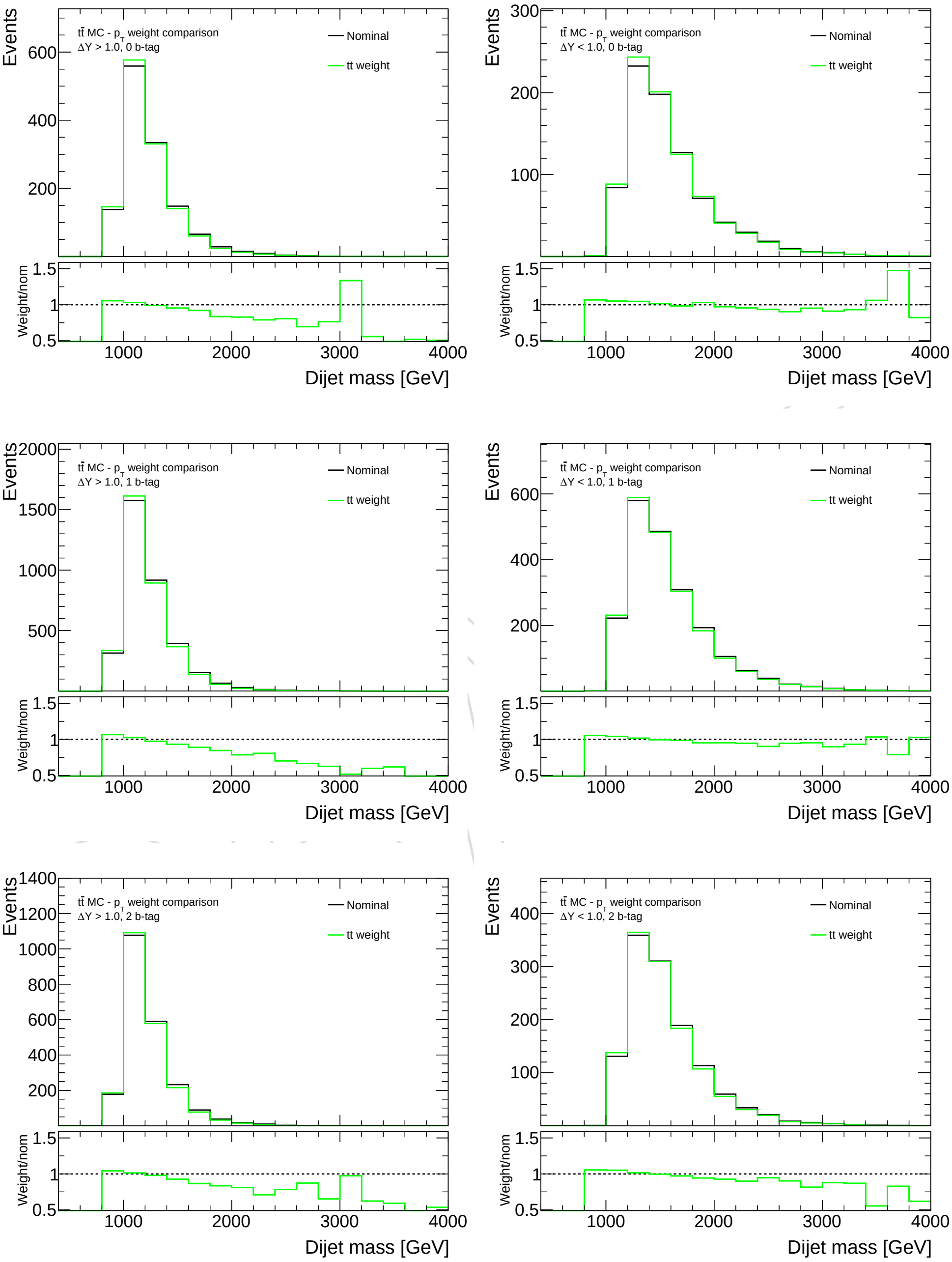

Figure 39: Effect of top p_{T} reweighting on the $t\bar{t}$ Monte Carlo sample for all 6 event categories.

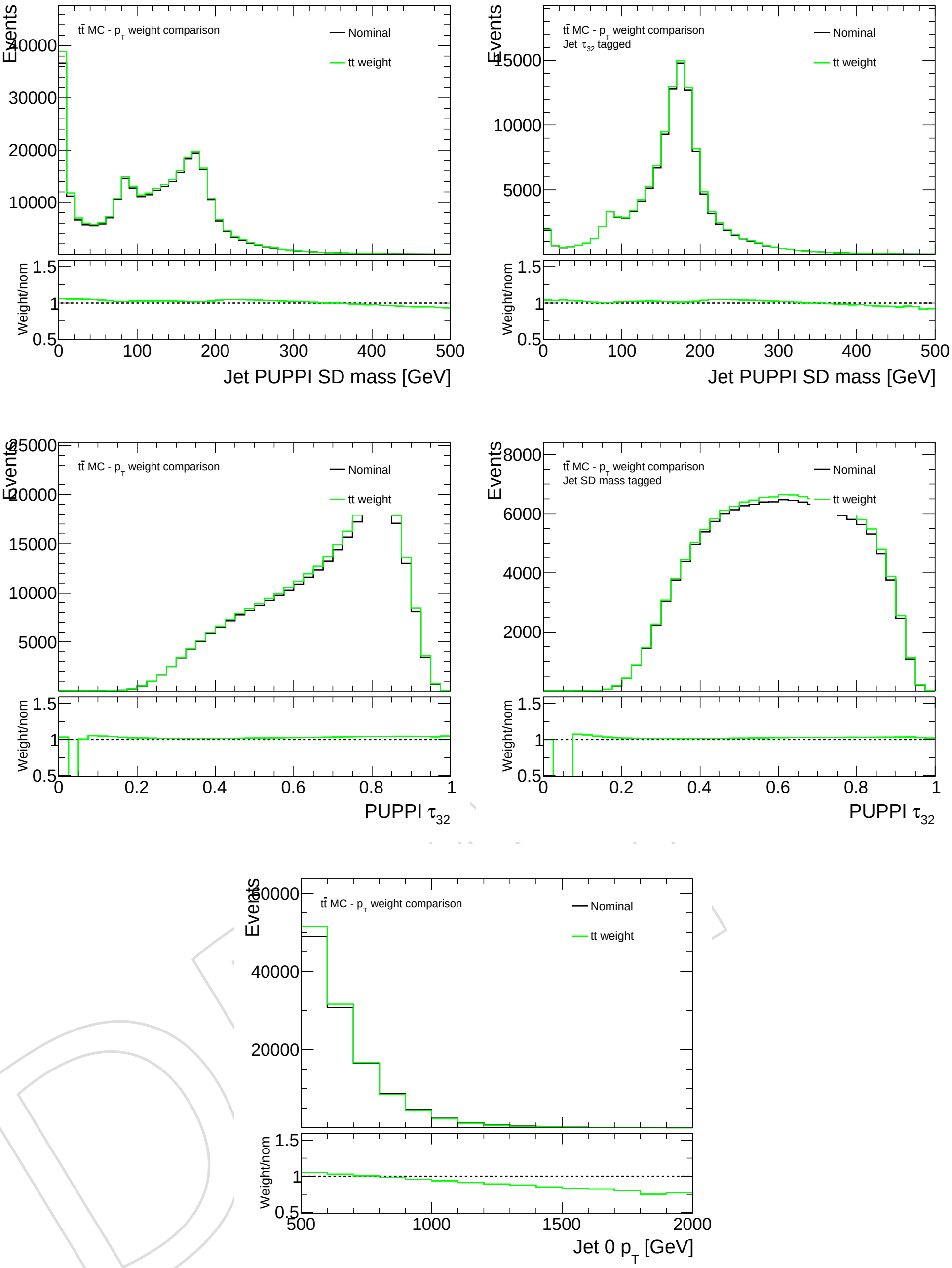

Figure 40: Effect of top p_T reweighting on jet variables.

C Systematic Shape Templates

In this section, we show all of the templates used to define the $\pm 1\sigma$ shape uncertainties on the simulated samples. These include jet energy scale, jet energy resolution, b-tagging scale factor, PDF, pileup, Q^2, QCD modificed mass, and QCD closure uncertainties.

C.1 Jet Energy Scale

Standard Model ttbar

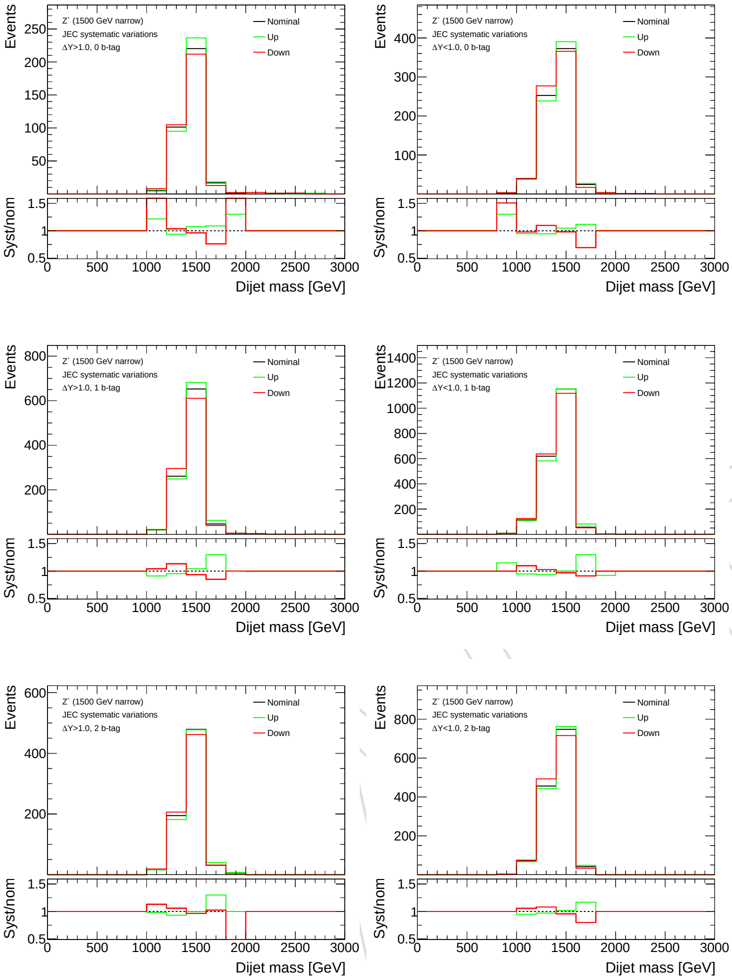

Figure 41: Effect of jet energy scale uncertainties on the $m_{t\bar{t}}$ shape for the $t\bar{t}$ Monte Carlo sample for all 6 event categories.

Z’ (1.5 TeV) narrow

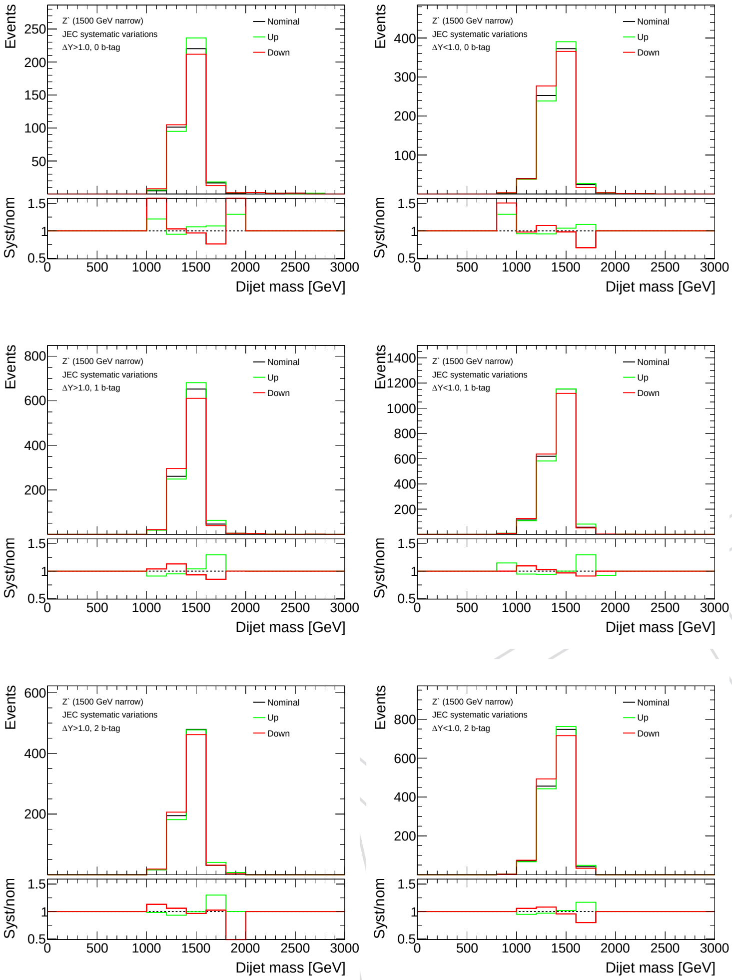

Figure 42: Effect of jet energy scale uncertainties on the $m_{t\bar{t}}$ shape for the narrow 1.5 TeV Z' Monte Carlo sample for all 6 event categories.

Z’ (3 TeV) narrow

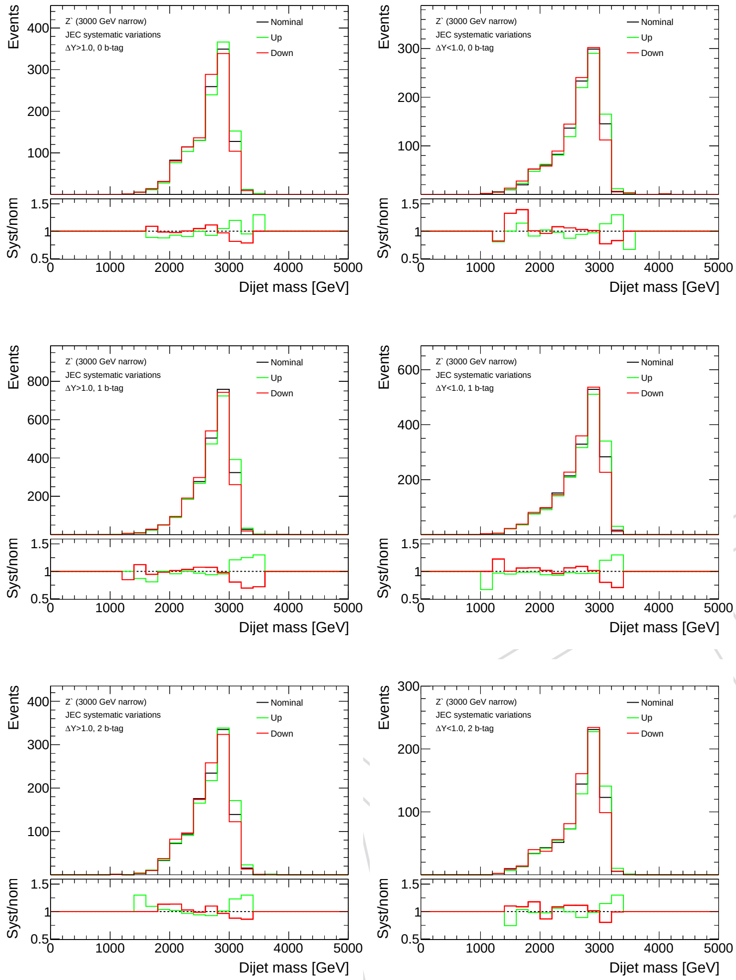

Figure 43: Effect of jet energy scale uncertainties on the $m_{t\bar{t}}$ shape for the narrow 3 TeV Z' Monte Carlo sample for all 6 event categories.

Z' (5 TeV) narrow

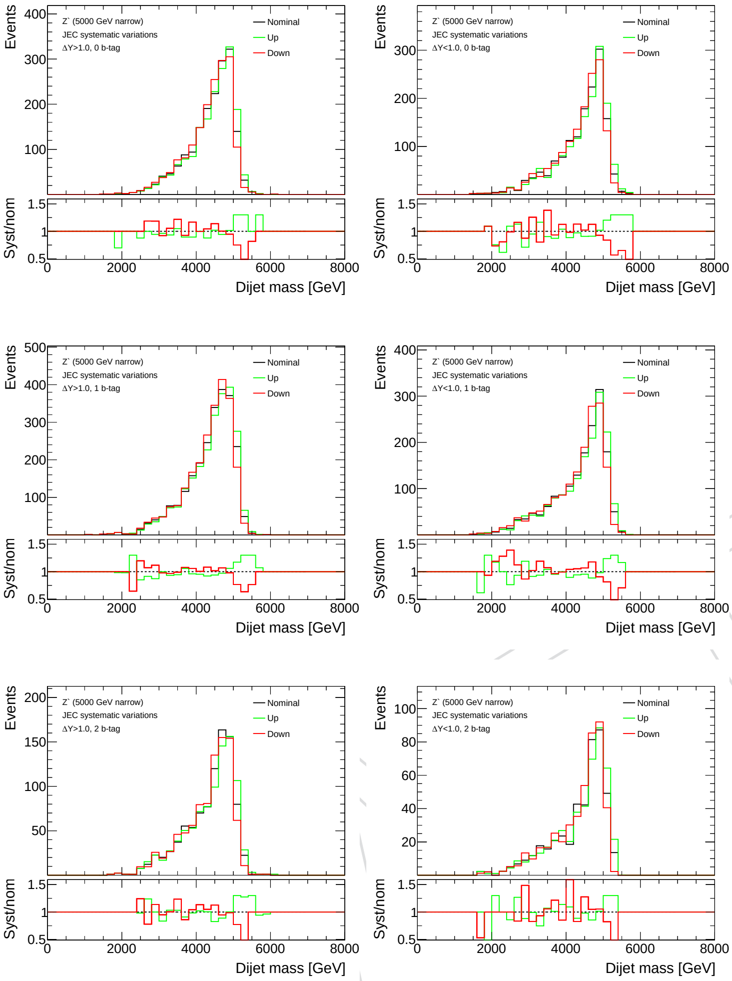

Figure 44: Effect of jet energy scale uncertainties on the $m_{t\bar{t}}$ shape for the narrow 5 TeV Z' Monte Carlo sample for all 6 event categories.

Z’ (1.5 TeV) wide

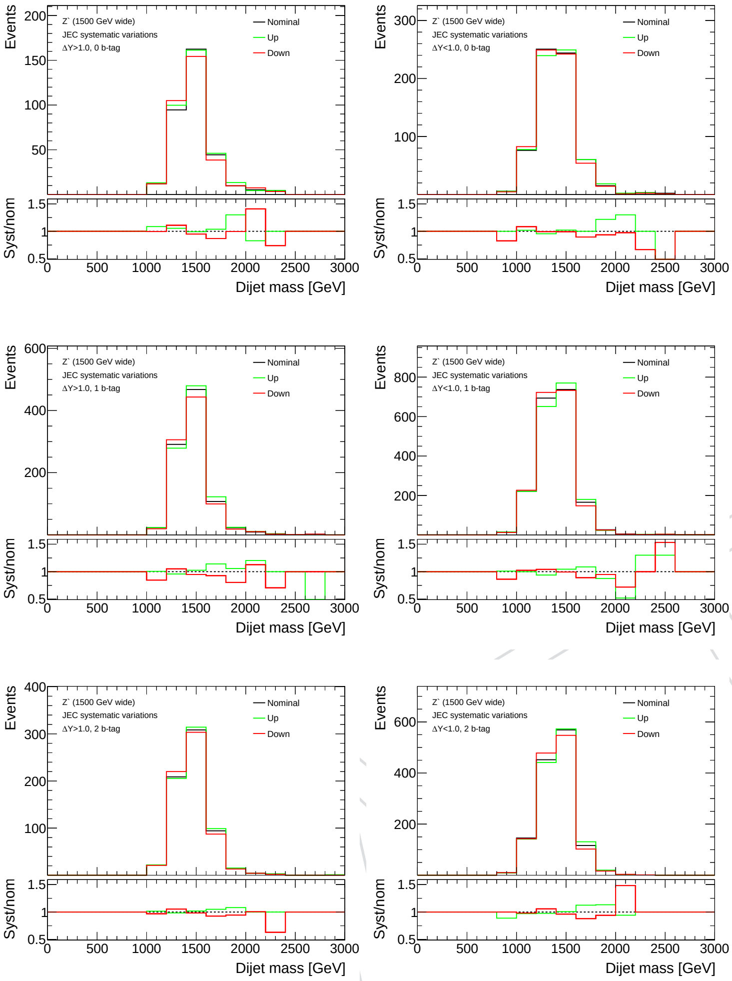

Figure 45: Effect of jet energy scale uncertainties on the $m_{t\bar{t}}$ shape for the wide 1.5 TeV Z′ Monte Carlo sample for all 6 event categories.

Z’ (3 TeV) wide

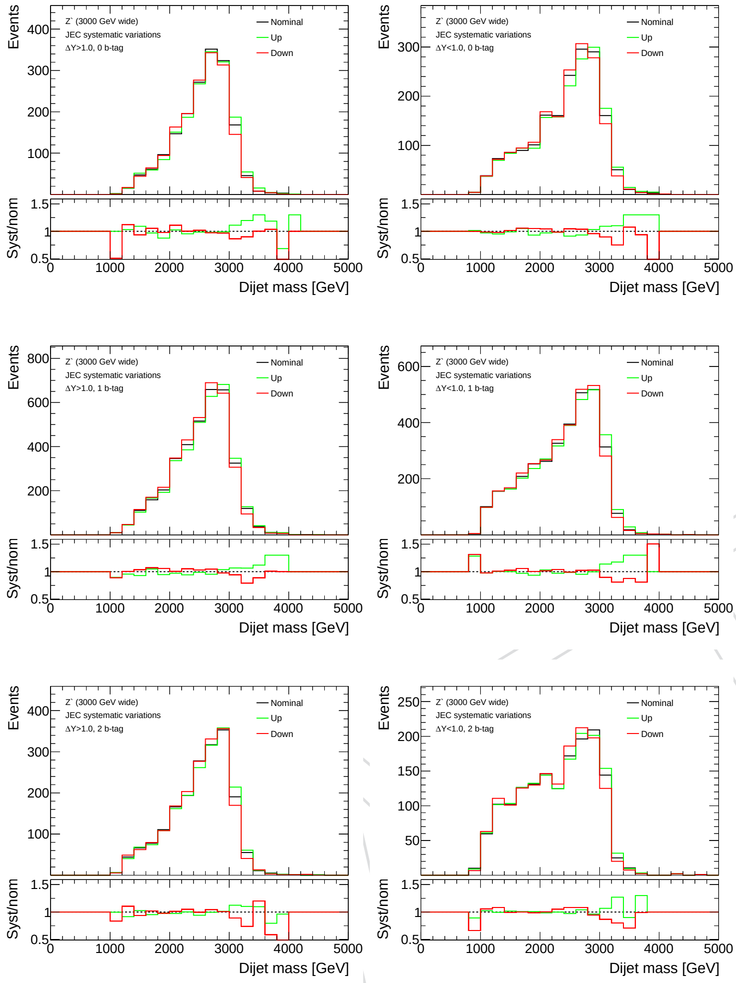

Figure 46: Effect of jet energy scale uncertainties on the $m_{t\bar{t}}$ shape for the wide 3 TeV Z′ Monte Carlo sample for all 6 event categories.

Z’ (5 TeV) wide

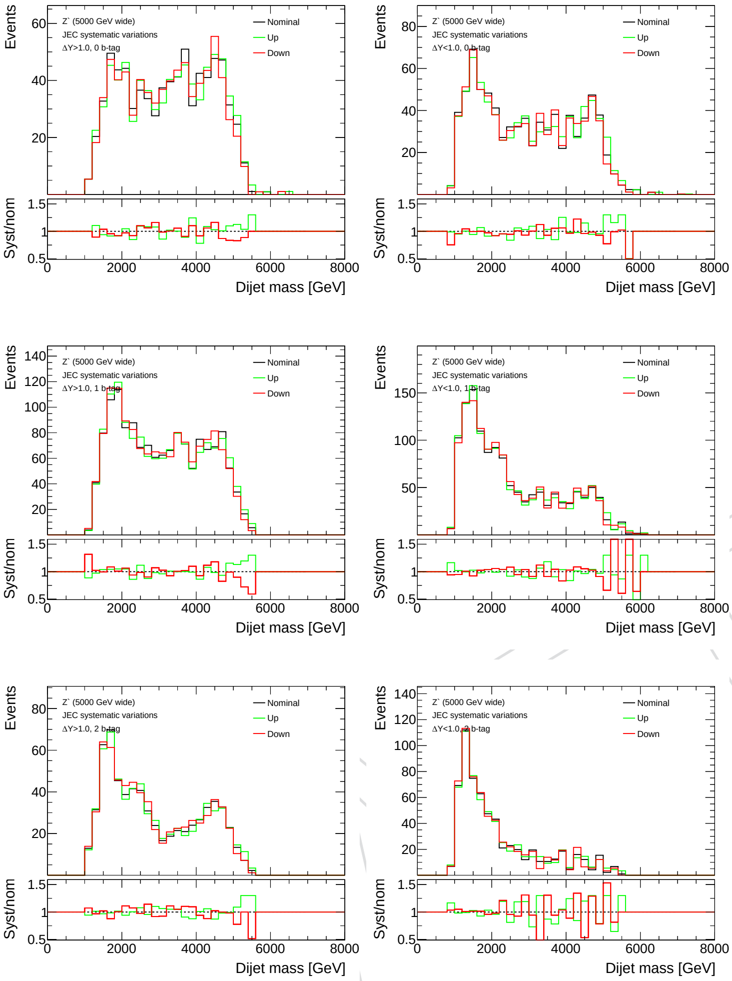

Figure 47: Effect of jet energy scale uncertainties on the $m_{t\bar{t}}$ shape for the wide 5 TeV Z' Monte Carlo sample for all 6 event categories.

RS Gluon (1.5 TeV)

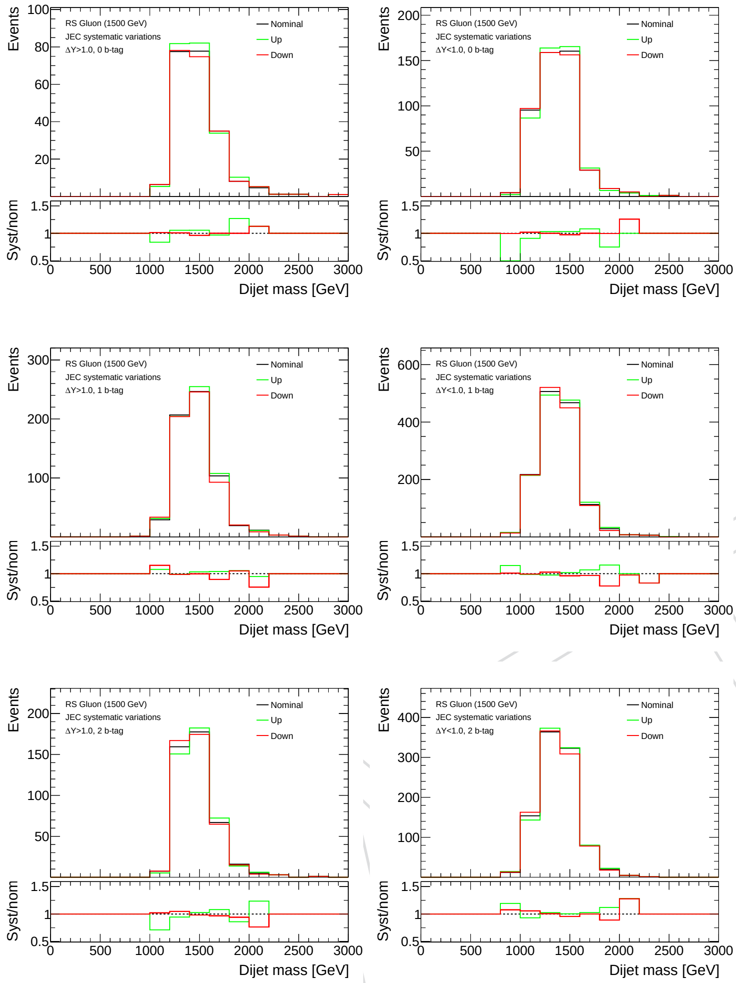

Figure 48: Effect of jet energy scale uncertainties on the $m_{t\bar{t}}$ shape for the 1.5 TeV RS Gluon sample for all 6 event categories.

RS Gluon (3 TeV)

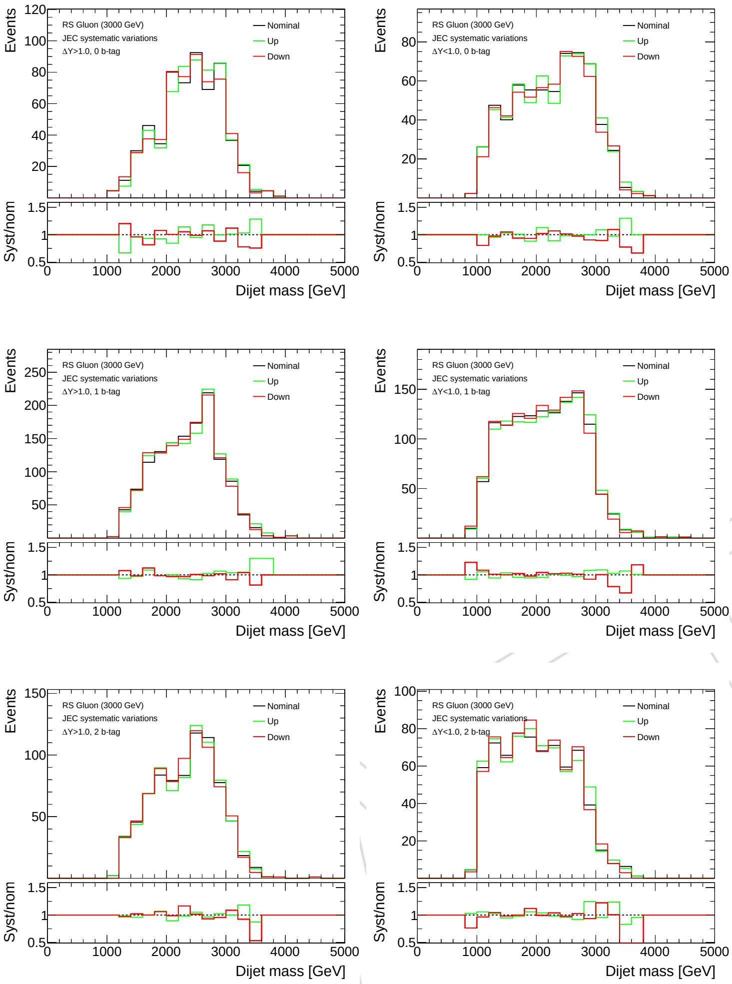

Figure 49: 3 TeV sample for all 6 event categories.

772 C.2 Jet Energy Resolution

773 Standard Model ttbar

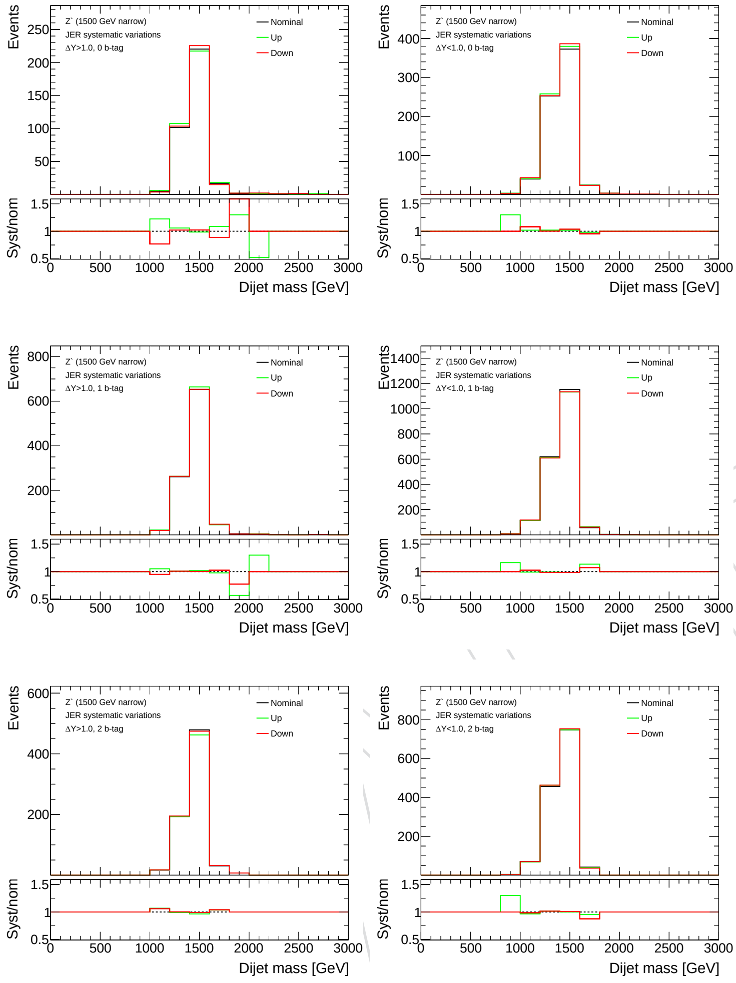

Figure 50: Effect of jet energy resolution uncertainties on the $m_{t\bar{t}}$ shape for the $t\bar{t}$ Monte Carlo sample for all 6 event categories.

Z’ (1.5 TeV) narrow

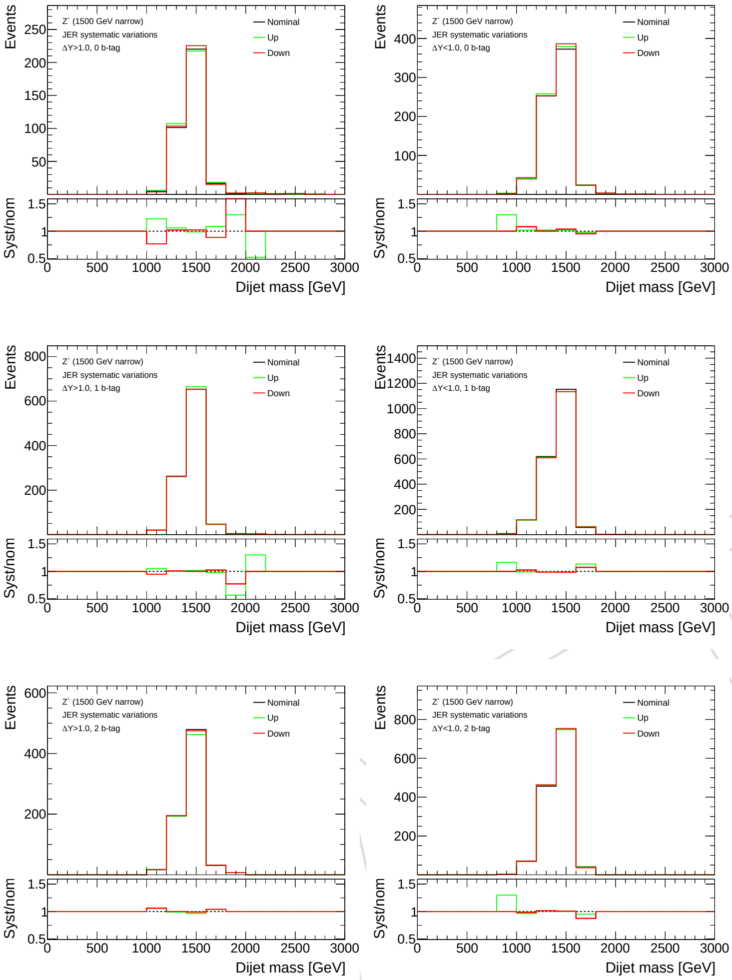

Figure 51: Effect of jet energy resolution uncertainties on the $m_{t\bar{t}}$ shape for the narrow 1.5 TeV Z′ Monte Carlo sample for all 6 event categories.

775 Z’ (3 TeV) narrow

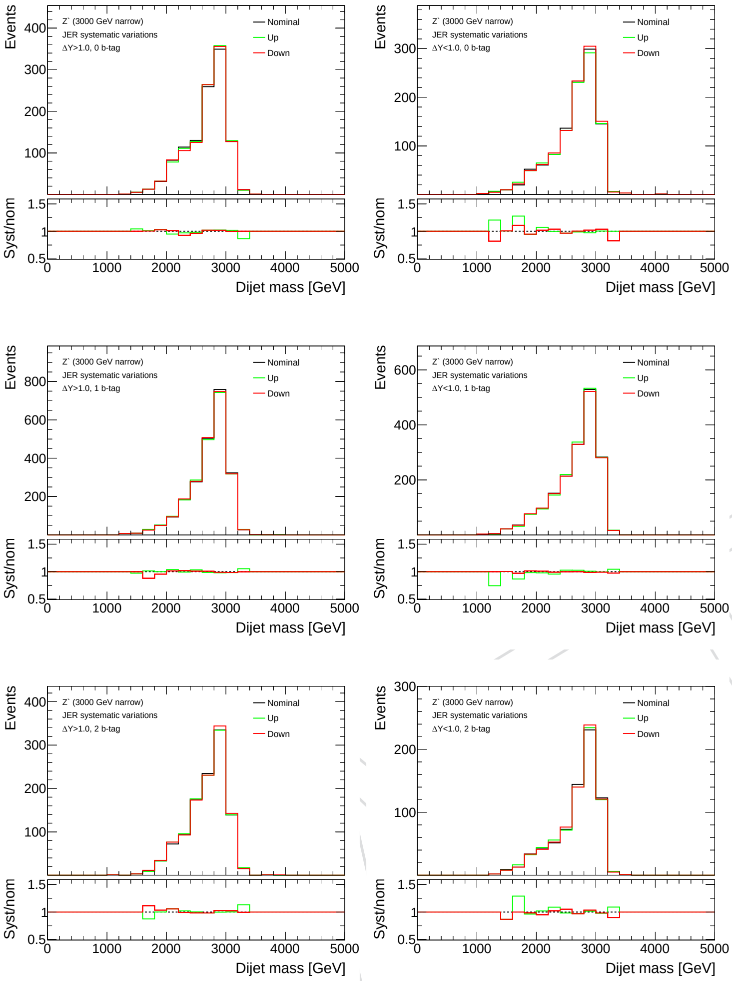

Figure 52: Effect of jet energy resolution uncertainties on the $m_{t\bar{t}}$ shape for the narrow 3 TeV Z′ Monte Carlo sample for all 6 event categories.

Z’ (5 TeV) narrow

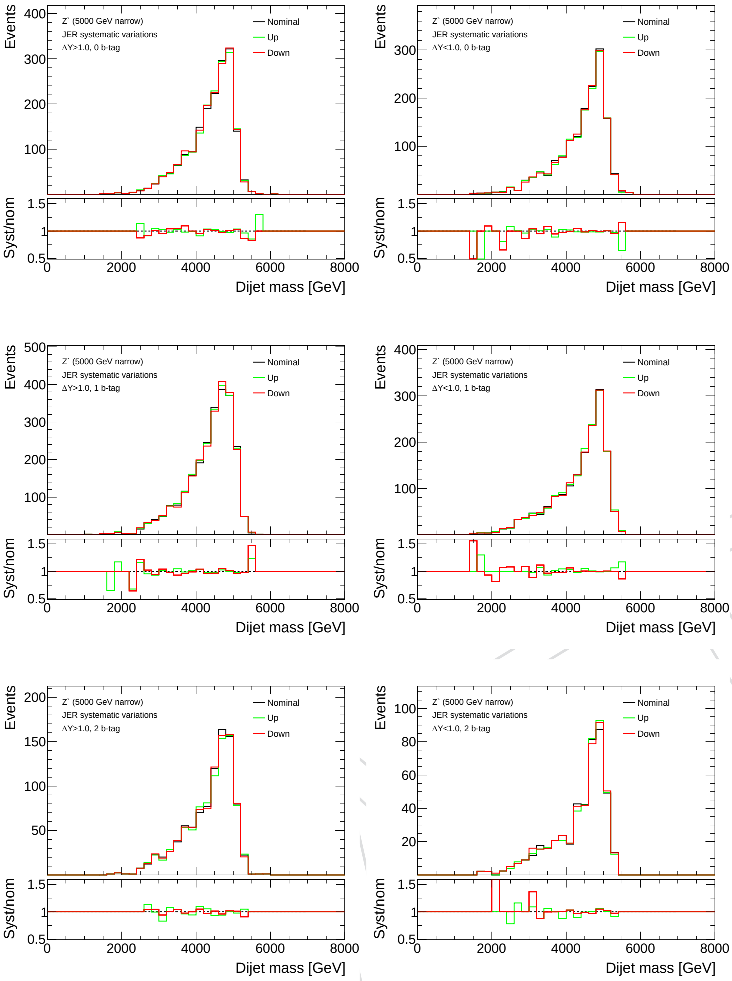

Figure 53: Effect of jet energy resolution uncertainties on the $m_{t\bar{t}}$ shape for the narrow 5 TeV Z' Monte Carlo sample for all 6 event categories.

Z’ (1.5 TeV) wide

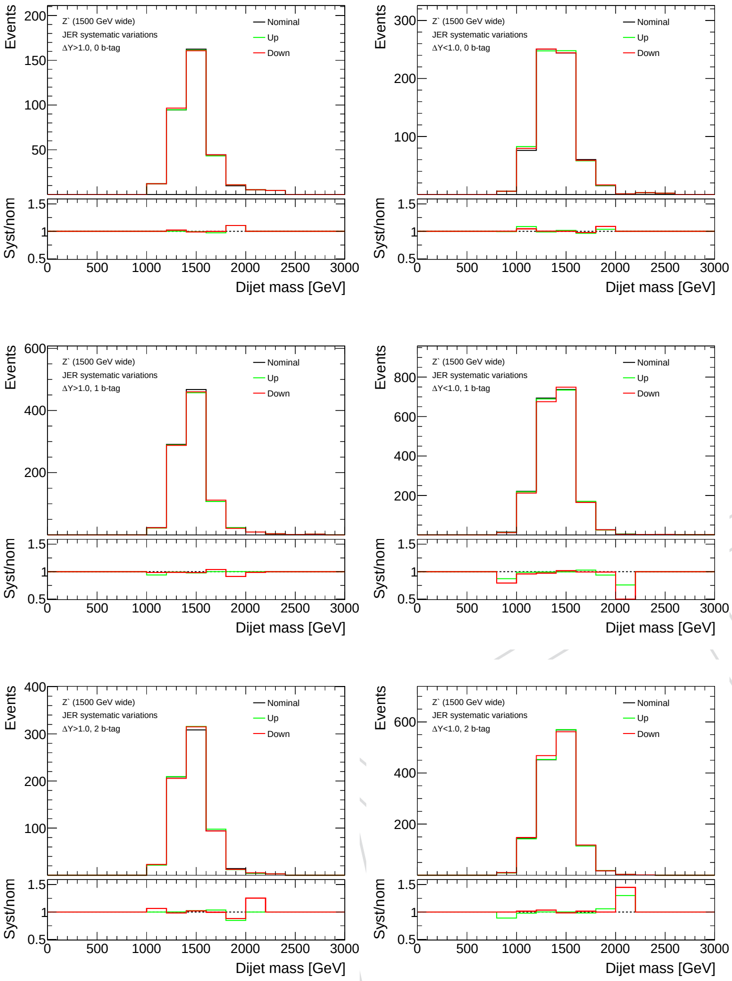

Figure 54: Effect of jet energy resolution uncertainties on the $m_{t\bar{t}}$ shape for the wide 1.5 TeV Z' Monte Carlo sample for all 6 event categories.

Z’ (3 TeV) wide

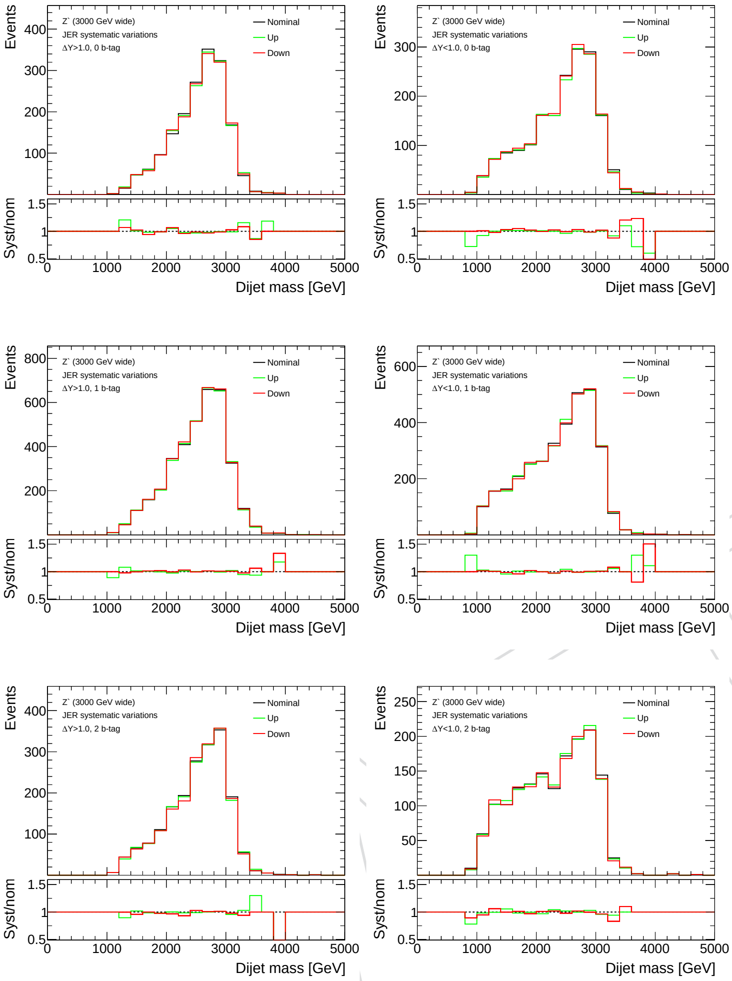

Figure 55: Effect of jet energy resolution uncertainties on the $m_{t\bar{t}}$ shape for the wide 3 TeV Z′ Monte Carlo sample for all 6 event categories.

Z' (5 TeV) wide

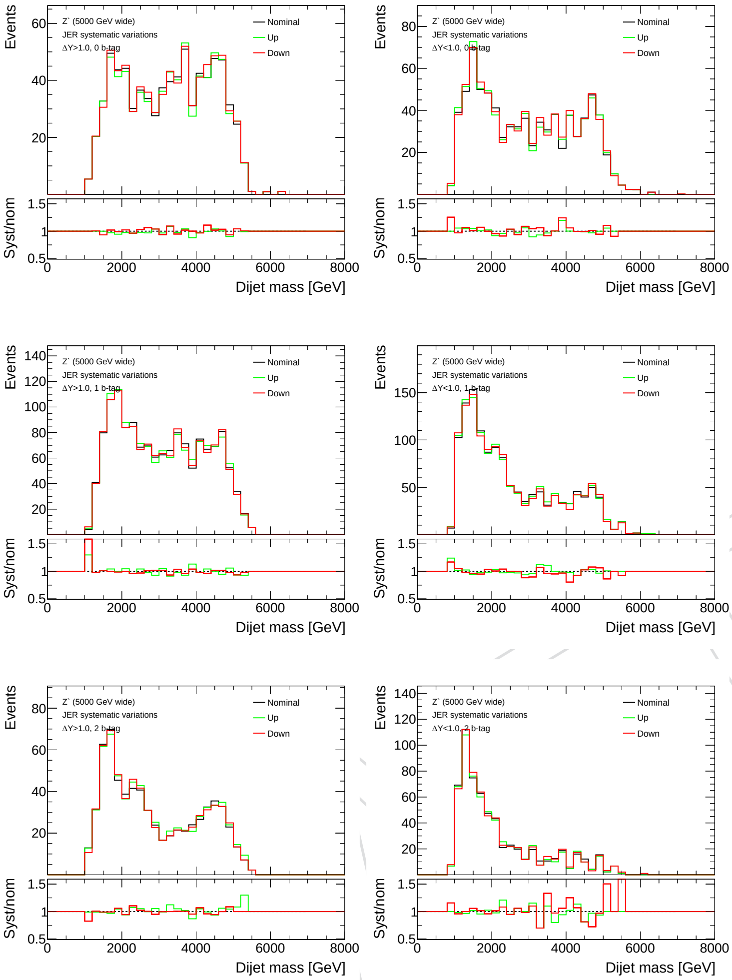

Figure 56: Effect of jet energy resolution uncertainties on the $m_{t\bar{t}}$ shape for the wide 5 TeV Z' Monte Carlo sample for all 6 event categories.

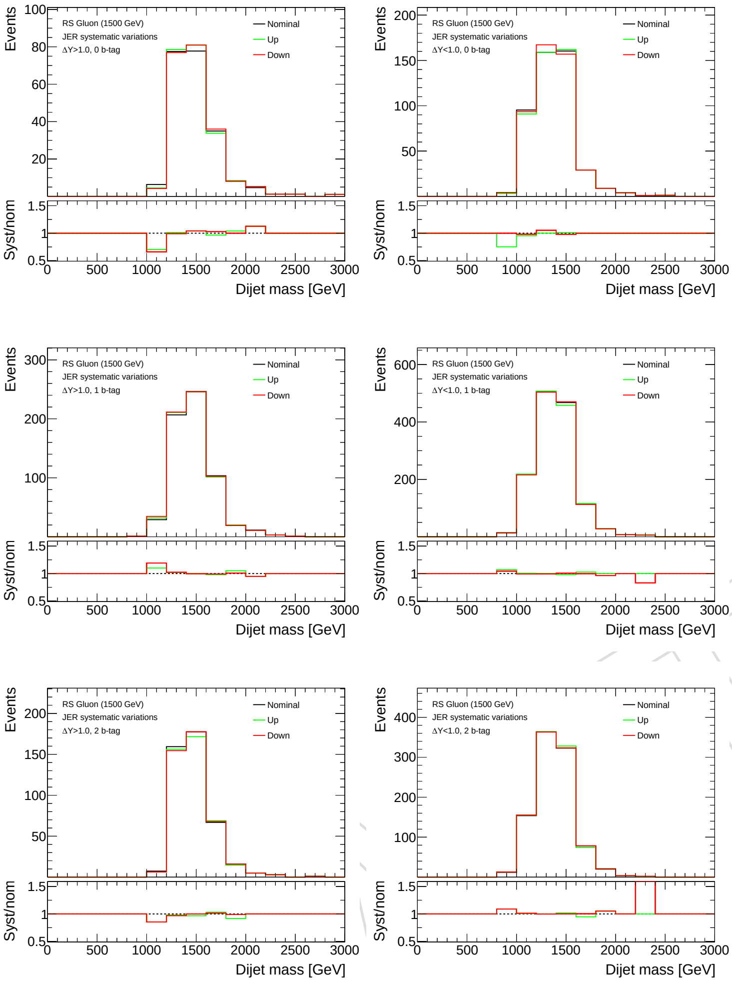

Figure 57: Effect of jet energy resolution uncertainties on the $m_{t\bar{t}}$ shape for the 1.5 TeV RS GLuon sample for all 6 event categories.

RS Gluon (3 TeV)

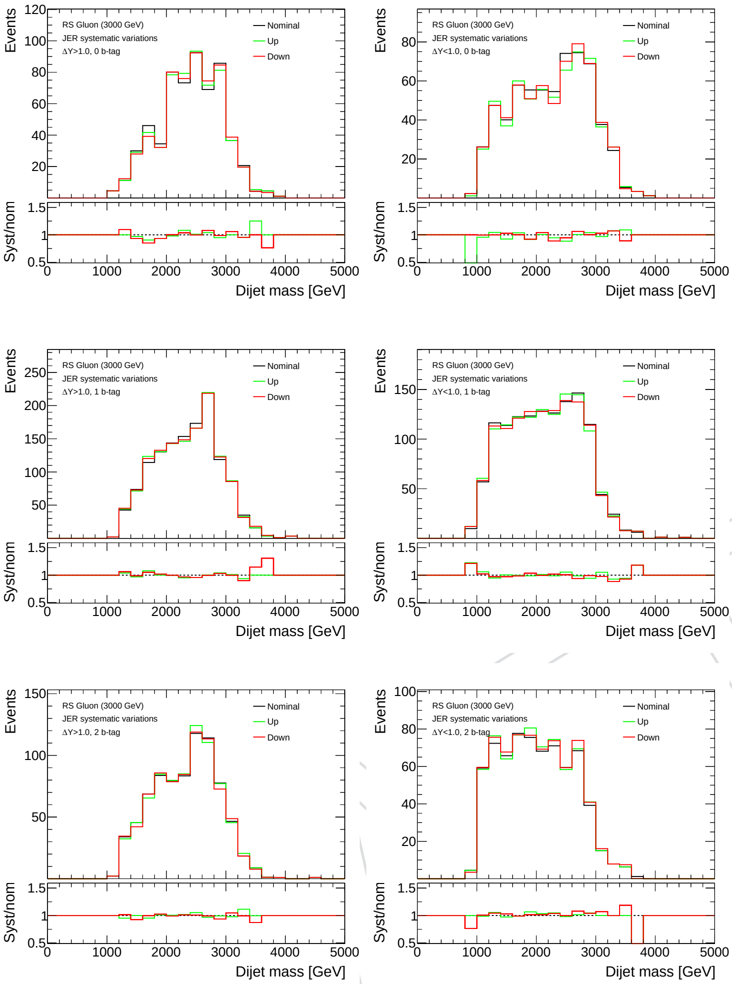

Figure 58: Effect of jet energy resolution uncertainties on the $m_{t\bar{t}}$ shape for the 3 TeV RS Gluon sample for all 6 event categories.

C.3 b-tag SF Uncertainty

Standard Model ttbar

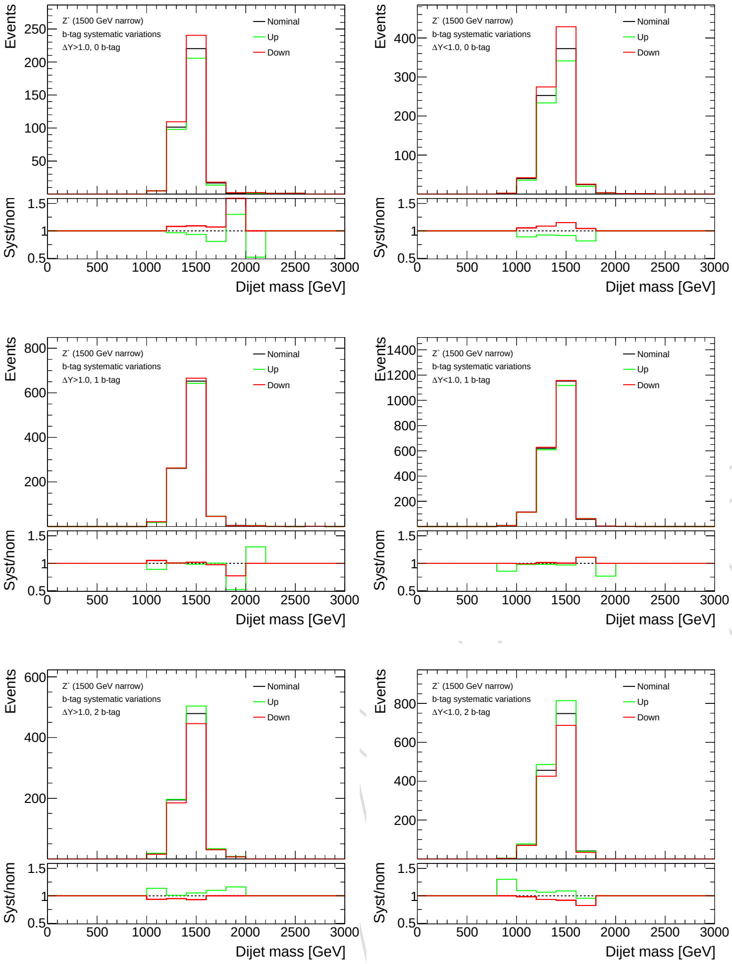

Figure 59: Effect of the b-tag scale factor uncertainties on the $m_{t\bar{t}}$ shape for the $t\bar{t}$ Monte Carlo sample for all 6 event categories.

Z’ (1.5 TeV) narrow

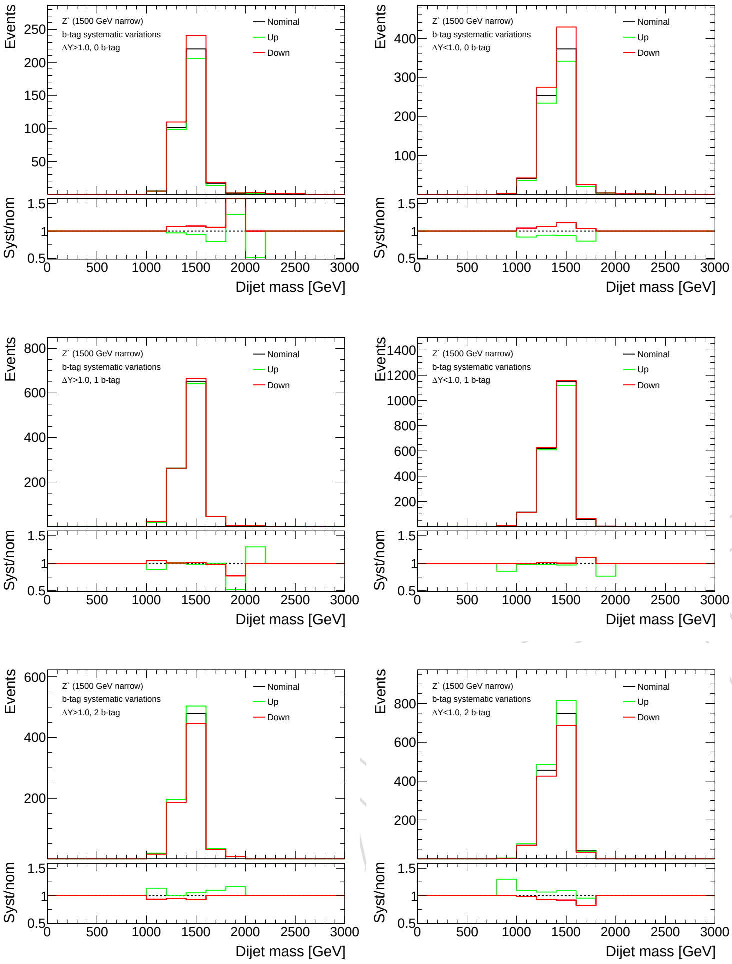

Figure 60: Effect of the b-tag scale factor uncertainties on the $m_{t\bar{t}}$ shape for the narrow 1.5 TeV Z′ Monte Carlo sample for all 6 event categories.

Z’ (3 TeV) narrow

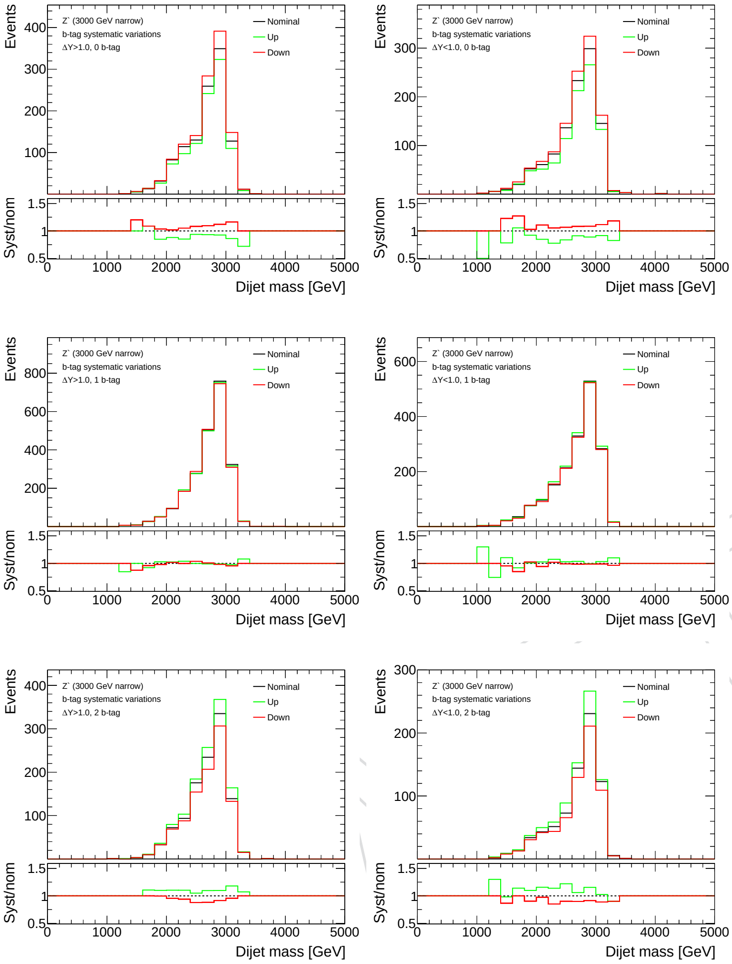

Figure 61: Effect of the b-tag scale factor uncertainties on the $m_{t\bar{t}}$ shape for the narrow 3 TeV Z′ Monte Carlo sample for all 6 event categories.

Z’ (5 TeV) narrow

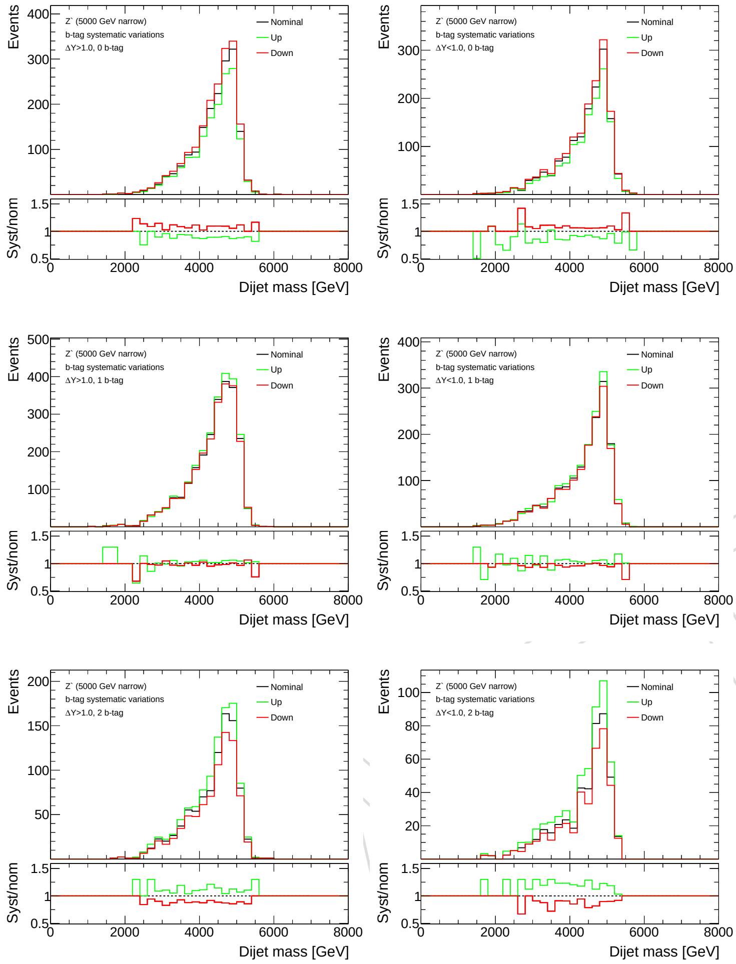

Figure 62: Effect of the b-tag scale factor uncertainties on the $m_{t\bar{t}}$ shape for the narrow 5 TeV Z' Monte Carlo sample for all 6 event categories.

Z’ (1.5 TeV) wide

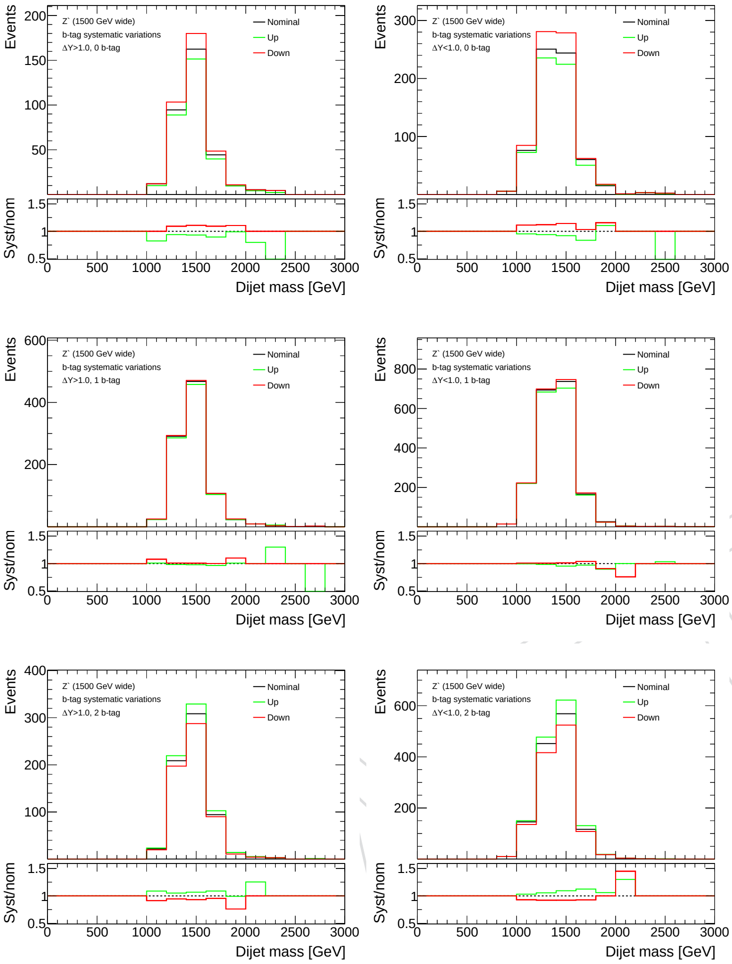

Figure 63: Effect of the b-tag scale factor uncertainties on the $m_{t\bar{t}}$ shape for the wide 1.5 TeV Z′ Monte Carlo sample for all 6 event categories.

Z’ (3 TeV) wide

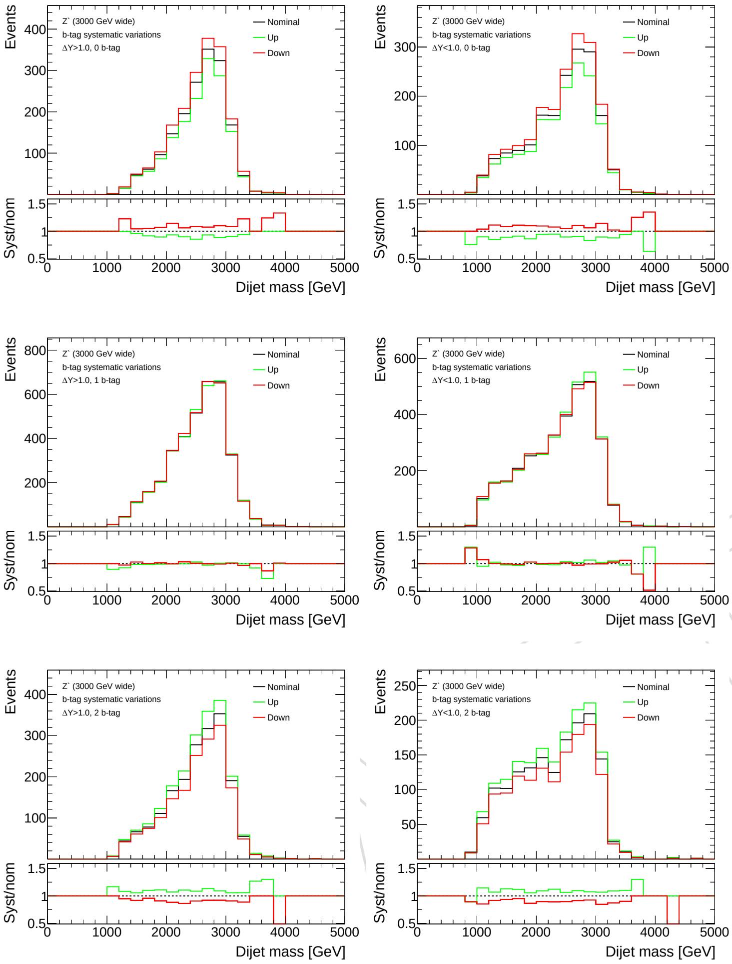

Figure 64: Effect of the b-tag scale factor uncertainties on the $m_{t\bar{t}}$ shape for the wide 3 TeV Z′ Monte Carlo sample for all 6 event categories.

Z' (5 TeV) wide

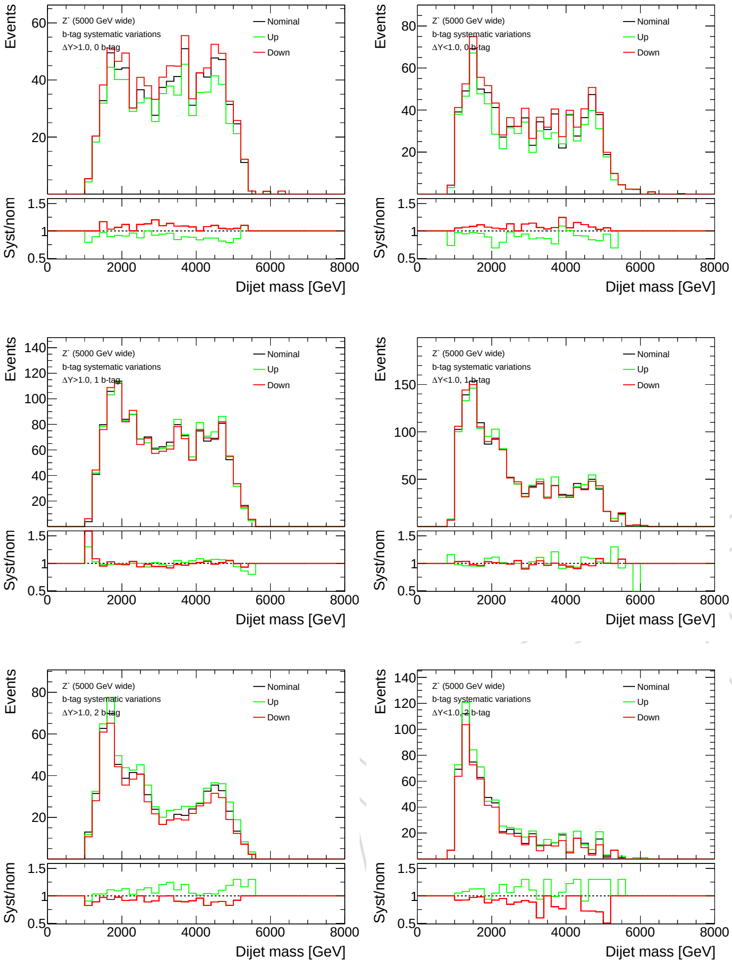

Figure 65: Effect of the b-tag scale factor uncertainties on the $m_{t\bar{t}}$ shape for the wide 5 TeV Z′ Monte Carlo sample for all 6 event categories.

RS Gluon (1.5 TeV)

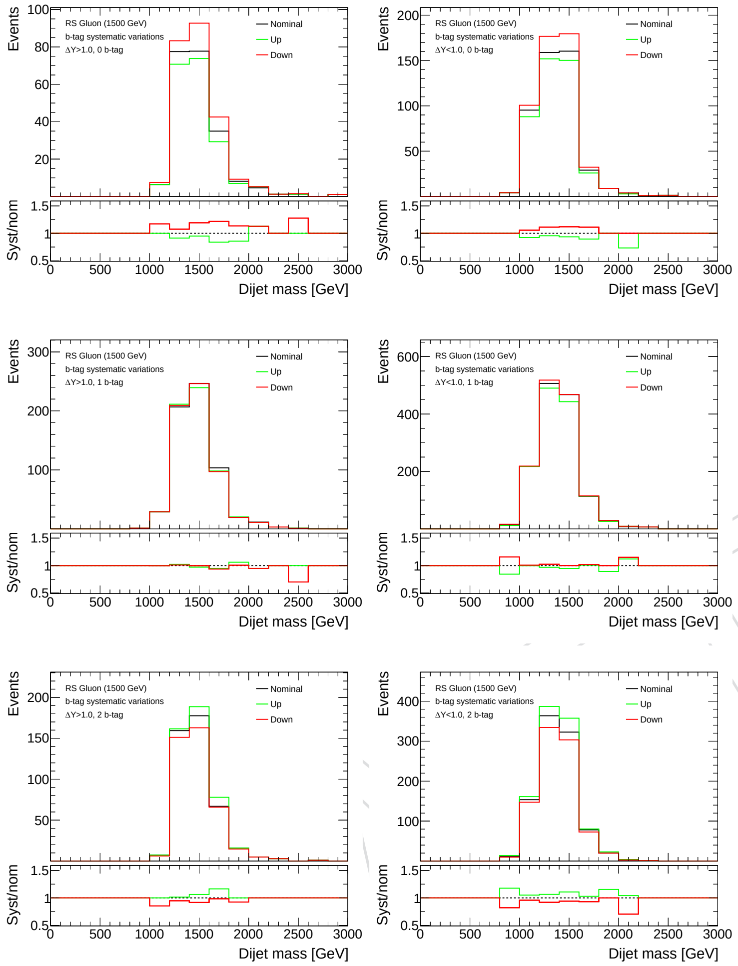

Figure 66: Effect of the b-tag scale factor uncertainties on the $m_{t\bar{t}}$ shape for the 1.5 TeV RS GLuon sample for all 6 event categories.

790 RS Gluon (3 TeV)

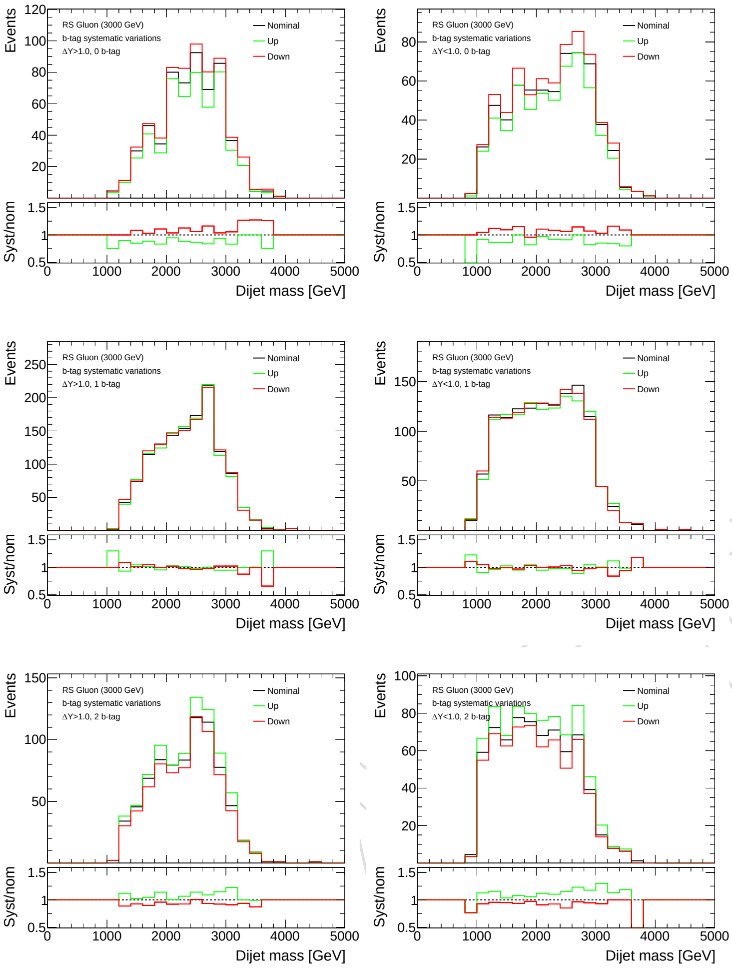

Figure 67: Effect of the b-tag scale factor uncertainties on the $m_{t\bar{t}}$ shape for the 3 TeV RS Gluon sample for all 6 event categories.

C.4 PDF Uncertainty

Standard Model ttbar

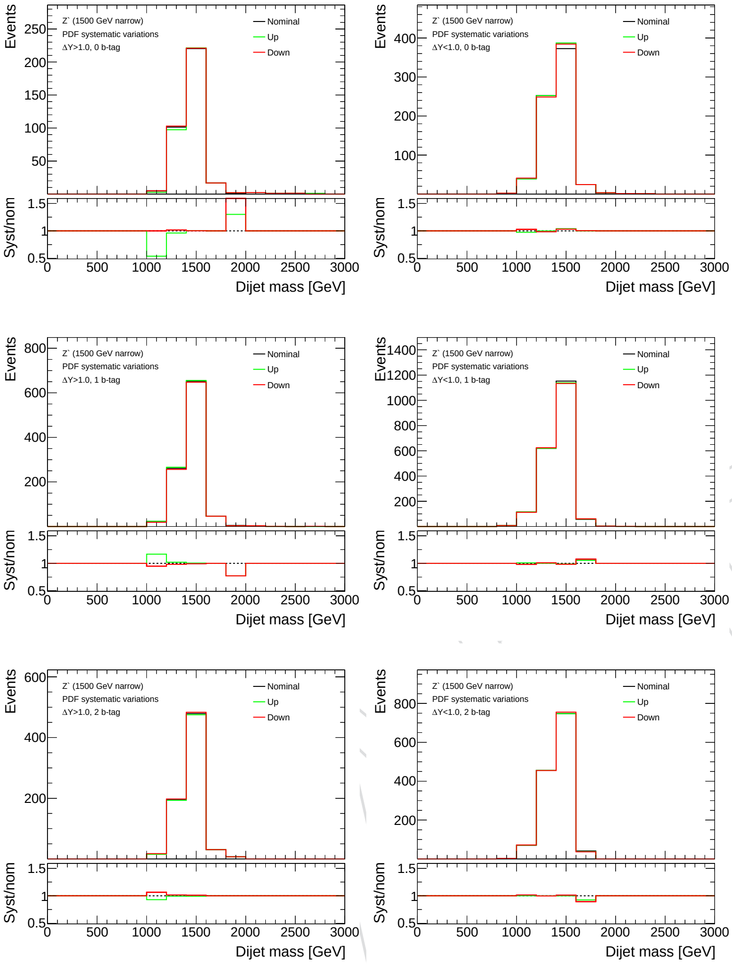

Figure 68: Effect of the PDF uncertainties on the $m_{t\bar{t}}$ shape for the $t\bar{t}$ Monte Carlo sample for all 6 event categories.

793 Z' (1.5 TeV) narrow

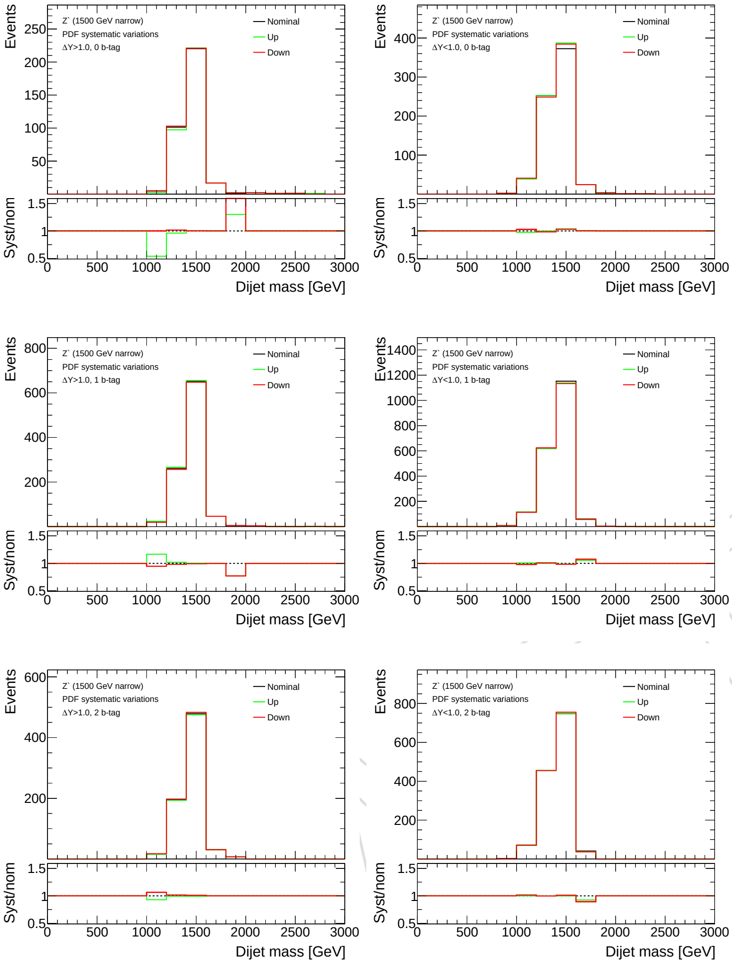

Figure 69: Effect of the PDF uncertainties on the $m_{t\bar{t}}$ shape for the narrow 1.5 TeV Z′ Monte Carlo sample for all 6 event categories.

Z’ (3 TeV) narrow

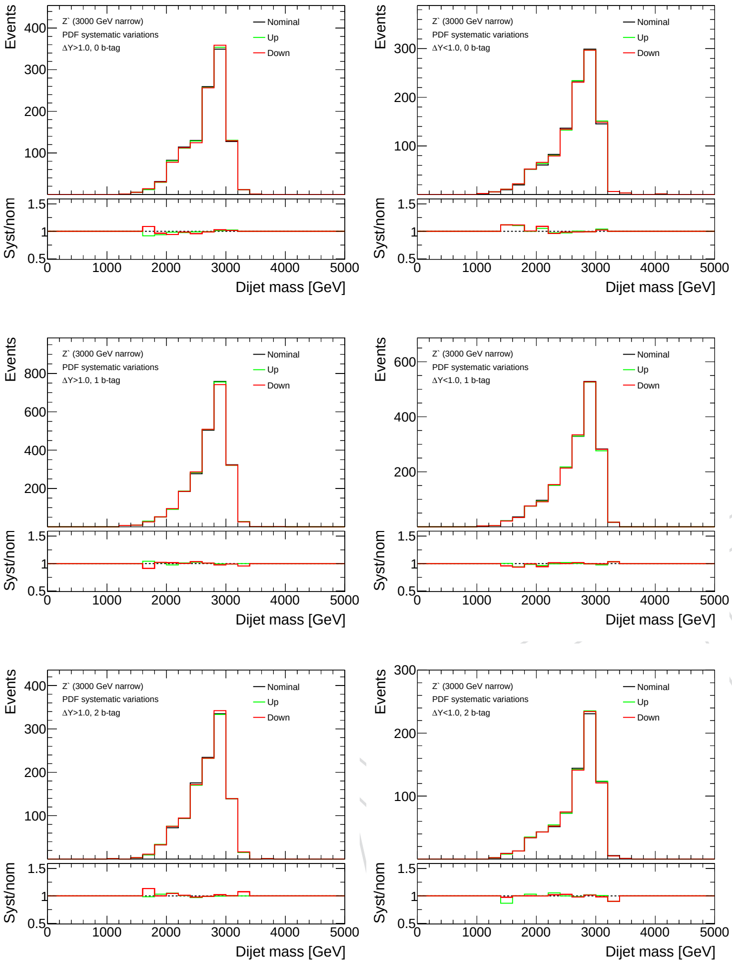

Figure 70: Effect of the PDF uncertainties on the $m_{t\bar{t}}$ shape for the narrow 3 TeV Z′ Monte Carlo sample for all 6 event categories.

Z’ (5 TeV) narrow

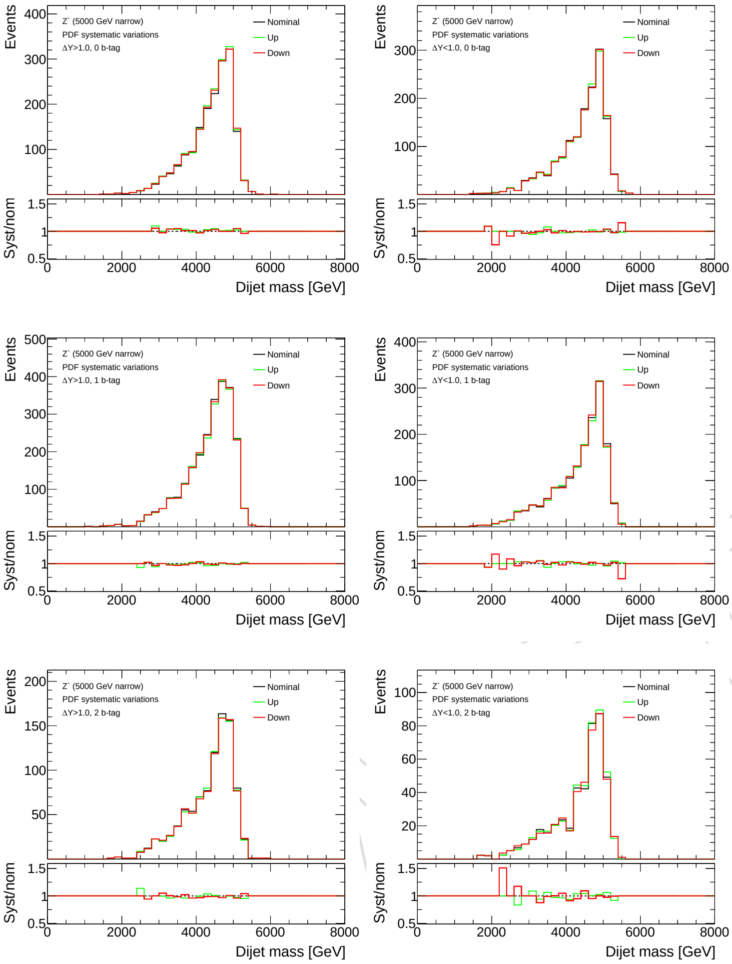

Figure 71: Effect of the PDF uncertainties on the $m_{t\bar{t}}$ shape for the narrow 5 TeV Z′ Monte Carlo sample for all 6 event categories.

Z’ (1.5 TeV) wide

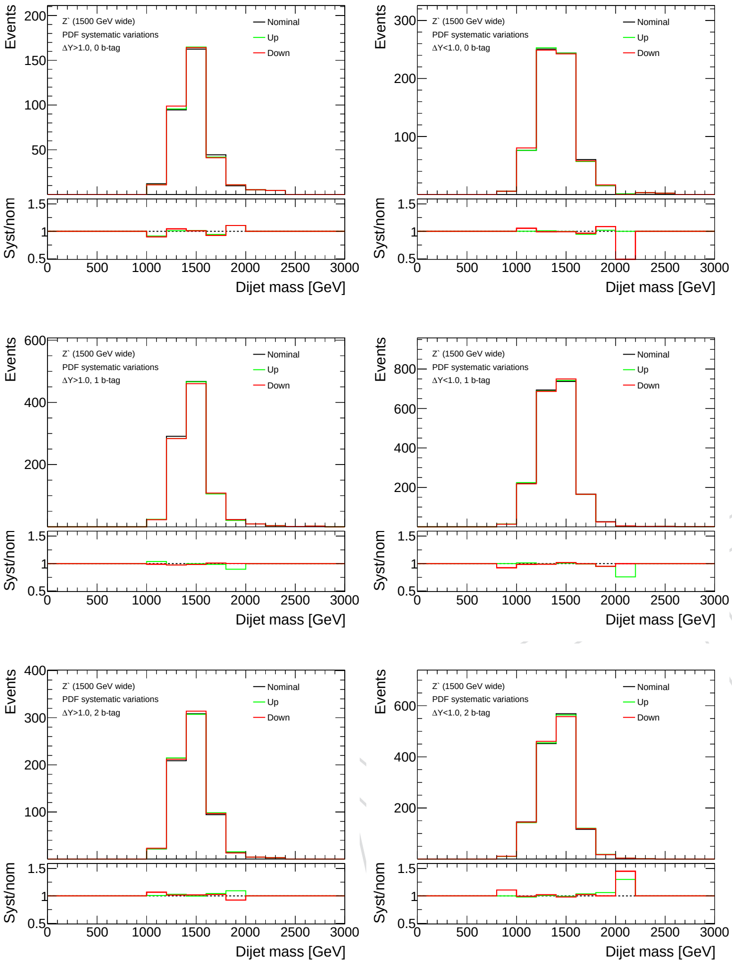

Figure 72: Effect of the PDF uncertainties on the $m_{t\bar{t}}$ shape for the wide 1.5 TeV Z' Monte Carlo sample for all 6 event categories.

Z’ (3 TeV) wide

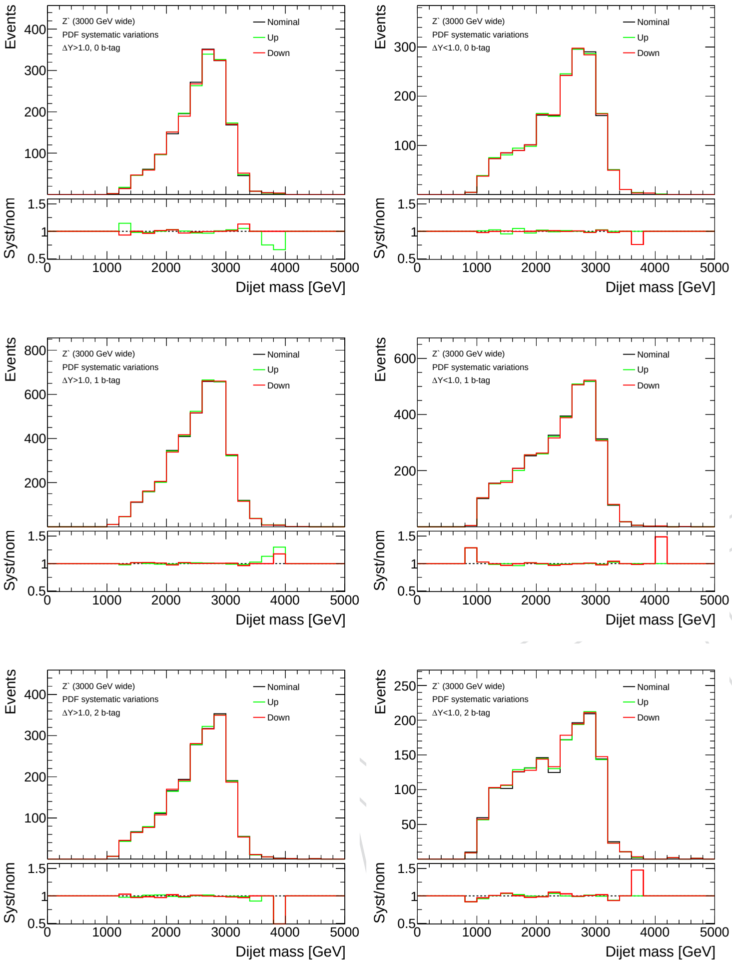

Figure 73: Effect of the PDF uncertainties on the $m_{t\bar{t}}$ shape for the wide 3 TeV Z' Monte Carlo sample for all 6 event categories.

798 Z’ (5 TeV) wide

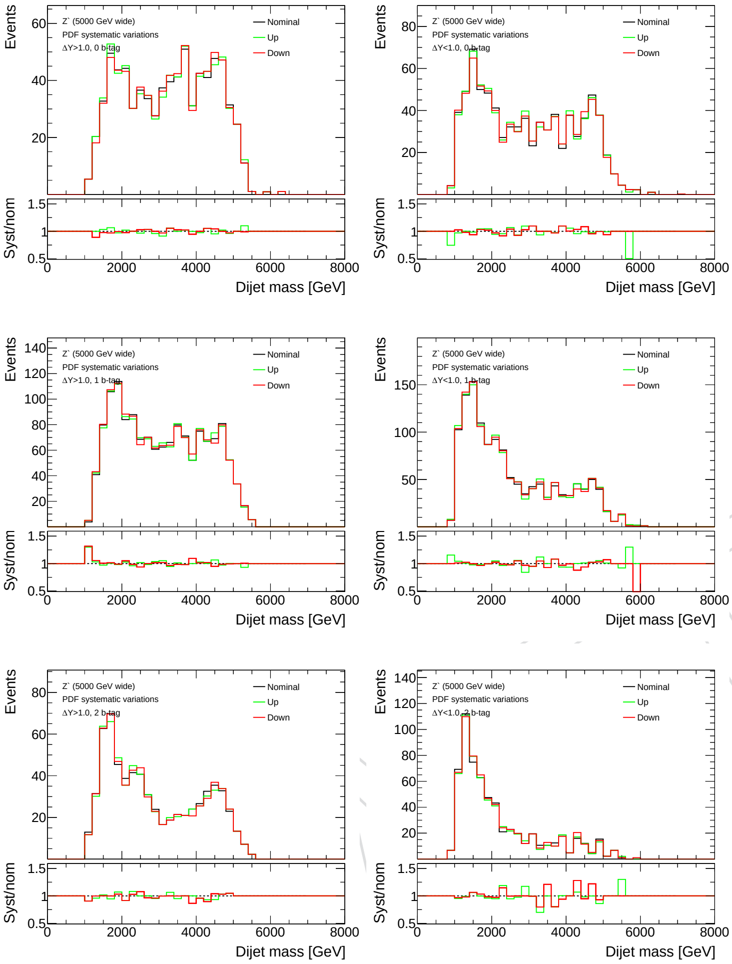

Figure 74: Effect of the PDF uncertainties on the $m_{t\bar{t}}$ shape for the wide 5 TeV Z' Monte Carlo sample for all 6 event categories.

799 RS Gluon (1.5 TeV)

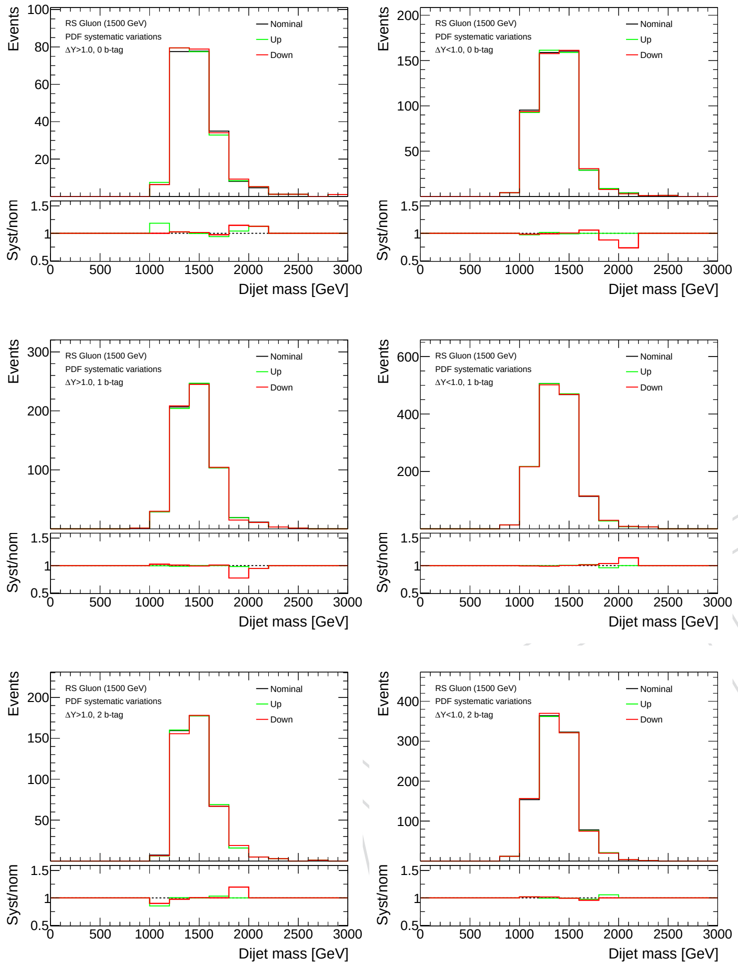

Figure 75: Effect of the PDF uncertainties on the $m_{t\bar{t}}$ shape for the 1.5 TeV RS GLuon sample for all 6 event categories.

800 RS Gluon (3 TeV)

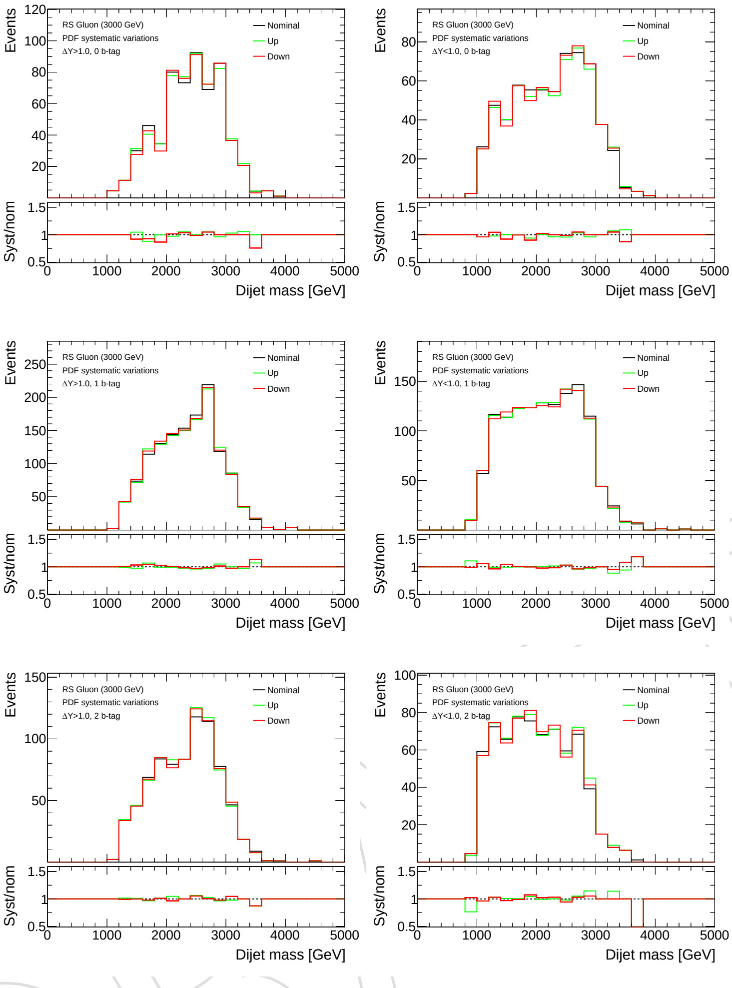

Figure 76: Effect of the PDF uncertainties on the $m_{t\bar{t}}$ shape for the 3 TeV RS Gluon sample for all 6 event categories.

C.5 PU Uncertainty

Standard Model ttbar

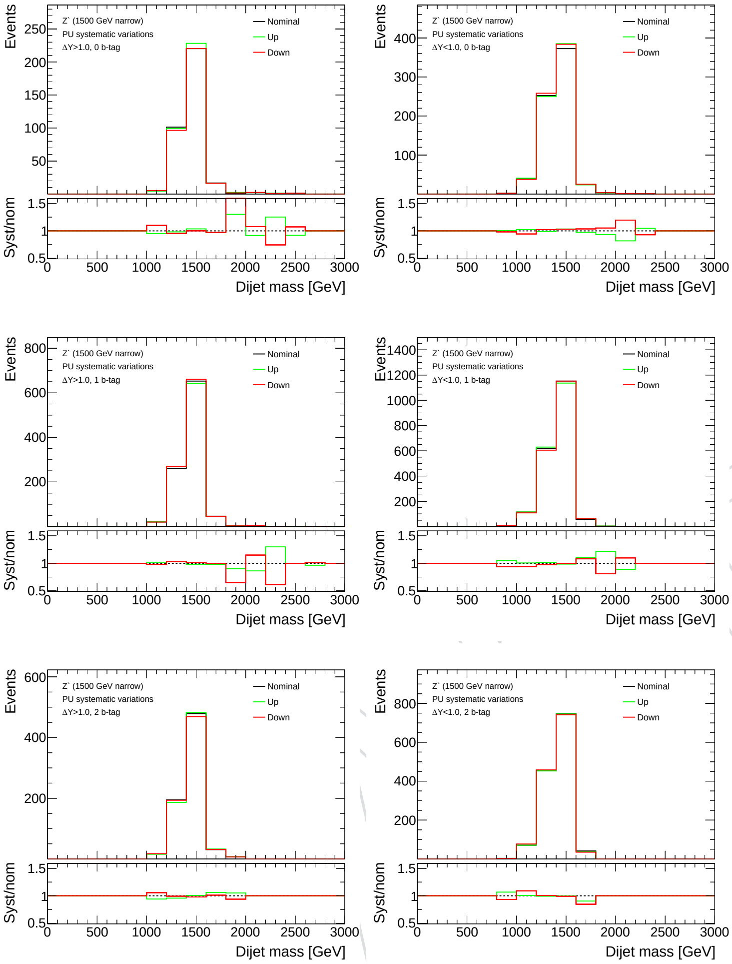

Figure 77: Effect of the pileup uncertainties on the $m_{t\bar{t}}$ shape for the $t\bar{t}$ Monte Carlo sample for all 6 event categories.

Z’ (1.5 TeV) narrow

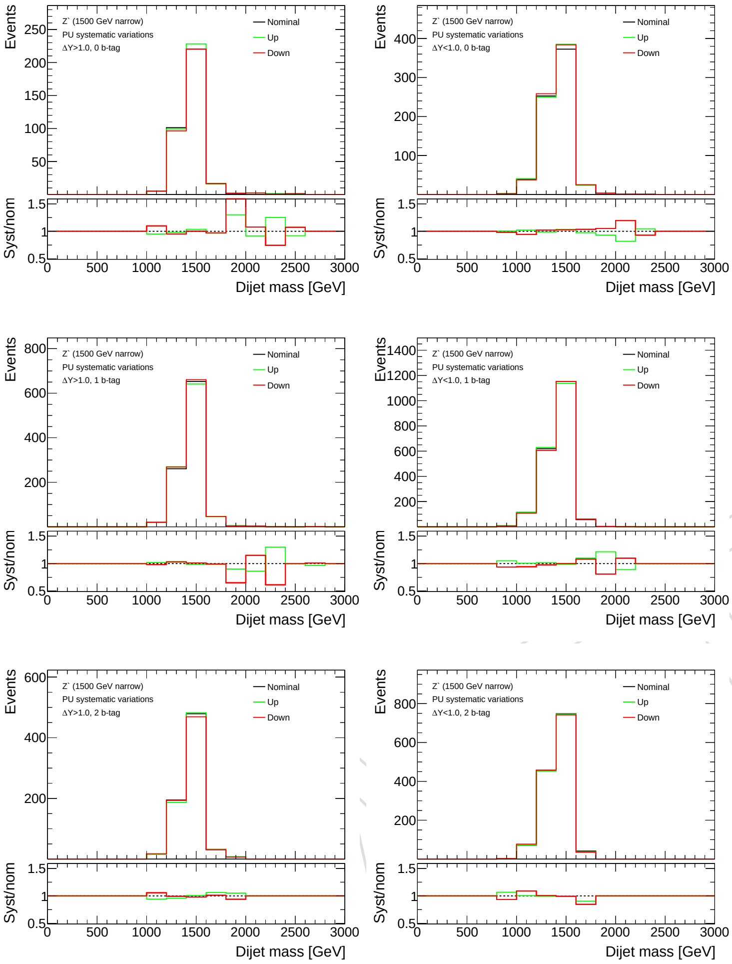

Figure 78: Effect of the pileup uncertainties on the $m_{t\bar{t}}$ shape for the narrow 1.5 TeV Z′ Monte Carlo sample for all 6 event categories.

Z’ (3 TeV) narrow

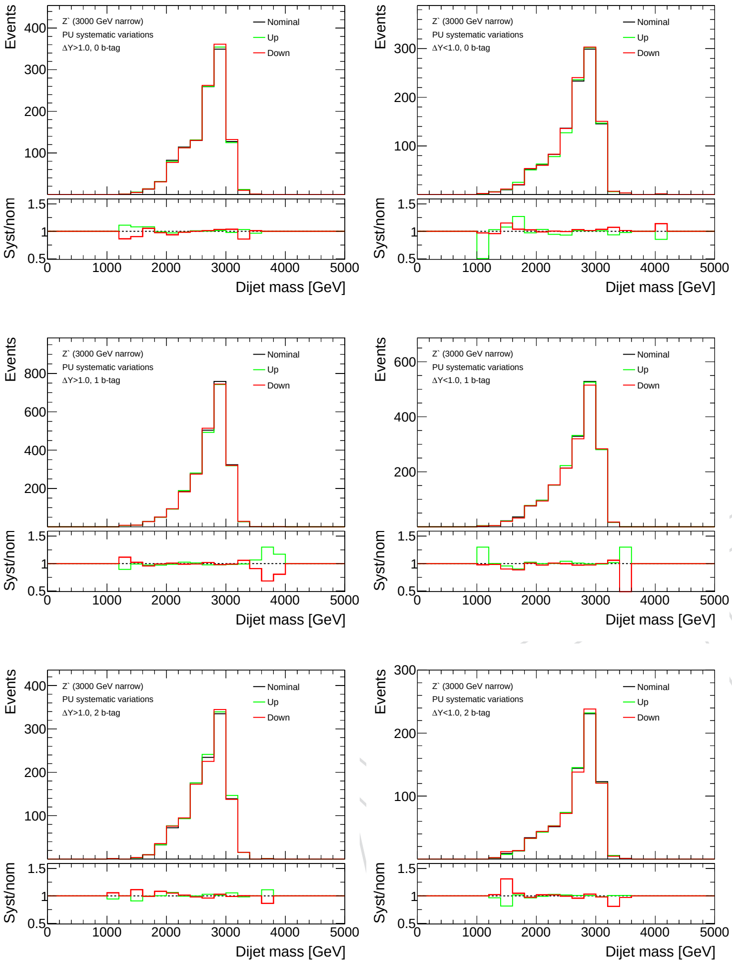

Figure 79: Effect of the pileup uncertainties on the $m_{t\bar{t}}$ shape for the narrow 3 TeV Z′ Monte Carlo sample for all 6 event categories.

805 Z’ (5 TeV) narrow

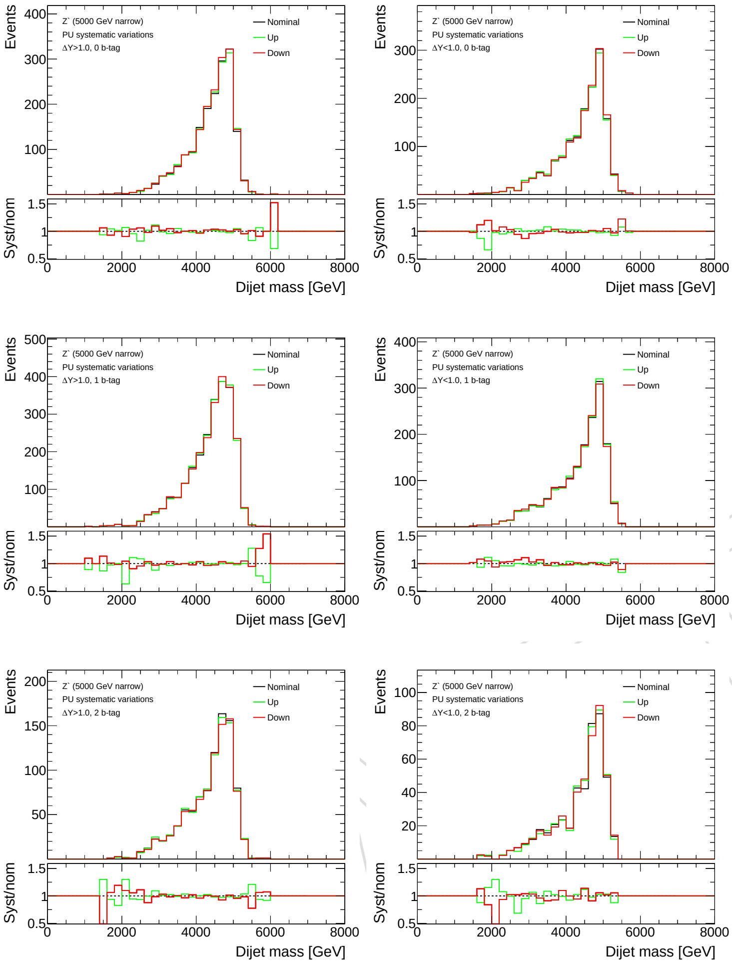

Figure 80: Effect of the pileup uncertainties on the $m_{t\bar{t}}$ shape for the narrow 5 TeV Z′ Monte Carlo sample for all 6 event categories.

806 Z’ (1.5 TeV) wide

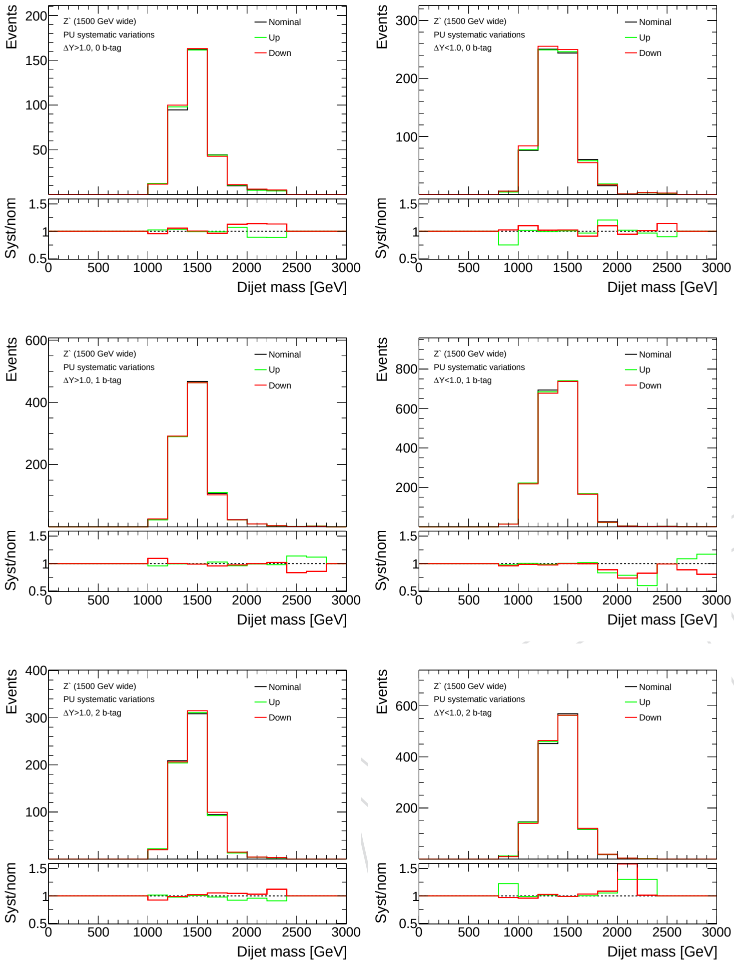

Figure 81: Effect of the pileup uncertainties on the $m_{t\bar{t}}$ shape for the wide 1.5 TeV Z′ Monte Carlo sample for all 6 event categories.

Z' (3 TeV) wide

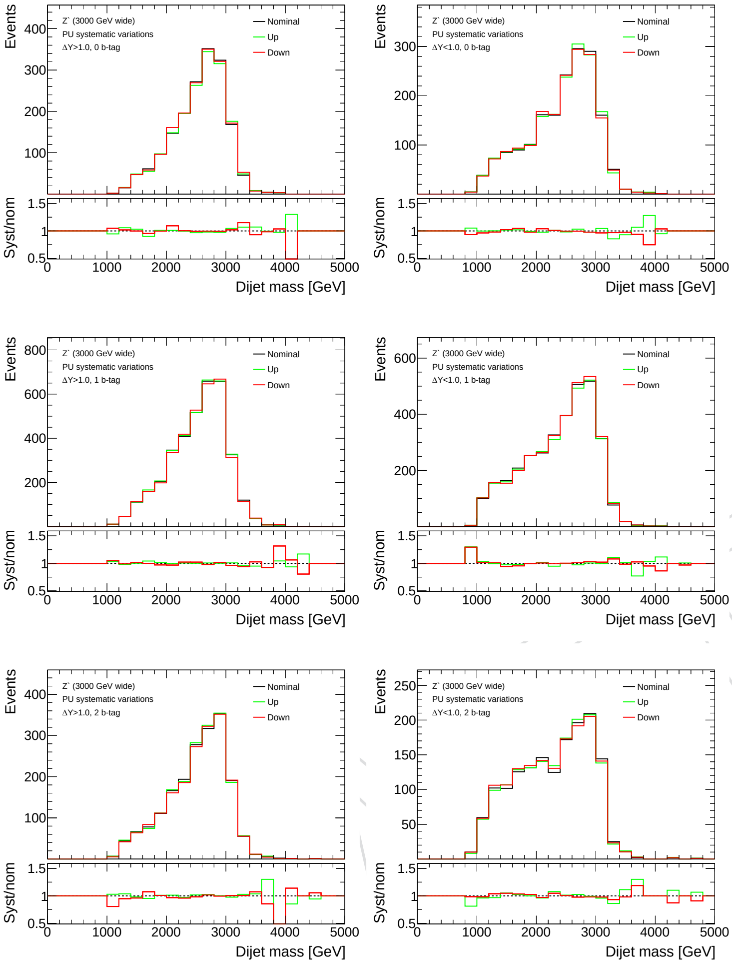

Figure 82: Effect of the pileup uncertainties on the $m_{t\bar{t}}$ shape for the wide 3 TeV Z′ Monte Carlo sample for all 6 event categories.

808 Z' (5 TeV) wide

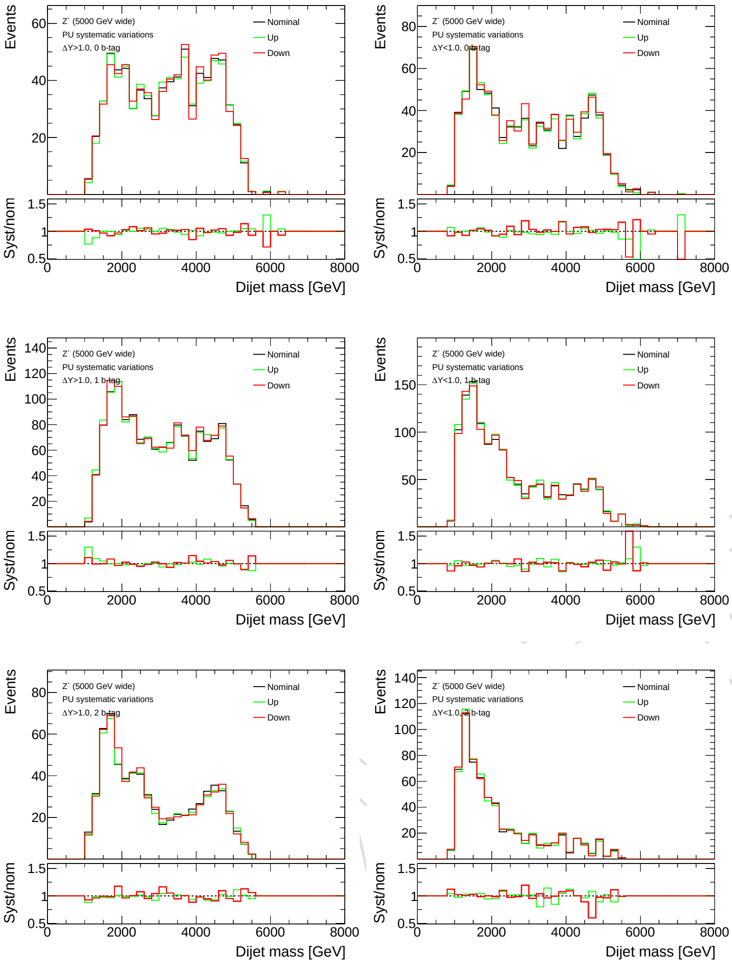

Figure 83: Effect of the pileup uncertainties on the $m_{t\bar{t}}$ shape for the wide 5 TeV Z′ Monte Carlo sample for all 6 event categories.

RS Gluon (1.5 TeV)

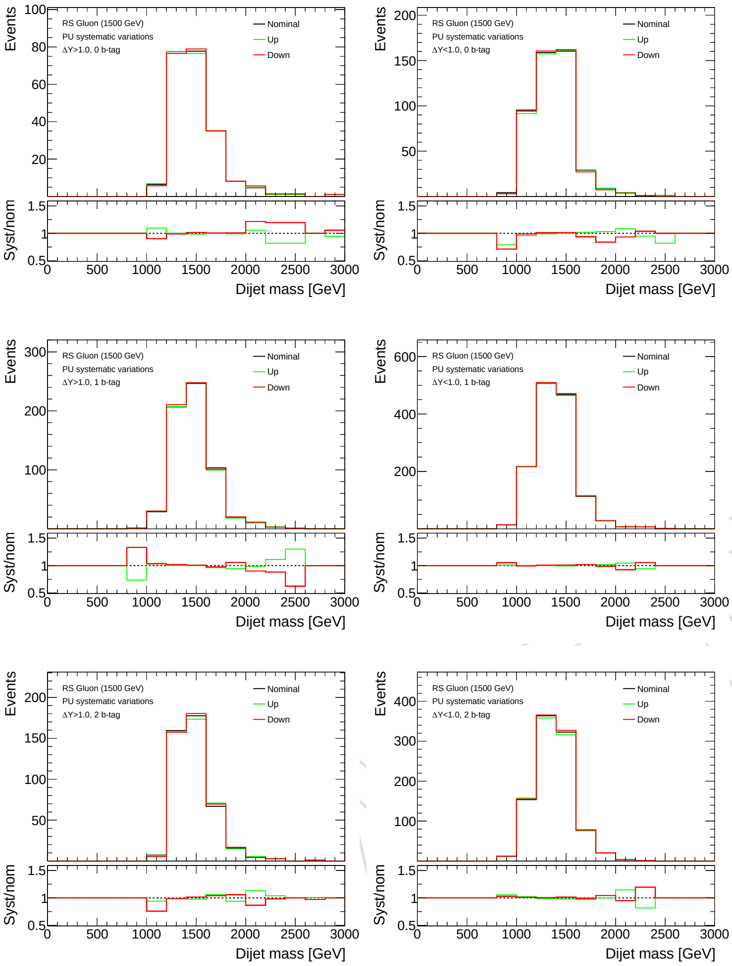

Figure 84: Effect of the pileup uncertainties on the $m_{t\bar{t}}$ shape for the 1.5 TeV RS GLuon sample for all 6 event categories.

RS Gluon (3 TeV)

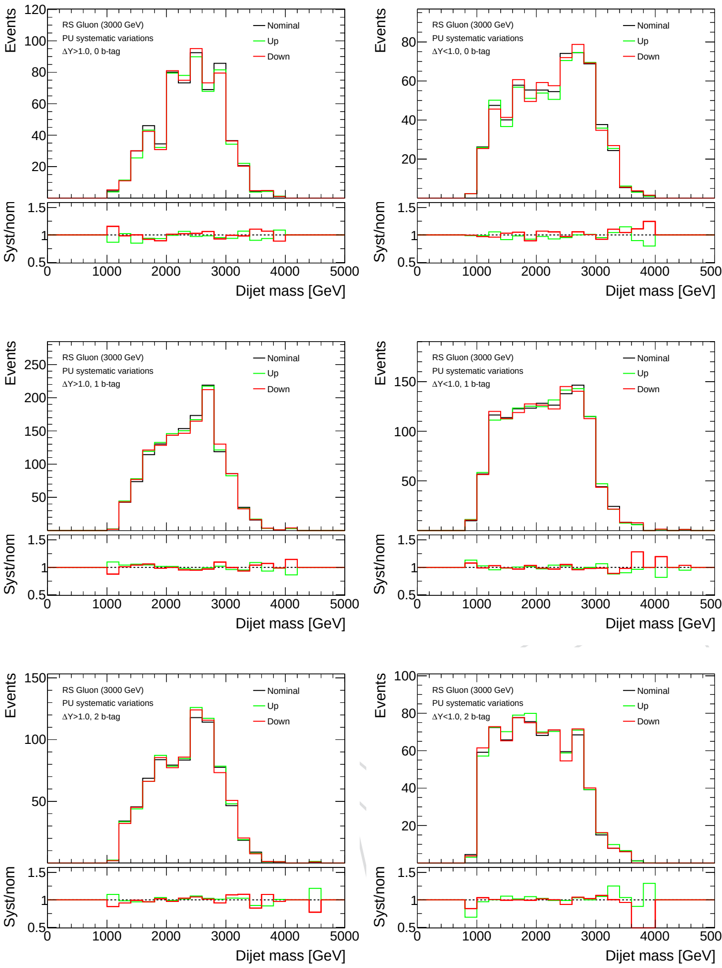

Figure 85: Effect of the pileup uncertainties on the $m_{t\bar{t}}$ shape for the 3 TeV RS Gluon sample for all 6 event categories.

C.6 Q2 Uncertainty

Standard Model ttbar

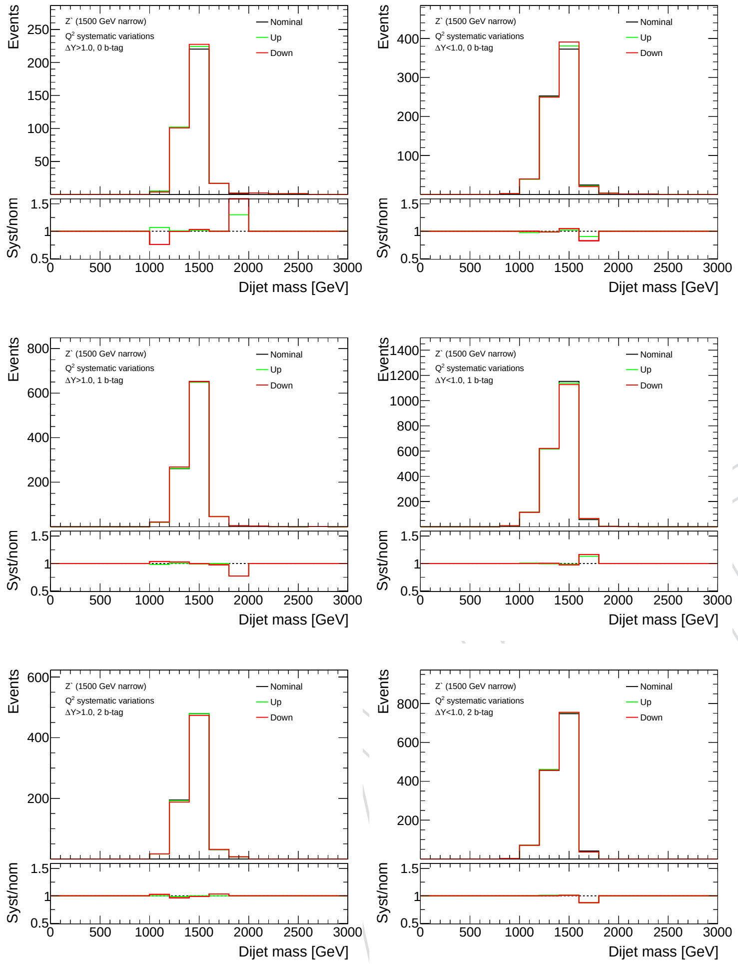

Figure 86: Effect of Q^2 uncertainties on the $m_{t\bar{t}}$ shape for the $t\bar{t}$ Monte Carlo sample for all 6 event categories.

813 Z’ (1.5 TeV) narrow

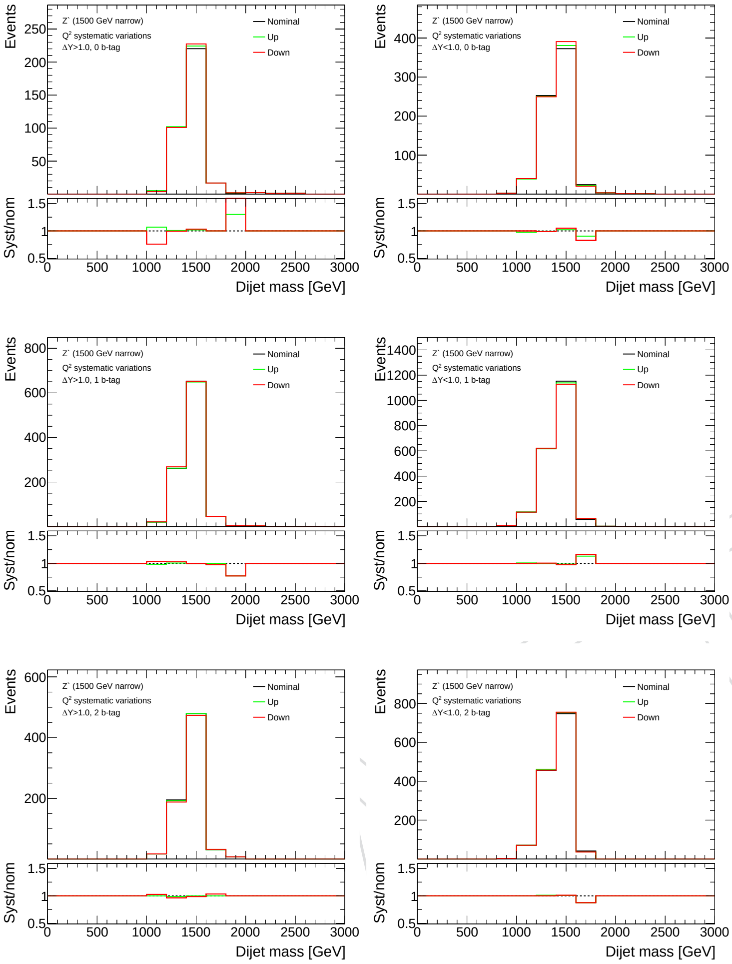

Figure 87: Effect of Q^2 uncertainties on the $m_{t\bar{t}}$ shape for the narrow 1.5 TeV Z′ Monte Carlo sample for all 6 event categories.

Z’ (3 TeV) narrow

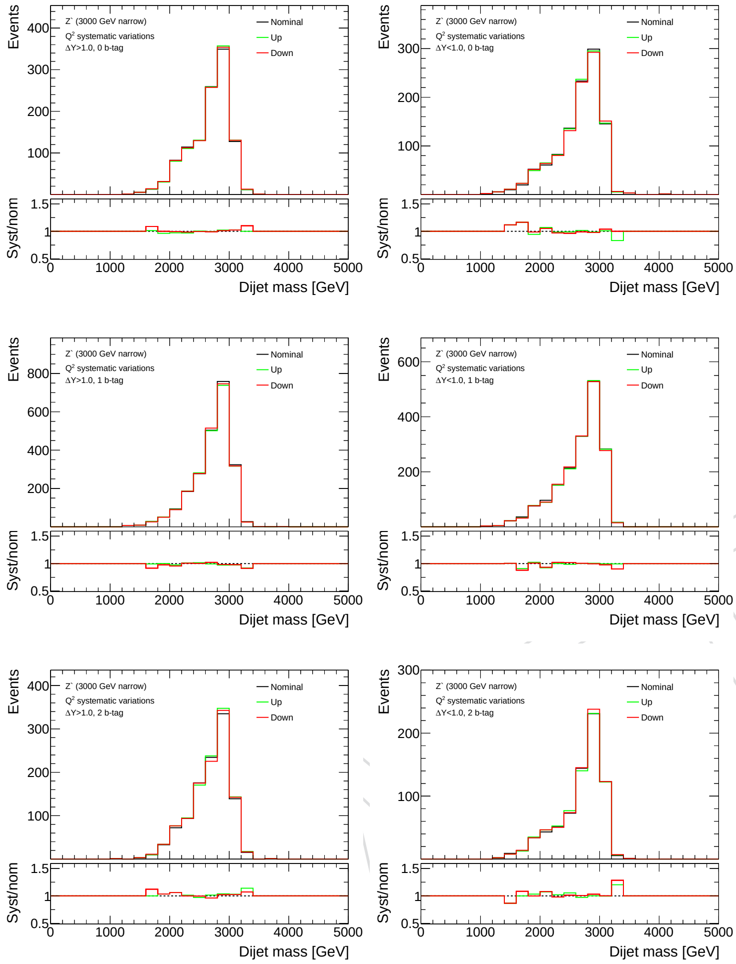

Figure 88: Effect of Q^2 uncertainties on the $m_{t\bar{t}}$ shape for the narrow 3 TeV Z′ Monte Carlo sample for all 6 event categories.

Z’ (5 TeV) narrow

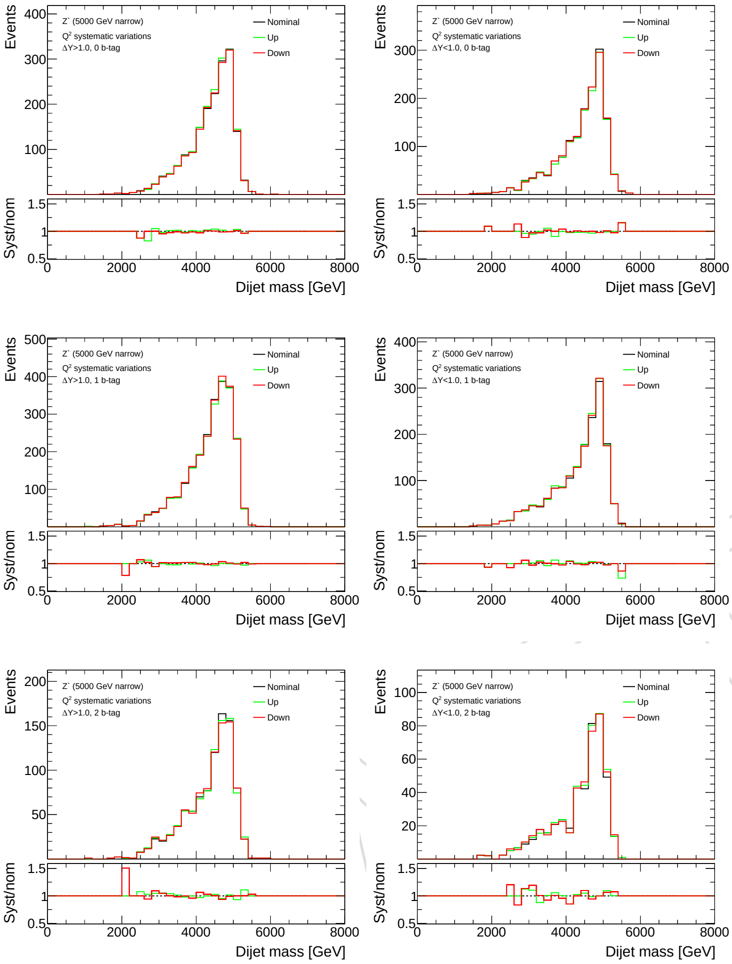

Figure 89: Effect of Q^2 uncertainties on the $m_{t\bar{t}}$ shape for the narrow 5 TeV Z′ Monte Carlo sample for all 6 event categories.

816 **Z' (1.5 TeV) wide**

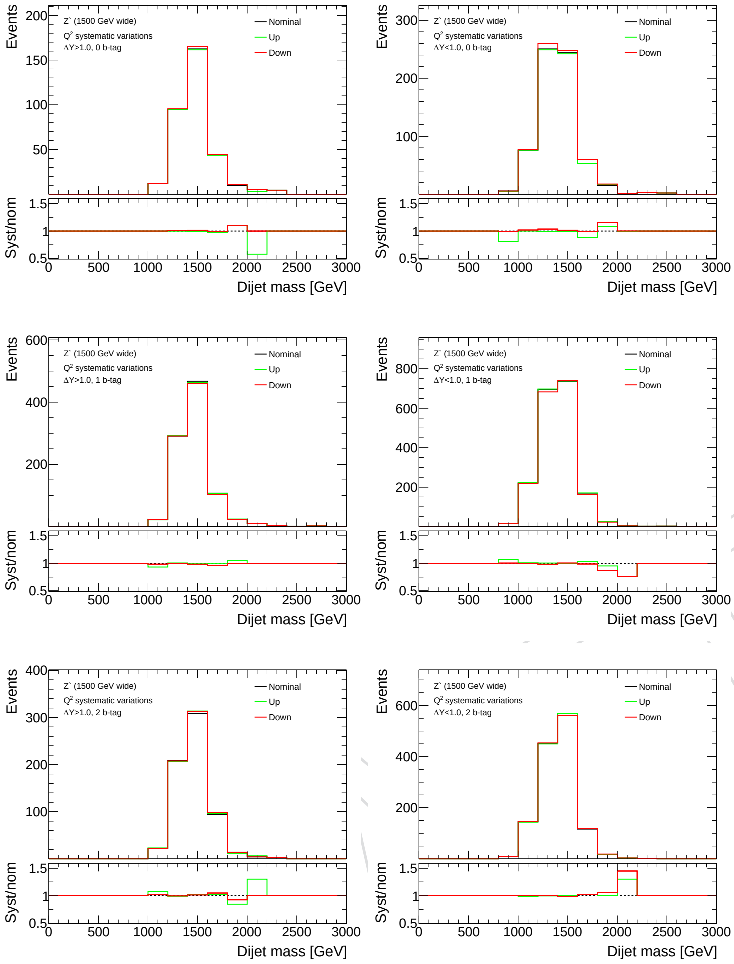

Figure 90: Effect of Q^2 uncertainties on the $m_{t\bar{t}}$ shape for the wide 1.5 TeV Z′ Monte Carlo sample for all 6 event categories.

Z' (3 TeV) wide

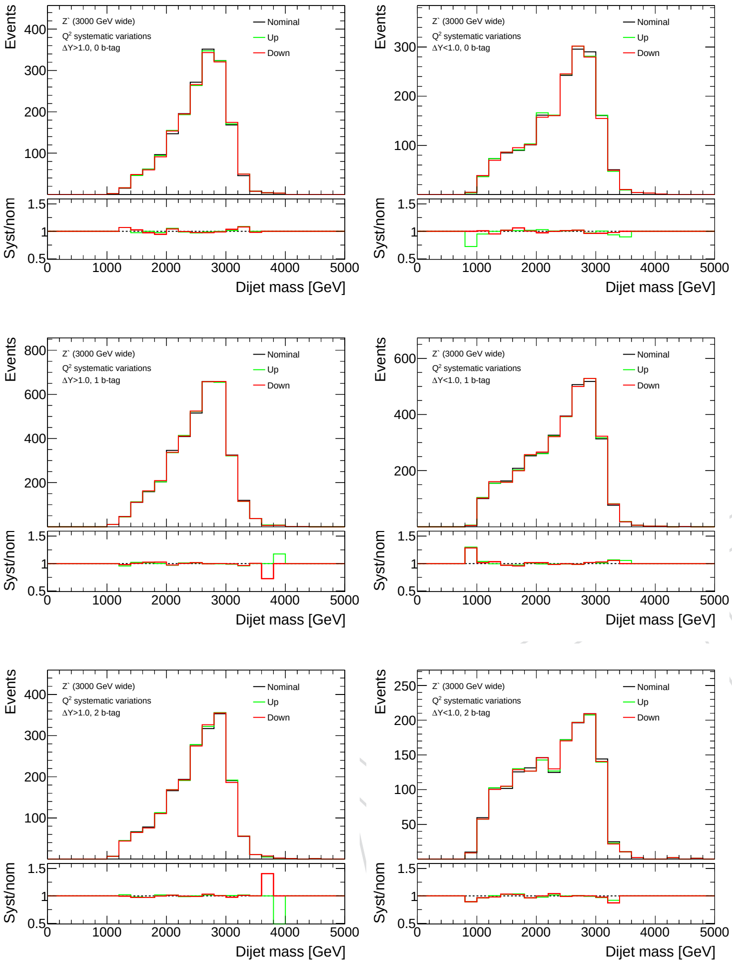

Figure 91: Effect of Q^2 uncertainties on the $m_{t\bar{t}}$ shape for the wide 3 TeV Z' Monte Carlo sample for all 6 event categories.

Z' (5 TeV) wide

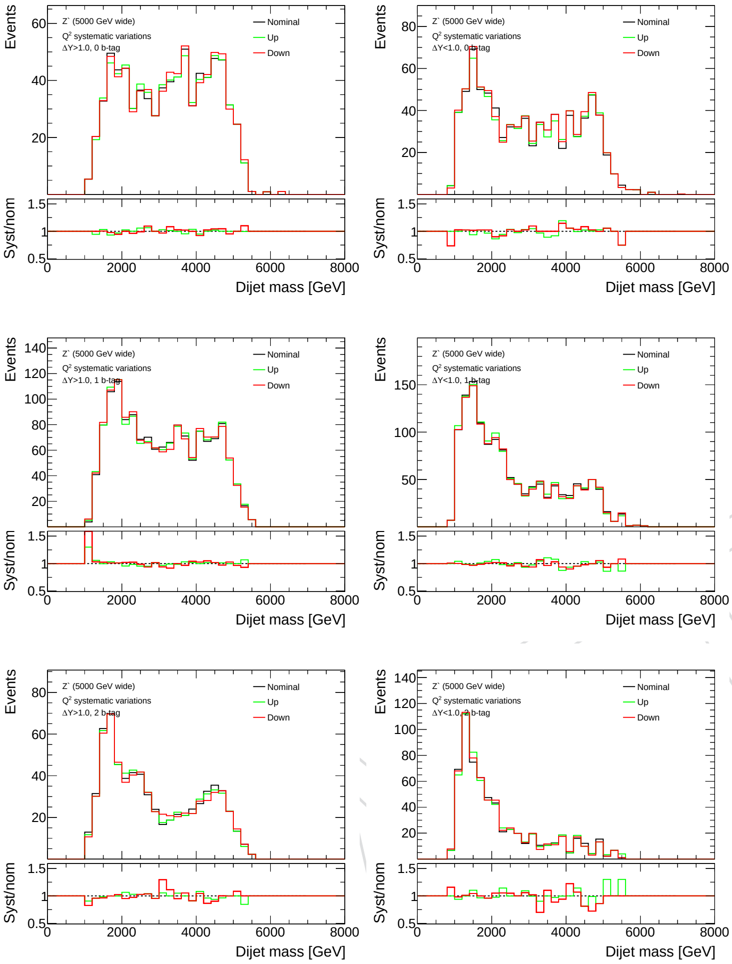

Figure 92: Effect of Q^2 uncertainties on the $m_{t\bar{t}}$ shape for the wide 5 TeV Z' Monte Carlo sample for all 6 event categories.

RS Gluon (1.5 TeV)

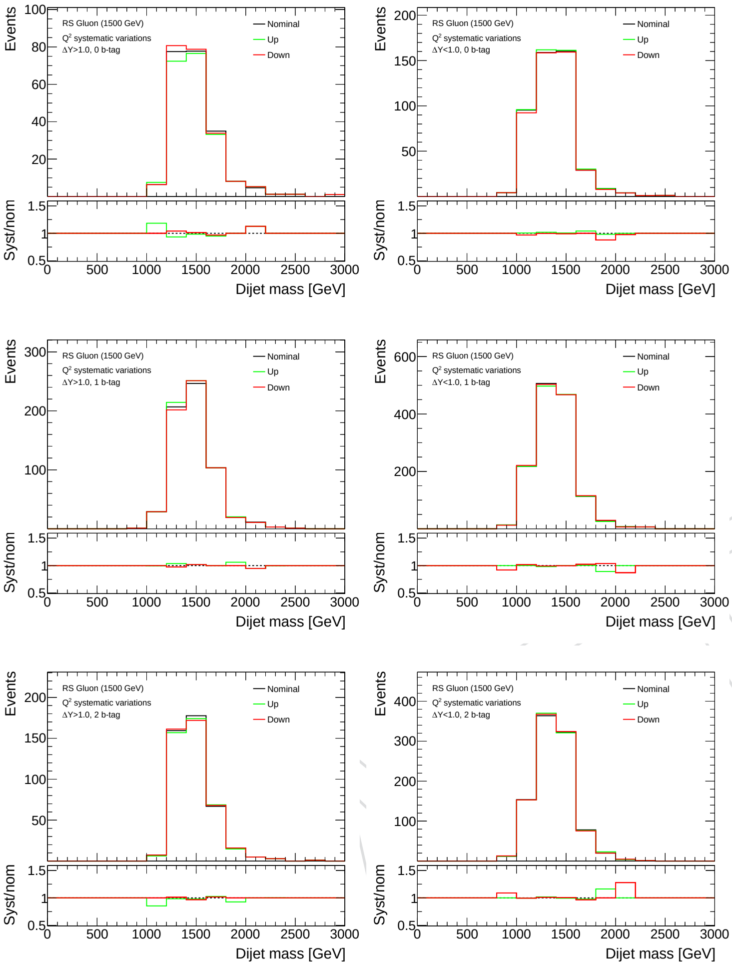

Figure 93: Effect of Q^2 uncertainties on the $m_{t\bar{t}}$ shape for the 1.5 TeV RS GLuon sample for all 6 event categories.

RS Gluon (3 TeV)

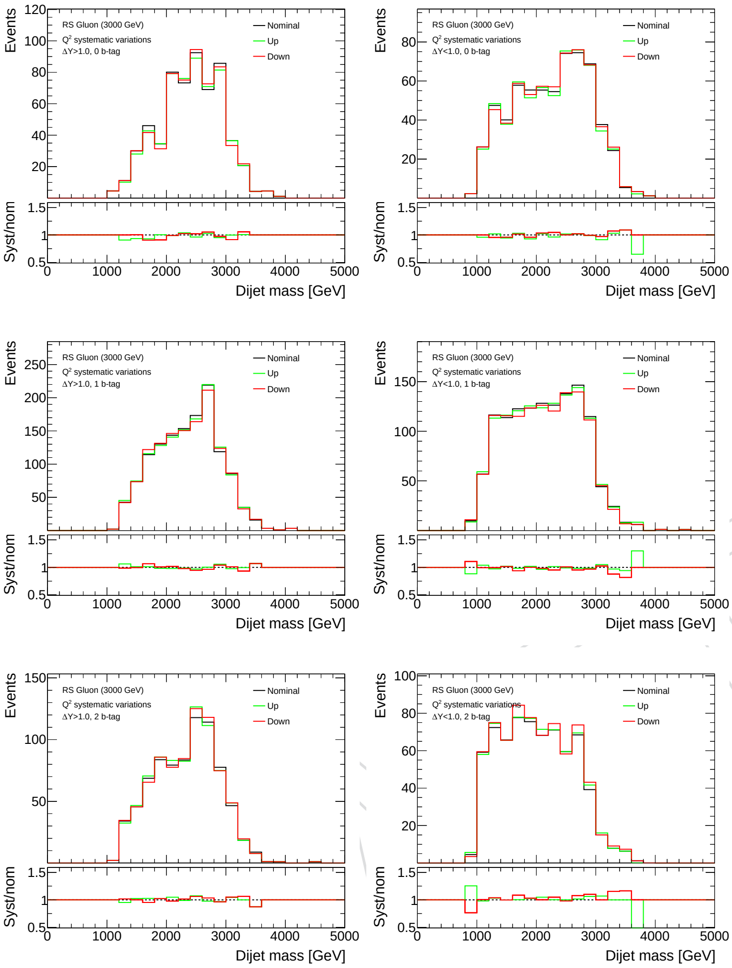

Figure 94: Effect of Q^2 uncertainties on the $m_{t\bar{t}}$ shape for the 3 TeV RS Gluon sample for all 6 event categories.

C.7 QCD Modified Mass Procedure

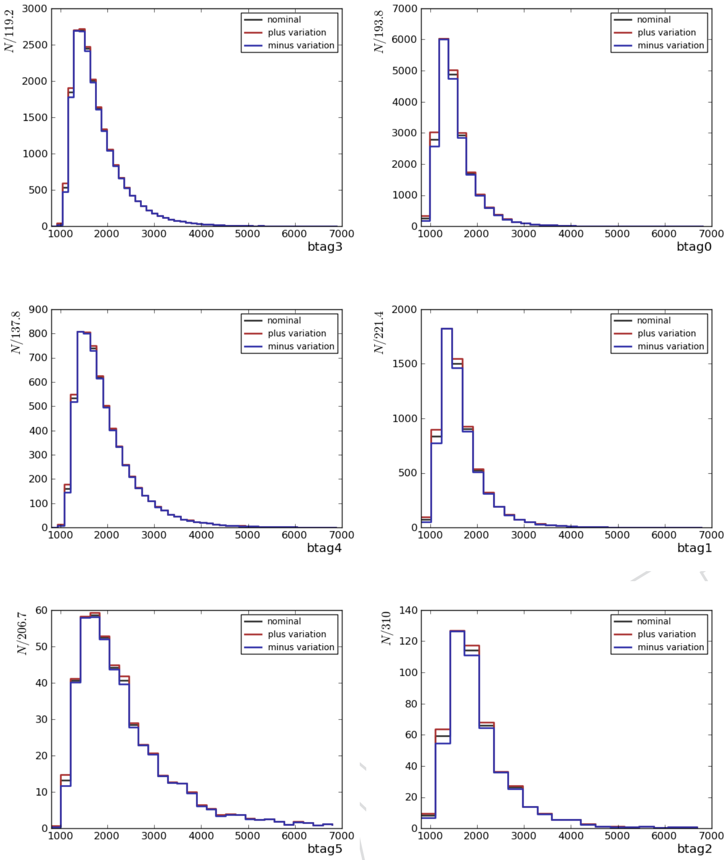

Figure 95: Effect of the NTMJ shape uncertainty due to the modified mass procedure on the $m_{t\bar{t}}$ shape for the NTMJ background estimation for all 6 event categories. The left (right) column shows the variation of the uncertainty by $\pm 1\sigma$ for the low (high) $|Deltay|$ region. The number of subjet b-tags increases from the first row to the last.

C.8 QCD Closure Test

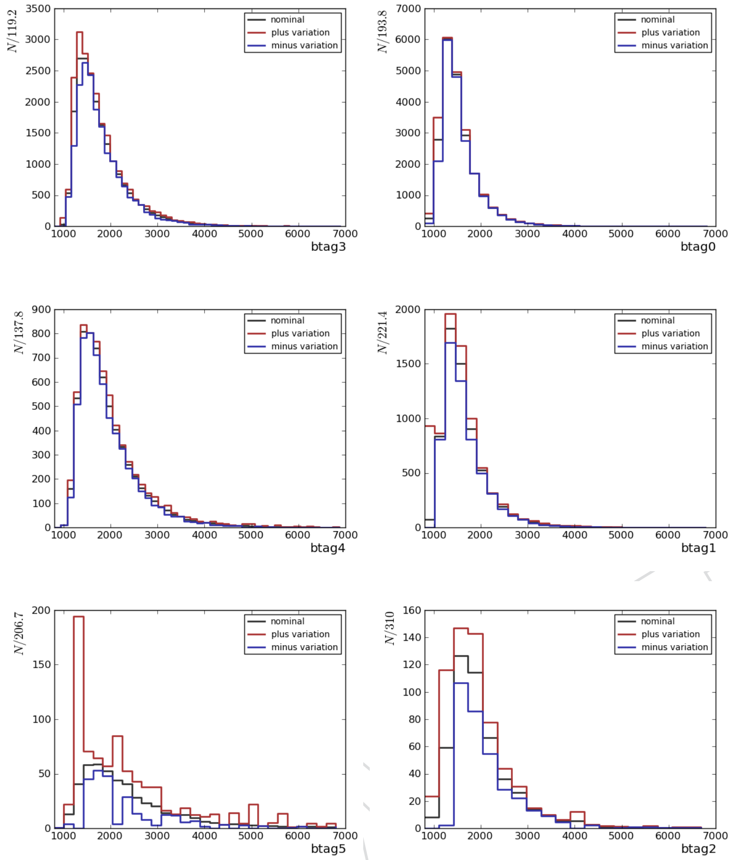

Figure 96: Effect of the NTMJ shape uncertainty due to the closure test results on the $m_{t\bar{t}}$ shape for the NTMJ background estimation for all 6 event categories. The left (right) column shows the variation of the uncertainty by $\pm 1\sigma$ for the low (high) $|\Delta y|$ region. The number of subjet b-tags increases from the first row to the last.

D $m_{t\bar{t}}$ Distributions Used in Limit Setting

The final $m_{t\bar{t}}$ distributions, with the binning used in limit setting, are shown in Figure 97.

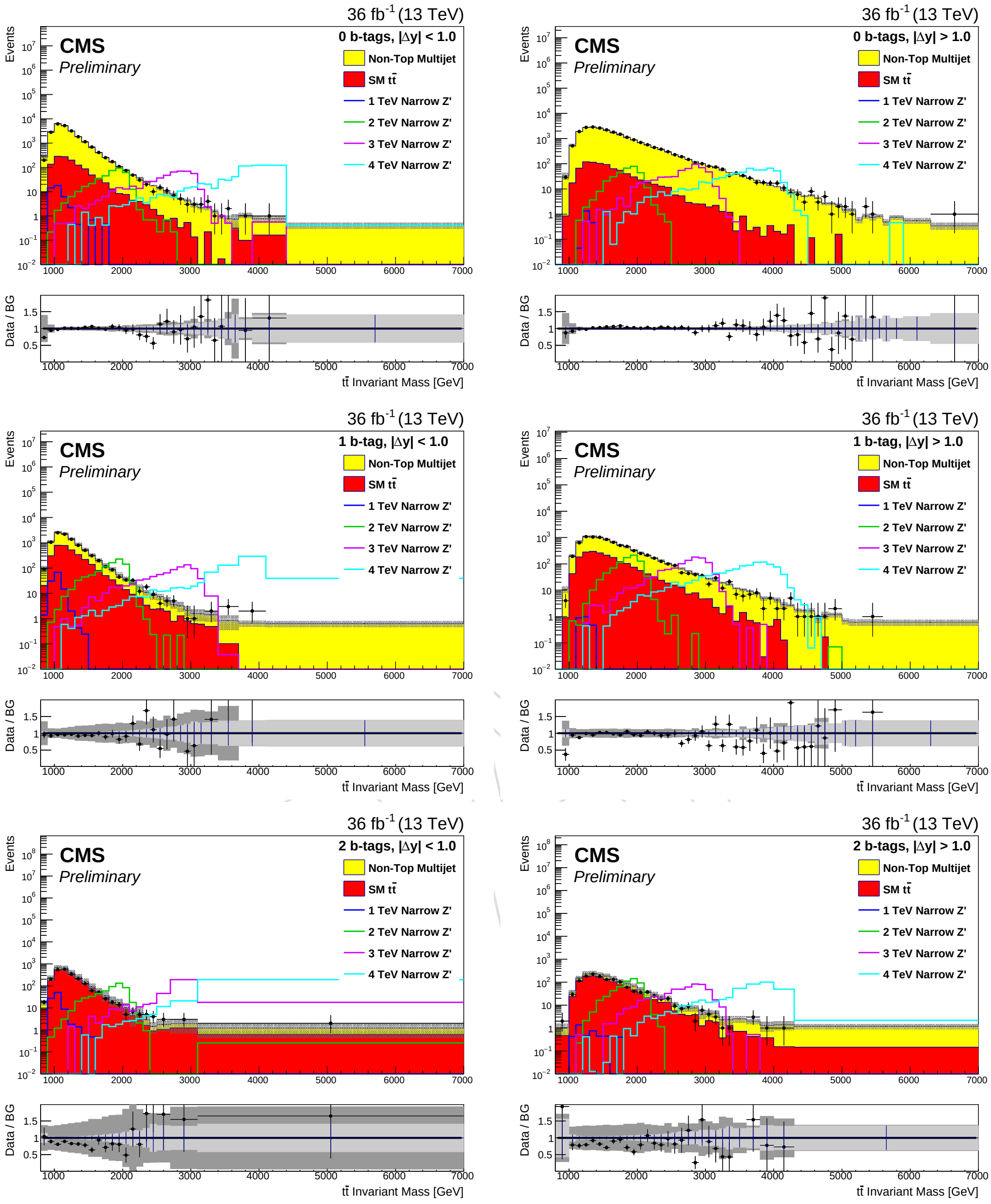

Figure 97: Final log-scale distributions of $m_{t\bar{t}}$, used in limit setting. All six signal regions are shown, with the $\Delta y < 1.0$ categories shown in the left column and the $\Delta y > 1.0$ categories in the right. The number of b-tags in the plots increase from zero in the first row to two b-tags in the third row. The shaded region corresponds to the combined systematic (dark gray) and statistical (light gray) uncertainties on the background model. Signal models have been normalized to a cross section of 1 pb. The bins in the plot were combined from right to left to create bins with a maximum background MC statistical error of 30%.